PEOPLE'S DEMOCRATIC REPUBLIC OF ALGERIA

MINISTRY OF HIGHER EDUCATION AND SCIENTIFIC RESEARCH

IBN KHALDOUN UNIVERSITY OF TIARET

FACULTY OF APPLIED SCIENCES

DEPARTMENT OF ELECTRICAL ENGINEERING

THESIS

Presented by:

Mr. CHELIH Amine

For the degree of:

DOCTORATE (L.M.D)

Specialty: **Electrical Networks**

TOPIC

Complementary Study of Physical and Geometrical Parameters for a Better Understanding of Ionic Wind Generation

The jury consists of:

Y. MESSLEM	Pr	President	Ibn Khaldoun University, Tiaret
M. GUEMOU	Pr	Examiner	Ibn Khaldoun University, Tiaret
Z. KECHIDI	MCA	Examiner	National Higher School of Autonomous Systems Technology of Sidi Abdellah - Alger
M.F. BEKKARA	MCA	Examiner	Mustapha Stambouli University - Mascara
M. BOUADI	MCA	Co-Supervisor	Ibn Khaldoun University, Tiaret
K. YANALLAH	Pr	Supervisor	Ibn Khaldoun University, Tiaret

Academic Year: 2024-2025

Acknowledgments

First and foremost, I would like to thank Almighty God for granting me the strength and patience to accomplish this task.

I wish to express my deepest gratitude to my supervisor, Professor **Khelifa YANALLAH**, a faculty member at the University of Tiaret, for agreeing to oversee my doctoral thesis. I am especially grateful for his warm welcome, invaluable assistance, insightful feedback, fruitful advice, and unwavering support throughout this research.

I extend my sincere thanks to Professor **Youcef MESLEM**, Director of the Laboratory of Electrical Engineering and Plasma (LGEP) at Ibn Khaldoun University, Tiaret, for his warm hospitality and immense kindness during the preparation of this dissertation. Furthermore, I am deeply grateful for Professor **MESLEM'S** acceptance to preside over the jury for this thesis.

I would also like to express my profound gratitude to my co-supervisor, **Dr. Mohammed BOUADI**, a faculty member at the University of Tiaret, for his relevant insights, valuable guidance, and active involvement in this project.

My sincere thanks also go to the members of the jury for their interest in this work and for accepting to evaluate it, namely:

Pr. M'hamed GUEMOU, Ibn Khaldoun University - Tiaret;

Dr. Ziane KECHIDI, Senior Lecturer (Class A) at National Higher School of Autonomous Systems Technology of Sidi Abdellah - Alger;

Dr. Mohammed Fethi BEKKARA, Senior Lecturer (Class A) at Mustapha Stambouli University - Mascara.

I am deeply thankful to **Dr. Mohamed Ridha BOUAZZA**, a faculty member at the University of Blida, and **Dr. Ahmed SAFA**, a faculty member at the University of Tiaret, for their support, discussions, and enlightened opinions. I warmly acknowledge their scientific expertise.

I would like to extend my special and sincere gratitude to Professor **Youcef BENMIMOUN**, a professor at the University of Mascara, and **Mr. Mohamed Fethi BEKKARA**, for their invaluable assistance and constant support, particularly in helping me obtain my external internship acceptance letter. Their support marked a crucial milestone in my academic journey, and I am deeply grateful for their trust and consistent encouragement.

I also wish to thank **Pr. F. Pontiga**, a professor at the University of Seville (Spain), and **Pr. P. Vazquez,** a professor at the University of Seville (Spain), for their assistance and guidance in enabling me to work and progress remotely. Their collaboration and support have been invaluable to the advancement of this research.

My sincere appreciation goes to Professors **Lucian DASCALESCU** and **Thami ZEGHLOUL** for welcoming me into their laboratories at the IUT University in Angoulême. Their availability, encouragement, and the resources they provided allowed me to conduct my work in an enriching and stimulating environment.

I would also like to thank all the professors I had the honor to meet during my academic journey, including ***Dr. Mohamed OMARI*** *and* ***Mr. Abdelmadjid GOUICHICHE****.*

I extend my gratitude to all my colleagues and fellow researchers, especially ***Ali BOUARGOUB, Salah Eddine Chouaib REFAS, Abdelkader Azzeddine BENGHARBI, Younes ABDELBARI, Mohamed Sofiane BENDILMI, Khaled DAIOUI, and Djalili****.*

Finally, I express my appreciation to the directors, administrative staff, and the entire faculty of the University of Tiaret for their support and encouragement throughout this journey.

Dedicate

To my beloved family,

Your unwavering support, unconditional love, and constant encouragement have been the cornerstone of my journey.

To my parents, for your sacrifices and belief in my dreams.

To my siblings, for your companionship and inspiration.

This work is a testament to your profound impact on my life and a small way to honor the strength and guidance you have always provided.

With all my love and gratitude.

Table of Contents

List of figures

List of tables

Nomenclature

$\mathbf{J}_i$	Flux of particles of type i ($i = e, p$ and n).
N_i	Number density of particles of type i ($i = e, p$ and n), N number density of neutral particles.
j	The current density, j_0 defined at the corona electrode and j_T defined at the ground.
ΔS	The surface perpendicular to the electric field line, ΔS_0 defined at the corona electrode and ΔS_T defined at the ground.
$\mathbf{E}$	The electric field, E_0 defined at the corona electrode (Peek formula).
$\mathbf{F}$	The EHD force acting on air.
ϕ	The electric potential, ϕ_0 defined at the corona electrode and ϕ_{calc} Estimated at the corona electrode.
ϕ_{onset}	The onset voltage.
ϕ_c	The critical applied voltage
I	The electric current.
v	The gas velocity, v_{max} the maximum gas velocity.
ρ_c	Space charge density.
q_p	The positive space charge density.
η_{eff}	Energy efficiency.
r_0	Corona wire radius.
R_c	Cylinder radius.
f	The separation distance between the two wires.
d	Inter-electrode separation.
w	wire length.
dl_a	displacement along the electric field line.
L_a	The total length of the electric field line.

Nomenclature

l_a	The arc length along the electric field line
L	The distance between the two grounded plates (Opening width).
l	The width of the grounded plates.
ℓ	The length of the upper and lower plates
h	The distance separation between the upper and lower plates
θ	Angle of the average direction of the EHD force
θ_p	The angle of deviation of the grounded rectangular plate electrode
α	The ionization coefficient.
η	The attachment coefficient.
ζ	The convergence criterion
ε_0	The air permittivity.
e_0	The elementary charge.
μ_i	The electrical mobility of particle of type i ($i = e, p$ and n).
ρ	The fluid density (The air density).
p	The gas pressure, p_0 atmospheric pressure.
T	The gas temperature, T_e the electron temperature, T_i the ion temperature and T_0 the room temperature.
λ	The dynamic viscosity.
μ_t	The turbulent viscosity
k	The turbulent kinetic energy
$\mathbf{I}$	The identity tensor
ε	The dissipation rate.
$\boldsymbol{\tau}_R$	The Reynolds stress tensor.
P_{mec}	The mechanical energy.

Nomenclature

P_{ele}	Electrical energy.
A_g	Gas flow cross-section.
v_g	Air flow velocity passing through the cross-sectional area Ag.
m_e	Mass of the electron
f_{pe}	Plasma frequency
λ_D	Debye length
k_B	Boltzmann constant
F_{DBD}	The average force of DBD
f	Represents body forces (such as gravitational or electromagnetic forces),

Introduction

Introduction

The study of corona discharge and its electrohydrodynamic (EHD) effects has garnered significant attention due to its wide-ranging applications in fields such as medicine, biology, electronics, and the environment [1-4]. It has also been exploited in industrial applications, including ozone generation [5], electrostatic precipitators [6], surface treatment [7], heat transfer enhancement [8], and electrostatic separation [9]. Corona discharge, a self-sustained electrical breakdown in gases, is a complex process involving interactions among charged particles, electric fields, and fluid motion, making it a significant topic in fundamental physics and engineering. The precise interaction between plasma physics, fluid mechanics, and electrical engineering offers opportunities to develop efficient and innovative solutions to various industrial challenges.

In general, corona discharge occurs when electrodes are subjected to a high voltage, particularly those with sharp curvatures, such as pointed tips, thin strips, or fine wires. During this process, charge carriers (electrons and ions) move across the interelectrode gap, repeatedly colliding with the neutral gas molecules. These collisions transfer part of the kinetic energy of the charge carriers to the neutral molecules, resulting in a bulk gas motion. This bulk flow, known as "electric wind" or "ionic wind," is a typical example of electrohydrodynamic (EHD) flow [10, 11]. The existence of ionic wind flow has been known for a long time [12]; however, it remains a subject of study and investigation due to its inherent complexity and significant industrial relevance.

This work addresses the modeling, validation, and applications of corona discharge in EHD systems, presenting a comprehensive approach that integrates numerical simulation, experimental validation, and innovative design optimization. By combining advanced modeling techniques with practical applications, this study contributes to ongoing research efforts to harness EHD phenomena for developing diverse technological solutions.

The first chapter provides a general introduction to plasma and electric discharges, with a specific focus on corona discharges, which are the primary objective of this research. After presenting the physical phenomena governing corona discharge, the chapter reviews the state of the art on ionic wind and discusses the various techniques for generating and applying ionic wind.

The second chapter focuses on developing a novel methodology to determine the spatial distribution of space charges and the density of the EHD force. This approach avoids traditional challenges related to numerical convergence in coupled equations and demonstrates significant flexibility by accommodating various electrode configurations for both positive and negative DC corona discharges.

In the third chapter, the numerical model is validated through precise comparisons with experimental data. This validation confirms the model's accuracy in predicting electrical characteristics, such as voltage-current relationships, and its effectiveness in simulating ionic wind and gas flow dynamics. Additionally, the research proposes an optimized electrode configuration for EHD air pumps, improving airflow distribution, energy efficiency, and simplicity of construction. This innovation addresses critical challenges in cooling systems, particularly for miniature electronic components.

The fourth chapter examines the shielding effect between neighboring corona discharge electrodes in wire-to-plate electrostatic precipitators. The study focuses on the impact of mutual electrostatic interactions on the structure of the EHD flow, a subject that has received limited attention in previous literature.

Finally, a novel application of ionic wind generated by corona discharge is studied for cleaning photovoltaic (PV) panels to address efficiency losses caused by dust accumulation. By combining numerical modeling with experimental validation, the study illustrates how geometric and operational parameters influence the efficiency and performance of EHD cleaning systems. The results provide a foundation for designing cost-effective and energy-efficient solutions for renewable energy applications.

Reference

[1] G. Fridman, G. Friedman, A. Gutsol, A. B. Shekhter, V. N. Vasilets, and A. Fridman, “Applied Plasma Medicine,” Plasma Processes and Polymers, vol. 5, no. 6, pp. 503–533, 2008, doi: 10.1002/ppap.200700154.

[2] B. Djemaa, Y. Benmimoun, B. Mohammed Fethi, S.-A. Kellal, and B. Fellah, “Comparative study of bacteria sterilization by cold plasma produced by DC generator with positive and negative polarity using atmospheric pressure,” PRZEGLĄD ELEKTROTECHNICZNY, vol. 1, Aug. 2020, doi: 10.15199/48.2020.12.10.

[3] B. L. Owsenek, J. Seyed-Yagoobi, and R. H. Page, “Experimental Investigation of Corona Wind Heat Transfer Enhancement With a Heated Horizontal Flat Plate,” Journal of Heat Transfer, vol. 117, no. 2, pp. 309–315, May 1995, doi: 10.1115/1.2822522.

[4] K. Ebihara et al., “Recent development of ozone treatment for agricultural soil sterilization and biomedical prevention,” Przeglad Elektrotechniczny, vol. 88, Jan. 2012.

[5] A. Draou, S. Nemmich, K. Nassour, Y. Benmimoun, and A. Tilmatine, “Experimental analysis of a novel ozone generator configuration for use in water treatment applications,” International Journal of Environmental Studies, vol. 76, no. 2, pp. 338–350, Mar. 2019, doi: 10.1080/00207233.2018.1499698.

[6] K. J. McLean, “Electrostatic precipitators,” IEE Proceedings A (Physical Science, Measurement and Instrumentation, Management and Education, Reviews), vol. 135, no. 6, pp. 347–361, Jul. 1988, doi: 10.1049/ip-a-1.1988.0056.

[7] M. F. Bekkara, L. Dascalescu, Y. Benmimoun, T. Zeghloul, A. Tilmatine, and N. Zouzou, “Modification of surface characteristic and tribo-electric properties of polymers by DBD plasma in atmospheric air,” Eur. Phys. J. Appl. Phys., vol. 81, no. 1, Art. no. 1, Jan. 2018, doi: 10.1051/epjap/2017170149.

[8] Y.-Y. Tsui, Y.-X. Huang, C.-C. Lan, and C.-C. Wang, “A study of heat transfer enhancement via corona discharge by using a plate corona electrode,” Journal of Electrostatics, vol. 87, pp. 1–10, Jun. 2017, doi: 10.1016/j.elstat.2017.02.003.

[9] L. Dascalescu, A. Tilmatine, F. Aman, and M. Mihailescu, “Optimization of electrostatic separation Processes using response surface modeling,” IEEE Transactions on Industry Applications, vol. 40, no. 1, pp. 53–59, Jan. 2004, doi: 10.1109/TIA.2003.821812.

[10] P. Béquin, K. Castor, and J. Scholten, “Electric wind characterisation in negative point-to-plane corona discharges in air,” The European Physical Journal - Applied Physics, vol. 22, no. 1, pp. 41–49, Apr. 2003, doi: 10.1051/epjap:2003006.

[11] D. F. Colas, A. Ferret, D. Z. Pai, D. A. Lacoste, and C. O. Laux, “Ionic wind generation by a wire-cylinder-plate corona discharge in air at atmospheric pressure,” Journal of Applied Physics, vol. 108, no. 10, p. 103306, Nov. 2010, doi: 10.1063/1.3514131.

[12] M. Robinson, “A History of the Electric Wind,” American Journal of Physics, vol. 30, no. 5, pp. 366–372, May 1962, doi: 10.1119/1.1942021.

CHAPTER I : The Generation of Electric Wind by Corona Discharge and Its Applications

Ionic wind, an induced phenomenon during corona discharge, possessing the features of silent operation and no moving parts, has a wide range of applications. Ionic wind generation is accompanied by complex physical processes, involving gas ionization, ion recombination, flow, and various chemical reactions, as well as mutual couplings between some of them. Therefore, understanding the corona discharge process and ionic wind generation is crucial for researchers and engineers to better utilize this phenomenon in practical applications. In this chapter, the principles of corona discharge and its induced ionic wind are presented. Subsequently, the challenges of transitioning the ionic wind technology from laboratory studies to practical applications are discussed. These challenges include the excessively high onset voltage of the corona, ozone emission, and influence of environmental conditions. Finally, some future research prospects and the conclusions are presented.

I.1 Introduction

Ionic wind is a physical phenomenon produced by corona discharge in a gas at atmospheric pressure and belongs to a type of low-temperature plasma in plasma science. The physical nature of ionic wind is the conversion of electrical energy into mechanical energy of fluid flow. Its microscopic principle is the momentum transfer from ions produced in the discharge to neutral molecules or atoms through collisions between them, thus resulting in a type of airflow. The main characteristics of this electrohydrodynamic (EHD) effect are silent operation [1-4], no moving parts, fast response [5, 6], low-cost maintenance [7], low-energy consumption [8], and compact structure [9]. Its generation principle and characteristics indicate that it has a wide range of applications in many fields, such as heat transfer enhancement[10-12], electrostatic precipitation [13, 14], food drying [15, 16], water collection [17, 18], aerodynamic flow control [19, 20], and electric propulsion [21, 22].

I.1.1 History of ionic wind

The earliest report concerning this EHD effect dates back to 1629 when Niccolo Cabeo, an Italian and contemporary of Galileo, noticed that sawdust could be attracted to an electrified body, touch it, and then be repelled [23]. However, Cabeo did not truly understand its mechanism, and the circulatory wind hypothesis Cabeo made was disapproved by the Irish natural philosopher Robert Boyle several decades later [24]. Actually, this is a phenomenon related to electrostatic forces, and it can occur in vacuum conditions as well as in air. Corona discharge can occur under variable air pressures [25, 26], either below the standard atmospheric pressure [27], However, ionic wind cannot be generated in a purely vacuum condition, because there are no charge carriers for collisions without air. The pressure can affect the discharge mode [28], ionization [29], and onset and average currents [30], which are closely related to the ionic wind flow. Indeed, the observation of ionic wind could not have occurred earlier than the invention of a high-voltage generating machine. It was not until 1672 that Otto von Guericke, who is famous for the Magdeburg hemispheres, fabricated a fractional sphere mounted on a crankshaft and observed that the rubbed sphere glowed in the dark [31]. This is the earliest recorded observation of corona discharge, but ionic wind was not mentioned by Guericke. The first discovery of the EHD phenomenon acknowledged by the public is attributed to Francis Hauksbee, curator of instruments for the Royal Society of London, who perceived a weak airflow blowing to his face when he held a charged tube toward himself in 1709 [32]. Several years later, Isaac Newton repeated Hauksbee's experiment and named this phenomenon electric wind [33]. In 1750, Benjamin Wilson, secretary to the Royal Society, succeeded in producing the rapid rotary motion of a pinwheel by directing the electric wind from a point discharge against it. Afterward, Hamilton, professor of philosophy at the University of Dublin, modified Wilson's apparatus to a single-stage device, which consisted of an S-shaped wire suspended horizontally at its center on an electrically conducting shaft. The two ends of the S-shaped wire were sharpened to points, from which the discharge occurred when high voltage was applied to the shaft, causing the S-shaped wire to spin around its axis. Although there were experimental observations on ionic wind at that time, scientists did not study or explain this EHD effect due to the lack of physical knowledge and technology.

The first explanation of the EHD phenomenon was provided by Tiberius Cavallo, an Anglo-Italian natural philosopher. He pointed out that the air opposite to the points of wires acquired strong electricity and repelled the points of the wires when describing the repulsion in the motion of a fly in 1777 [34]. Michael Faraday published his observations on electric wind in 1838 and explained that it is a momentum-transfer process by friction or collision between charged and uncharged gas particles [35]. Faraday's publication is a milestone in understanding the mechanisms of ionic wind. Afterward, August Töpler, inventor of schlieren optics, used his new technique to study the flow patterns of the electric wind. In 1873, James Clerk Maxwell qualitatively analyzed the mechanism of electric wind [36]. He pointed out that when the electric intensity in the neighborhood of the discharge point reaches a certain limit, the air insulation is broken. Subsequently, the electricity accumulates in the air around this point, and the charged particles of air tend to move away from the electrified body because they are charged with the same type of electricity. Maxwell's study provided the most complete theory on the EHD phenomenon contemporaneously, much of which remains valid today, despite the fact that no rudimentary mathematical treatment was applied to this theory.

The aforementioned studies only conducted a qualitative analysis on the generation and mechanism of ionic wind and lacked relevant quantitative studies. This situation continued until the end of the 19th century when Chattock conducted the first quantitative experimental study on the relationship between pressure and electric current for the electric wind induced by a configuration of parallel plane electrodes [37]. In 1954, Löb extended the pressure–current equation of Chattock's study to other geometries [38]. Soon after, Harney examined the electrical parameters of a corona discharge and found that the effect of electric wind on these parameters is small unless the air is substituted by a dielectric liquid [39]. Subsequently, Robinson conducted an in-depth experimental study of the generation and influencing factors of ionic wind in 1961 [40]. One year later, Otmar Stuetzer summarized and expanded the studies of Löb and Harney, offering the most complete explanation of the EHD phenomenon [41]. The EHD effect has various names, such as electric wind (named by Newton), corona wind (named for its generation by a corona discharge), and ionic wind (more common nowadays), since it was first observed and recorded by Hauksbee. In the three centuries from its first discovery, many scientists and engineers conducted various studies on ionic wind, including many scientific giants (such as Newton, Faraday, and Maxwell). Robinson reviewed the history of the EHD phenomenon study in detail [24]. These significant contributions have made the mechanism of ionic wind generation clearer and more recognized by the scientific community. These research results have also laid a solid foundation for the subsequent application of ionic wind technology in various fields.

I.1.2 Different Techniques for Generating Ionic Wind

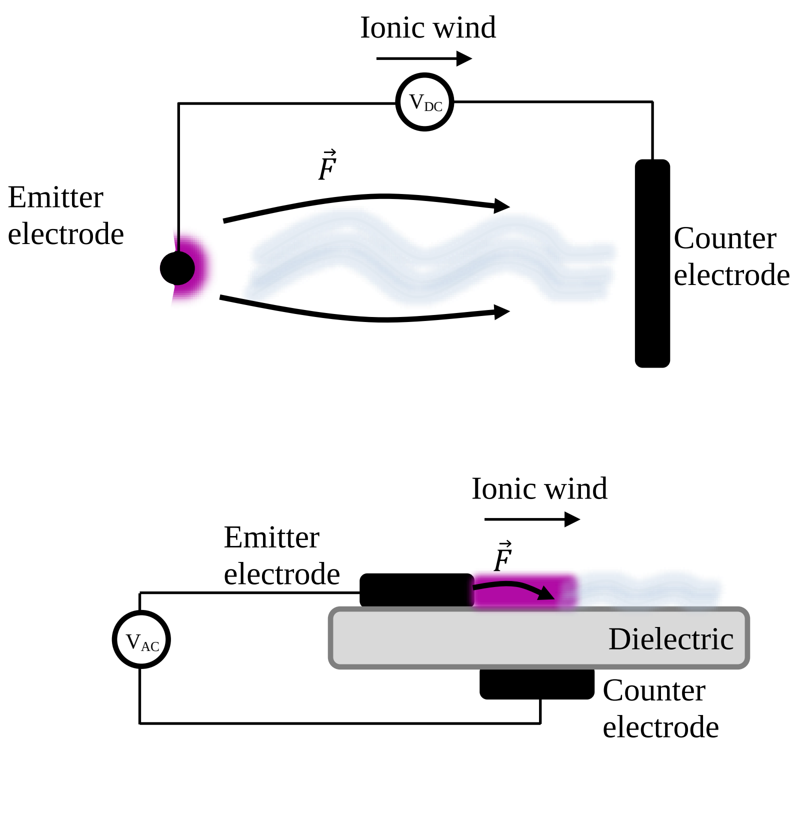

Figure I.1 Schematic of ionic wind generation: (a) corona discharge; (b) dielectric barrier discharge (DBD).

From a qualitative perspective, ionic winds can be visualized as shown in Figure I.1 for both a corona discharge (Figure I.1(a)) and DBD (Figure I.1(b)). Regardless of the discharge mode, the basic mechanism of ionic wind formation is the same – momentum transfer from ions produced in the discharge to neutral gas molecules. However, as corona discharges are primarily DC and DBD are inherently AC, there are some interesting fundamental differences between the two.

I.1.2.1 Generation of Ionic Wind by Corona Discharge

A corona discharge is a highly localized discharge that is generated by applying high voltage between a sharp emitter electrode and a blunt counter electrode (Fig. I.1(a)). Common geometries include a point to plane (pin or needle electrode to flat plate electrode), wire to plane, and wire-to-wire (where the symmetry plane serves as a virtual blunt electrode). The sharp-to-blunt electrode configuration produces a highly nonuniform electric field that serves to localize much of the ionization and plasma generation to a very small region around the sharp electrode. Since the electric field is only sufficient to breakdown the gas near the sharp point (~3×10^6 V/m for air [42]) the discharge is effectively localized and thus can be generated without an external ballast resistor in the circuit. The localized plasma region also serves to inhibit sparking, which is typically what occurs when high voltage is applied at atmospheric pressure. At atmospheric pressure, corona discharges are inherently filamentary [43, 44], consisting of short, transient streamers that are self-limiting. However, at steady state, corona discharges appear completely stationary, with the visible portion of the discharge confined to the localized plasma region near the emitter electrode. The exact nature of the filamentary behavior depends strongly on the polarity of the discharge; in positive polarity (positive emitter electrode) the filaments consist of streamers at a frequency of ~10^4-10^6 Hz, whereas in negative polarity (negative emitter electrode) the discharge consists of regular Trichel pulses [19, 45]. In the context of EHD pumps, the steady state behavior of the corona discharge is most relevant, and the discharge is considered stable from an onset voltage up to a peak allowable voltage where the field in the entire gap exceeds breakdown and sparks ultimately occur. The average current is essentially steady and increases monotonically with voltage. (Note that at sufficient time resolution, it consists of a number of short pulses corresponding to the filamentary behavior of the discharge [43].) Unlike the common DC glow discharge, there is no voltage drop after the onset voltage is reached, and the discharge voltage can continue to be increased until sparkover. Typically, ranges of operation are on the order of kV to tens of kV producing currents ranging from μA to mA, and the ionization fraction is extremely small with charge densities ~10^{13} cm^3 within the ionization region that quickly fall off to ~10^9 cm^3 across the space between the electrodes [46].

I.1.2.2 Generation of Ionic Wind by Dielectric Barrier Discharge (DBD)

A dielectric barrier discharge (DBD) is different than a corona discharge, both in geometry and operation. The basic configuration consists of two metal electrodes where one or both the electrodes is covered by a dielectric solid. Although many geometries are possible [47], for flow generation the preferred geometry is a surface DBD consisting of two electrodes, one exposed and one buried within a dielectric layer (Fig. I.1(b)), with Teflon, Kapton, and similar polymer materials being common dielectric materials of choice. The DBD is actuated with an AC voltage, and as the voltage rises a surface discharge is struck in the small volume between the exposed electrode and the dielectric on which it sits. As the charge carriers in the discharge accumulate on the dielectric, they produce a surface voltage that compensates the applied voltage, effectively extinguishing the discharge. As the applied voltage switches polarity in the second half of the AC cycle, the charges on the dielectric are removed, allowing for the discharge to again ignite until charge carriers of the opposite polarity accumulate on the dielectric and again extinguish the discharge. The presence of the dielectric allows for this sequence of ignition compensation extinction to occur on its surface. The dielectric is essential to inhibit sparking, especially at atmospheric pressure, but also requires the voltage to constantly switch polarity to maintain a pseudo constant discharge. Thus, in contrast to a corona discharge, which uses spatial inhomogeneity to stabilize the discharge and inhibit sparking, a DBD is stabilized temporally. In comparison to a corona discharge, the voltages are also on the order of kV to tens of kV but produce greater currents densities, in the range of 100-1000 A/cm^2 [48, 49] near the electrode dielectric interface, but the ionization fraction is still relatively small. From a flow generation perspective, the same process of ions colliding with neutral molecules occurs in a DBD, and the same air ions found in corona discharges are for the most part also found in a DBD. The nature of the geometry in the discharge volume between the exposed electrode and dielectric surface plays an important role in defining the flow direction, and unlike a corona discharge driven ionic wind, the flow in a DBD is generated along the surface, akin to a wall jet, rather than in a large bulk volume. While one might presume that the flow would oscillate given the AC nature of the discharge, it has been shown that in air the flow is always in the direction away from the exposed electrode, and this can be attributed to the negative ions in the discharge [50, 51]. Thus, like a corona discharge, the flow is always generated in the same direction and the net effect is a constant wall jet along the dielectric surface.

I.1.2.3 Importance of Corona Discharge in Generating Electric Wind

The importance of corona discharge in generating ionic winds lies in its higher efficiency, simpler design, and ability to produce effective airflow without the need for complex structures. Corona discharge operates at high voltage with low current, making it more efficient in converting electrical energy into airflow compared to DBD, which requires more intricate designs and suffers from higher energy losses. Additionally, corona discharge can generate focused and strong ionic winds using simple electrodes such as wires or sharp tips, whereas DBD relies on more complex structures like insulated electrodes. These features make corona discharge more suitable for practical applications that demand high efficiency and straightforward design.

The advantage of corona discharge is its ability to operate with all types of electrical power supplies. The main challenge associated with this type of discharge is the transition to an electric arc [52]. This transition is accompanied by a significant increase in the current flowing through the discharge and a rise in gas temperature, resulting in the generated plasma being close to thermodynamic equilibrium. Consequently, the power injected into the gas is predominantly dissipated through Joule heating.

In most applications utilizing corona discharges, efforts are made to avoid the transition to an arc to prevent electrode deterioration and to optimize the generation of active species based on the injected energy.

I.2 Fundamentals of Corona Discharge

I.2.1 Definition

In corona discharge, ionic wind is generated through momentum exchange between particles in a gas corona discharge, and thus its flow characteristics are closely related to the corona discharge process. Corona is a weakly luminous discharge, which occurs in a highly non-uniform electric field generated between two electrodes with small radii of curvature (at least one of them has a small radius of curvature, e.g., a sharp-to-blunt electrode configuration, two thin wires or edges). The electric field in vicinity of one or both electrodes should be much stronger than in the rest of the discharge gap [53]. Coronas are always nonuniform: strong electric field, ionization, and luminosity are located in the vicinity of a single electrode. Weak electric fields drag charged particles to another electrode to close the circuit.

Corona discharge is a type of self-sustained discharge, but it is different from the situation in a uniformly distributed electric field: once a self-sustained discharge occurs in the interstitial gas between the two electrodes, it can immediately cause breakdown of the entire air gap. In the process of corona discharge, the uneven distribution of electric field confines the ionization and plasma generation to the vicinity of the tip of the emitting electrode in which the electric field strength is extremely high, and a self-sustained discharge occurs. However, most of the other areas in the interstitial gas between the two electrodes are not ionized and maintain considerable insulation, causing the self-sustained discharge process to be stable.

The current of a corona discharge mainly depends on the electrical conductance of the interstitial gap between the anode and the cathode, that is, it depends on the applied voltage, electrode geometry, inter-electrode gap (the distance between the emitting electrode and the collecting electrode), and the physical properties of the gas, etc. [54, 55].

I.2.2 Mechanism of Corona Discharge

I.2.2.1 Sources of Seed Electrons

The establishment of an electrical discharge in a gaseous space subjected to a potential requires the presence of free charges in the medium: seed electrons. These free electrons present in the gaseous medium gain energy under the influence of the external electric field and lose energy due to elastic and inelastic collisions with particles present in the gas. These seed electrons can originate from several sources, including:

- **Cosmic Radiation or Natural Radioactivity**

Under the effect of irradiation by cosmic rays or natural radioactivity processes, 7 to 20 electrons per cm^3/sec are produced in air at atmospheric pressure [56].

- **Detachment of Electrons from Negative Ions**

This is the primary process of electron production from negative ions. These ions may pre-exist in the inter-electrode space, particularly in the presence of impurities such as O_2 or H_2O. The main contributors to seed electrons will be negative ions like $O_2^-(H_2O)_n$ or $H_2O^-(H_2O)_n$, which are associated with impurities [57, 58].

- **Field Emission**

When the local electric field near the conductor is extremely high (such as near sharp edges or points), electrons can be directly emitted from the electrode surface due to quantum tunnel effect [59].

- **Secondary Electron Emission**

Electrons can be ejected from a surface when energetic ions or photons strike it, contributing to the supply of seed electrons. The secondary electron yield depends on the material, impact energy, and incident particle type [60].

I.2.2.2 Development of Discharge in Inter-Electrode Gaps: Streamer Theory

In Townsend's theory, cathodic emission processes play a fundamental role in the initiation of self-sustained discharge. However, this theory fails to explain the measured discharge development times (ranging from 10^{-9} to 10^{-7} s) in cases involving large inter-electrode gaps and high pressures. These times are significantly shorter than those required for the appearance of secondary effects at the cathode, which condition the transition from non-self-sustained to self-sustained discharges (typically 10^{-5} to 10^{-4} s). Furthermore, the breakdown voltage for spark initiation in large gaps does not depend on the cathode material, contrary to what is predicted by Townsend's theory.

To explain the mechanism of discharge development in large inter-electrode gaps, L. B. Loeb and J. M. Meek [61] proposed a model in which photoionization, resulting from excitation and recombination phenomena in the inter-electrode space, and space charge effects are the key factors driving discharge development (Figure I.2). According to this model, the discharge develops in the form of a highly conductive channel known as a streamer (plasma channel) [62].

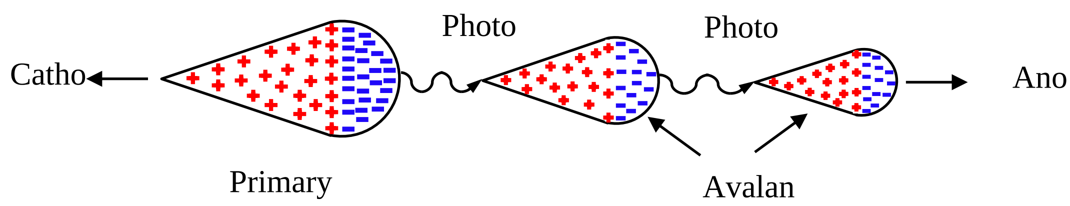

Figure I.2. Diagram of discharge development through photo-ionization.

- **Primary Avalanche and Space Charge Formation**

The initial stage of streamer discharge development corresponds to the formation of a primary avalanche, which is triggered by ionizing collisions when the local electric field exceeds a critical value at any point within the inter-electrode gap. This avalanche is accompanied by the formation of a space charge. In an avalanche, electrons form a negatively charged cloud that rapidly drifts toward the anode, whereas the much heavier positive ions remain nearly immobile due to their low mobility. This results in a highly non-uniform electric field, with intensified field strength near the avalanche poles, particularly around the positive pole, which consists of positive ions and acts like a conductive tip. Meanwhile, the electric field decreases along the avalanche flanks.

Once the space charge associated with the primary avalanche reaches a critical size (~10^8 electrons), it enhances ionizing collisions at both the leading edge and the tail of the avalanche. Within the avalanche, some electrons and ions recombine, emitting radiation that can induce photoionization of gas molecules both inside and outside the avalanche. The newly generated electrons may then initiate secondary avalanches, provided the local electric field remains sufficiently strong. These secondary avalanches, in turn, generate additional positive space charge ahead of the primary avalanche, sustaining the discharge process.

- **Avalanche Propagation and Streamer Formation**

The secondary avalanches play a crucial role in both sustaining the self-sustained discharge and amplifying the number of free charge carriers. The amplification process primarily occurs along the field axis and in the direction of the preceding avalanche. Each avalanche continues its own rapid development, forming a cascading effect. Even before the initial avalanche has fully developed, a chain reaction of new avalanches emerges.

As electrons move toward the anode, the avalanche chain appears to propagate toward the cathode. However, the progression of the discharge is extremely fast because avalanches are transmitted by radiation rather than by electron or ion migration. This means that ionization occurs without direct involvement of the cathode. Consequently, the discharge takes the form of a plasma channel aligned with the electrode axis, and its development depends on the local field distribution.

- **Thermal Effects and Streamer Maintenance**

During elastic collisions with gas molecules, free charges transfer part of their kinetic energy, leading to an increase in gas temperature. However, as long as this temperature remains below the threshold required for thermal ionization, it has no significant impact on the discharge process. This stage of the discharge is referred to as the streamer phase. The external field required to sustain the streamer is lower than the critical field necessary for ionization by collisions.

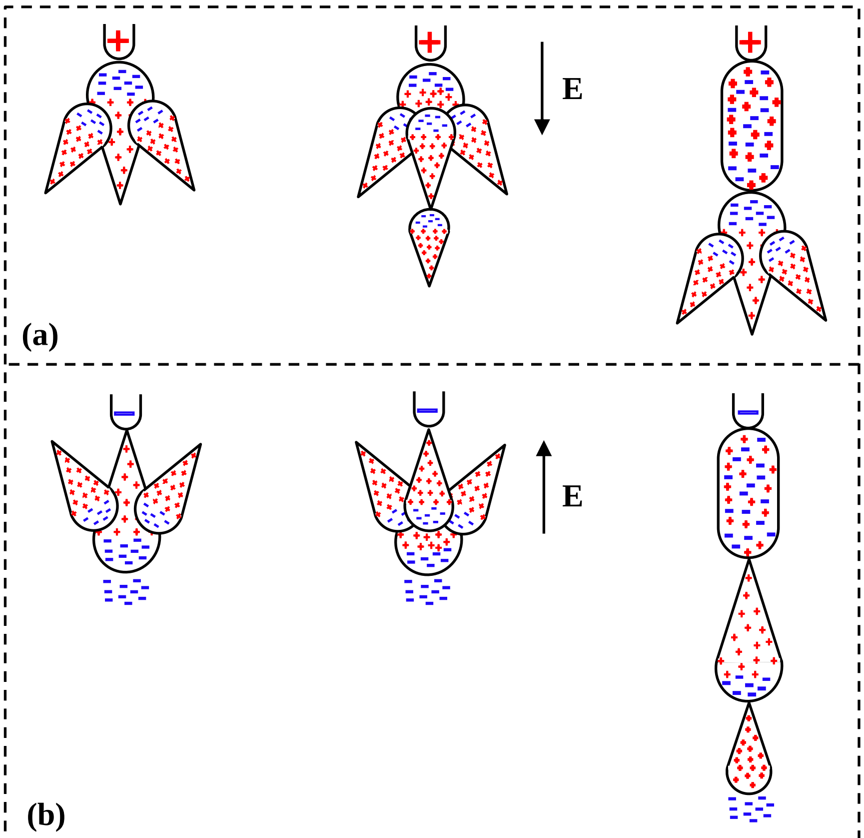

Figure I.3. Successive stages of streamer development in a gas with a point-to-plane electrode configuration: (a) positive point; (b) negative point [64].

For example [63], in air:

➢ The average field required for a streamer propagating from the anode is approximately 5 kV/cm.

- The field for a streamer originating from the cathode is about 15 kV/cm.
- The critical ionization field is around 30 kV/cm under standard pressure and temperature conditions.

Figure I.3 illustrates the various stages of streamer discharge development. The plasma channel model for gas discharges is of considerable qualitative significance, as it provides a convincing framework for understanding the probability and mechanisms of discharge formation for large values of the product (pressure × gap distance) [61, 62].

I.2.3 Types of Corona Discharges

Corona discharges can be classified into two types: positive corona discharges and negative corona discharges, depending on whether the stressed electrode acts as the anode or the cathode. The operating mechanisms of each discharge type are described below.

I.2.3.1 Positive Corona Discharge

Positive corona discharge exhibits characteristics distinct from negative corona, particularly in terms of current waveforms and spatial development, as previously reported [65, 66]. Unlike the highly repetitive Trichel pulses observed in negative corona, the current waveforms in positive corona appear as a series of irregular, narrow pulses. The average current increases rapidly with increasing applied voltage until a spark occurs. In contrast to the diffuse nature of negative corona, positive corona propagates primarily along the central axis, forming a straight discharge channel that first appears ahead of the needle tip, as illustrated in Figure I.4(a) [67]. Compared to the discharge excited by negative polarity, positive corona exhibits stronger intensity in the central region but a much narrower discharge channel. A positive corona discharge occurs when the sharp electrode is brought to a positive potential while the plate is grounded. Naturally occurring free electrons in the inter-electrode space accelerate toward the sharp electrode, and in the ionization region—where the reduced electric field (E/N) exceeds 120 Td, as shown in Figure I.4(b)—ionization generates positive ions. These ions are repelled by the anode due to Coulomb forces, moving away from the sharp electrode within a distance of less than one millimeter. Beyond this region, the electric field becomes too weak ($<E/N = 120$ Td in air at atmospheric pressure) to sustain further ion generation, and the positive ions migrate toward the cathode. This unipolar zone, containing only positive ions, is referred to as the "drift region" Figure I.4(b). Unlike in negative corona, the corona region in positive discharge coincides with the ionization region. For

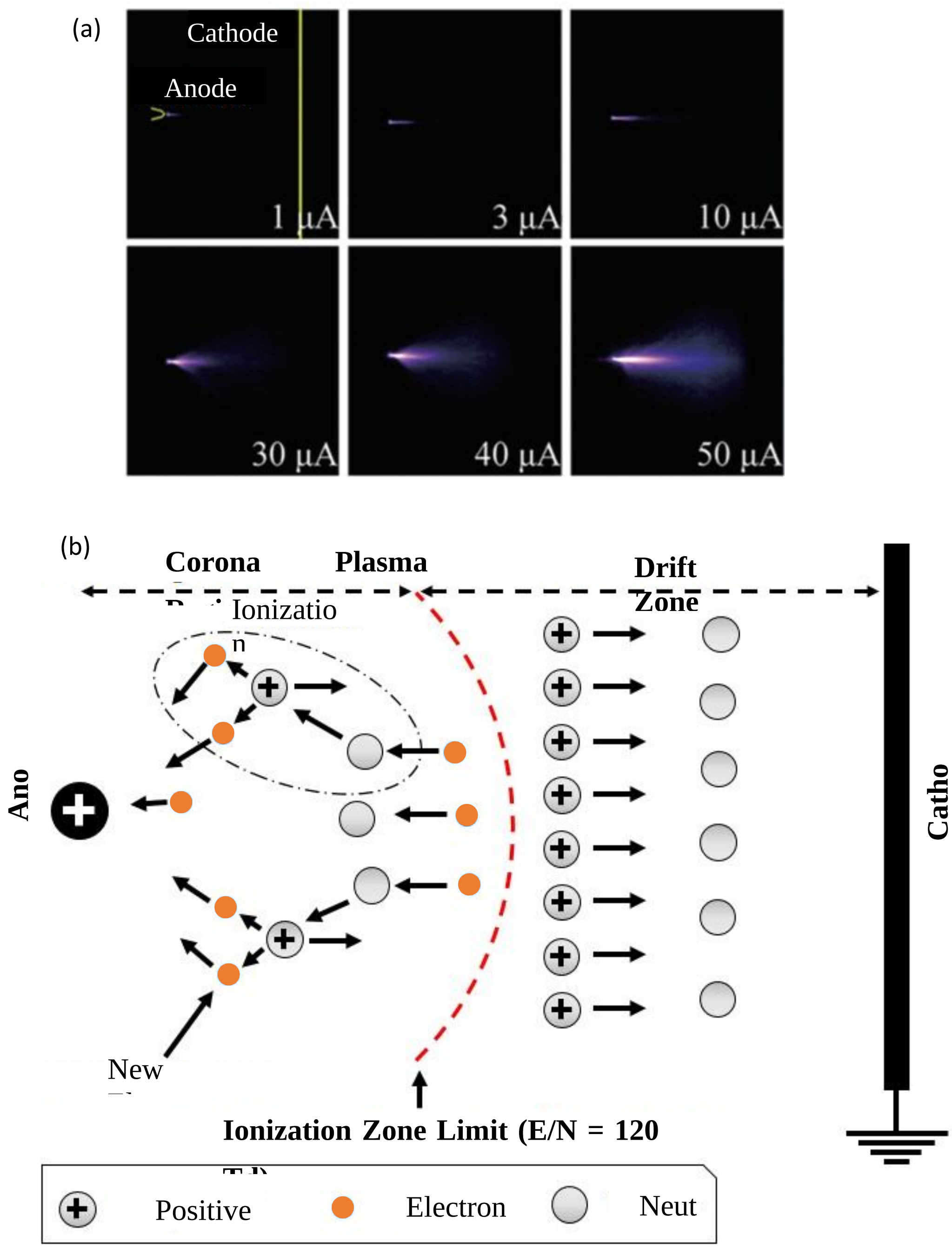

Figure I.4. Description of Positive Corona Discharge.

this type of discharge, streamers propagate as an extension of the anode. According to modeling studies referenced in [68], the discharge consists of two phases: the streamer propagation phase, which lasts approximately 50 ns at a velocity of 2×10^5 m/s, and the restoration phase, during which ions drift. Together, these phases form a cycle with a frequency of 10 kHz, leading to a transient discharge current rather than a continuous one. As indicated in [69], a positive current of 50 µA can be divided into a continuous unipolar current of 20 µA, uniformly distributed over the cathode surface, and alternating current streamers contributing 30 µA, impacting the cathode at a frequency of 10 kHz.

I.2.3.2 Negative Corona Discharge

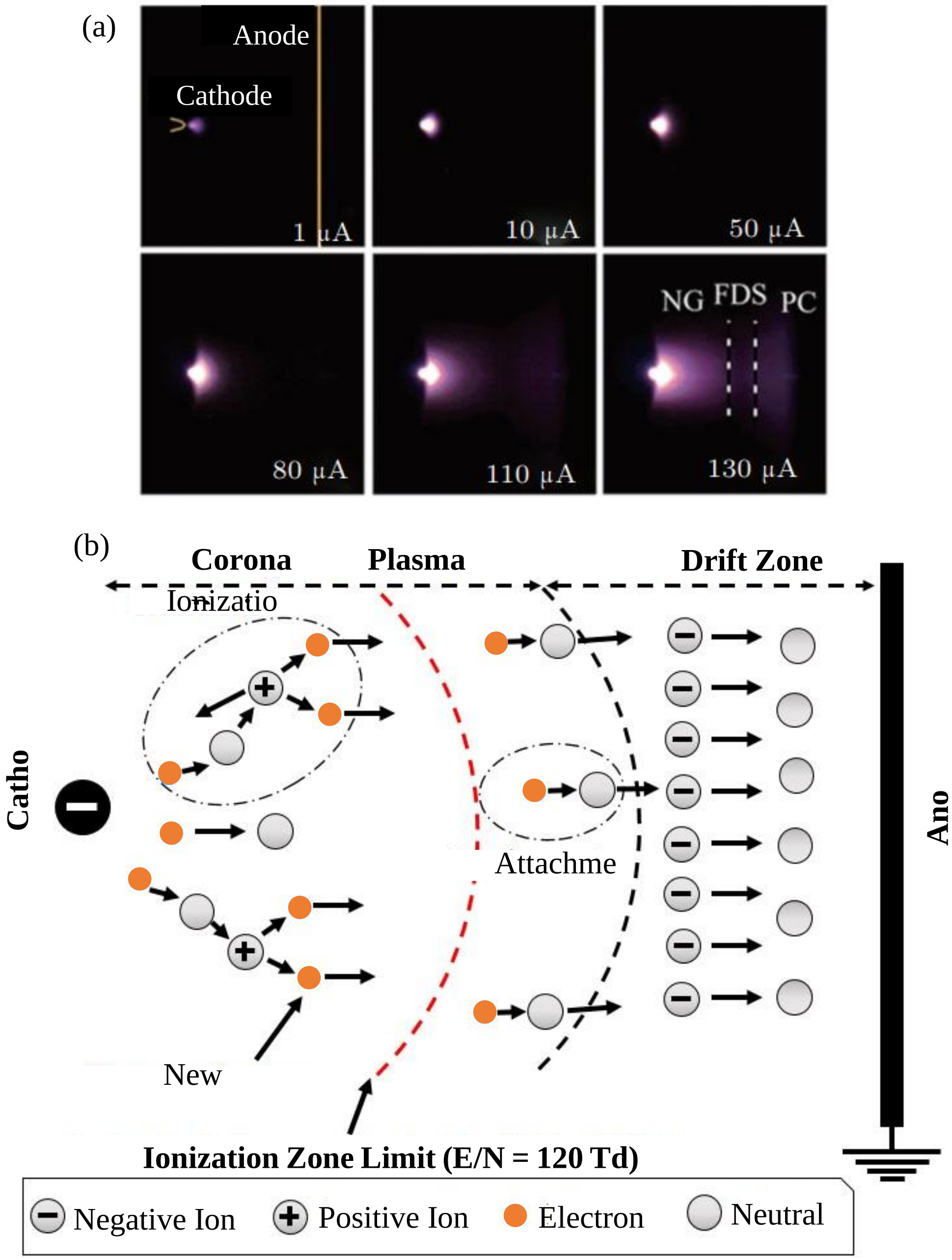

Figure I.5. Description of negative corona discharge.

During negative corona discharge, the development of the discharge generally progresses through three stages (Figure I.5(a)) [67]. In the Townsend stage (Stage 1), the discharge is weak but stable, sustaining a sub-microampere current through gradual electron multiplication via ionization collisions. However, secondary processes such as cathode emissions remain insufficient to accelerate ionization growth significantly. As the applied voltage increases, the discharge enters the Trichel pulse stage (Stage 2), where self-sustained and highly repeatable current pulses appear due to the formation and dissipation of space charge regions near the cathode [4]. Electron avalanches momentarily reduce the local electric field, suppressing further ionization until the space charge dissipates, allowing the cycle to repeat (Figure I.5(b)). With further voltage increase, the discharge transitions into the stable glow stage (Stage 3), where a continuous, uniform glow discharge develops, characterized by three distinct regions: the negative glow near the cathode, the Faraday dark space with lower electron density, and the positive column extending toward the anode [67]. The current in this stage becomes steady and continuous, marking the establishment of a fully self-sustained discharge. If the applied voltage continues to rise beyond a critical threshold, the local electric field becomes strong enough to induce intense ionization avalanches, leading to a complete spark breakdown that bridges the gas gap, thereby marking the transition from corona to a high-current discharge mode.

I.3 Factors Influencing Electric Wind Production

The electric wind pattern can be influenced by many factors, including the electrodes geometry, the EHD force and the current-voltage characteristics. These factors can be categorized into three main types:

I.3.1 Influence of Voltage Waveforms on Ionic Wind Dynamics

The dynamics of ionic wind are strongly influenced by the characteristics of the applied voltage waveform, including its amplitude, frequency, and shape. The electric field generated by the voltage waveform governs the ionization process, ion mobility, and charge distribution, all of which affect the strength and direction of the induced airflow [70]. When a DC voltage is applied, the ionic wind remains steady, as the electric field continuously accelerates charged particles in a unidirectional manner. The airflow strength depends on the magnitude of the voltage, with higher voltages leading to increased ionization and stronger wind. However, excessive voltage can trigger spark breakdown, disrupting stable ionic wind generation [71].

In contrast, AC voltage waveforms introduce periodic variations in the electric field, causing oscillatory ion motion and intermittent wind patterns. At low frequencies, the ions have sufficient time to travel toward the oppositely charged electrode before the polarity reverses, resulting in a quasi-steady airflow with reduced efficiency compared to DC-driven wind. At higher frequencies, ion drift is limited, leading to weaker wind production.[72]. Overall, the selection of the voltage waveform plays a critical role in controlling ionic wind characteristics.

I.3.2 Effects of Environmental Conditions

I.3.2.1 Effect of Temperature

The variation of ambient temperature influences the electric wind generated by an electric discharge by affecting ionization processes, gas density, charge mobility, and airflow dynamics. These changes impact the strength, velocity, and stability of the electric wind [73] ,[74], [40], [75]. The key effects are as follows:

- **Ionization and Charge Mobility**

As ambient temperature increases, gas molecules gain more thermal energy, leading to more frequent collisions between charged particles and neutral molecules. This can enhance ionization in some cases by increasing electron impact ionization rates. However, at very high temperatures, recombination processes may also accelerate, leading to a reduction in free charge carriers. Additionally, charge mobility increases with temperature because the reduced gas density lowers the resistance to ion motion. As a result, higher temperatures can improve the movement of charge carriers, potentially enhancing the electric wind strength.

- **Gas Density and Breakdown Voltage**

According to the ideal gas law, air density decreases with increasing temperature when pressure is constant. Since electric wind is driven by ion-neutral collisions, lower air density results in fewer available neutral molecules for momentum transfer, which can weaken the wind. Furthermore, the breakdown voltage of air decreases at higher temperatures because the increased mean free path of electrons facilitates ionization. This means that corona discharge can be initiated and sustained at lower electric fields, which can alter the behavior of the electric wind.

- **Momentum Transfer and Electric Wind Velocity**

The electric wind is generated through the transfer of momentum from moving ions to neutral gas molecules. At higher temperatures, neutral molecules move faster due to increased thermal energy, which can enhance the diffusion of ions. However, the reduced gas density leads to a lower total mass of neutral molecules per unit volume, potentially reducing the efficiency of momentum transfer. This trade-off between increased charge mobility and decreased mass of neutral molecules affects the overall velocity and intensity of the electric wind.

- **Buoyancy Effects and Convective Currents**

Temperature variations introduce buoyancy forces, which create natural convective currents that can interact with the ion-induced electric wind. In warmer conditions, hot air rises due to lower density, which can distort or enhance the airflow pattern generated by the discharge. In applications such as electrohydrodynamic cooling, combining electric wind with natural convection can improve heat dissipation. However, in other cases, these temperature-induced buoyancy effects may disrupt the directional flow of the electric wind, leading to turbulence and instability.

I.3.2.2 Effect of Humidity

Humidity plays a crucial role in modifying the characteristics of electric wind produced by an electric discharge. The presence of water vapor in the air influences ionization, charge mobility, and momentum transfer, thereby affecting the strength and velocity of the electric wind [76], [77], [78], [79]. The following factors describe the impact of humidity:

- **Ionization and Charge Mobility**

The presence of water vapor in humid air leads to the formation of molecular clusters around ions, increasing their effective mass and reducing their mobility. Additionally, water molecules readily capture free electrons, forming negative ions such as H_2O^- and OH^-, which reduces the number of free electrons available for ionization. This electron attachment process suppresses secondary ionization, thereby weakening the intensity of the electric wind. Since charge carriers become less mobile, the rate of ion drift decreases, leading to a reduction in ion-induced airflow.

- **Breakdown Voltage and Discharge Characteristics**

Humidity increases the breakdown voltage of air, making it more difficult for a corona discharge to initiate and sustain. Water vapor influences the mean free path of electrons, increasing the energy required for ionization. As a result, at a given applied voltage, the discharge strength is reduced, which in turn diminishes the production of ions and weakens the electric wind. The suppression of corona discharge under high humidity conditions has been observed in several experimental studies, where higher humidity levels require stronger electric fields to maintain discharge activity.

- **Momentum Transfer and Airflow**

Electric wind is generated by ion-neutral collisions, where charged ions accelerate neutral air molecules, inducing bulk air movement. Under humid conditions, the clustering of ions with water molecules increases their effective mass, reducing their acceleration and weakening their ability to transfer momentum to neutral molecules. Consequently, the airflow velocity of the electric wind decreases. Studies indicate that in high-humidity environments, the reduction in electric wind velocity can be significant, sometimes dropping by more than 30% compared to dry air conditions.

- **Surface Effects and Corona Discharge Stability**

Humidity can also influence the electrode surface conditions, particularly in corona discharge setups. Water vapor adsorption on metal electrodes can alter the local electric field distribution, sometimes leading to a more stable corona discharge. However, in extreme cases, condensation or surface ionization effects can result in local charge redistribution, which may destabilize the discharge process. These changes in corona discharge behavior directly impact the generation and strength of the electric wind.

I.3.2.3 Effect of Pressure

Pressure significantly impacts the characteristics of electric wind produced by an electric discharge. Variations in pressure influence ionization processes, charge carrier mobility, gas density, electron mean free path, and ion-neutral interactions, all of which determine the intensity and efficiency of the electric wind [80], [81], [82], [83]. The primary effects are outlined below.

- **Ionization and Charge Mobility**

At higher pressures, gas molecules are packed more densely, leading to more frequent electron-neutral collisions. This results in enhanced ionization but also increases electron energy loss, making it harder for electrons to reach the ionization threshold. At lower pressures, the mean free path of electrons increases, meaning they can gain higher energy before colliding with gas molecules, leading to more efficient ionization in weak electric fields. However, charge mobility decreases at high pressure because the increased gas density leads to more frequent collisions that slow down ion movement.

- **Gas Density and Mean Free Path**

As pressure increases, gas density also increases, meaning there are more neutral molecules per unit volume available for momentum exchange with ions. This can enhance the strength of the electric wind if charge mobility remains sufficient. - However, a higher density also shortens the mean free path of electrons, increasing the likelihood of energy loss in collisions before ionization occurs. At low pressure, the mean free path increases, allowing for more energetic electron collisions and easier ionization, but fewer neutral molecules per unit volume lead to weaker momentum transfer, reducing the effectiveness of the electric wind.

- **Momentum Transfer and Electric Wind Strength**

The electric wind is generated by the transfer of momentum from moving ions to neutral gas molecules. At high pressure, increased gas density leads to more frequent ion-neutral collisions, enhancing momentum transfer. However, lower ion mobility due to frequent collisions may counteract this effect. At low pressure, ions move more freely and gain higher drift velocities, but with fewer neutral molecules available, the overall strength of the electric wind may be reduced.

- **Breakdown Voltage and Discharge Stability**

Higher pressure increases the breakdown voltage of air because electrons lose energy more rapidly in frequent collisions, making it harder to sustain a discharge at a given electric field. At lower pressure, the breakdown voltage decreases because electrons can travel longer distances without colliding, allowing for easier ionization. Discharges in low-pressure environments, such as in plasma applications, often produce stronger electric wind due to the high mobility of charged particles.

I.3.3 Impact of Geometric Configurations of Electrodes

The geometric configuration of electrodes significantly impacts the performance of ionic wind by influencing ion generation, electric field distribution, and airflow characteristics. Key factors include:

I.3.3.1 Electrode Shape and Size:

Sharp electrodes (e.g., needle, wire) create intense localized electric fields, enhancing ionization and increasing wind velocity. However, larger or blunt electrodes (e.g., plates, cylinders) distribute the field over a wider area, reducing ion concentration and wind strength.

I.3.3.2 Electrode Spacing:

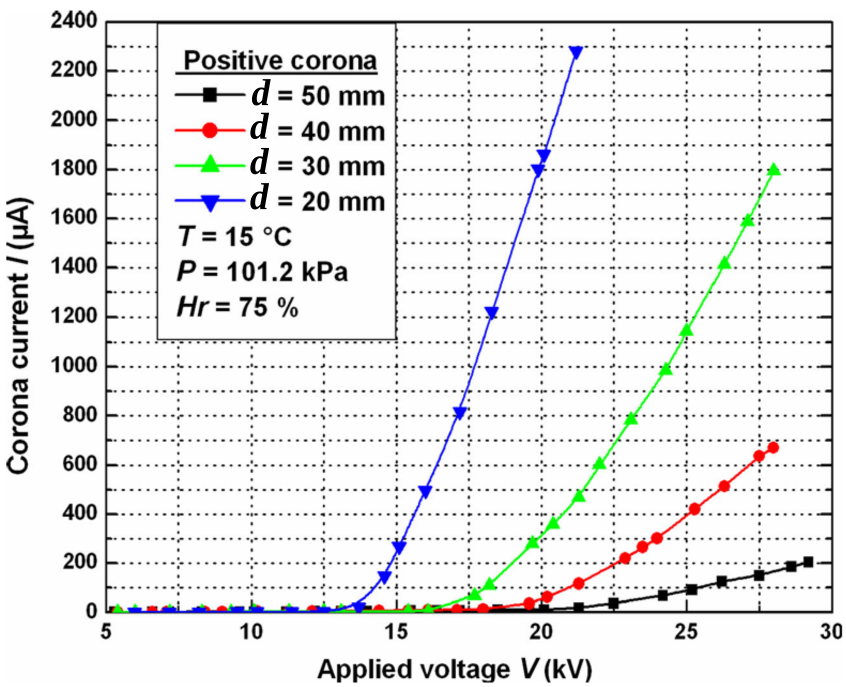

Figure I.6. Current-voltage characteristics as a function of inter-electrode distance. [84]

Smaller gaps lead to stronger electric fields and higher ion generation, but may also increase power consumption and the risk of electrical breakdown. In contrast, larger gaps reduce ionization efficiency but allow for a more uniform wind distribution. An example is shown in Figure I.6 [84], where the characteristic current-voltage curve is plotted for different inter-electrode spacings (0.5 cm, 1 cm, and 2 cm) in a Blade-to-Plane electrode configuration.

I.4 Applications of Electric Wind from Corona Discharge

I.4.1 Cooling and Thermal Management

Ionic wind, generated through electrohydrodynamic (EHD) forces, has various applications in cooling and thermal management, particularly in electronics, heat sinks, and LED cooling.

- **Electronics Cooling:**

In electronic cooling, the airflow generated by an electric discharge dissipate heat from components such as microprocessors, power electronics, and circuit boards by enhancing convective heat transfer.

One of the main advantages of using electric wind for electronic cooling is the absence of moving parts. Unlike traditional fans, which rely on mechanical rotation, the system operates silently and has no components that wear out over time. This significantly reduces maintenance requirements and increases the reliability of the cooling system. Additionally, the compact design of electric wind cooling makes it ideal for miniaturized electronic devices, where space constraints prevent the use of conventional cooling methods.

Another key benefit is its high efficiency. Electric wind can achieve effective heat dissipation with lower energy consumption compared to traditional fans. This makes it particularly useful for battery-powered and energy-sensitive applications. Furthermore, it allows for precise and localized cooling, making it possible to target specific hot spots on a circuit board without affecting other areas. Unlike fan-based cooling, which creates turbulence that attracts dust, electric wind cooling minimizes dust accumulation, maintaining long-term performance and reducing the risk of overheating.

A good example of electronic cooling using electric wind is LEDs cooling. Indeed, Light-emitting diodes (LEDs) are widely used for lighting and display applications due to their high energy efficiency and long lifespan. However, LEDs generate heat during operation, and if this heat is not efficiently dissipated, it can lead to reduced performance, color shift, and even premature failure. Traditional cooling methods, such as passive heat sinks and active fans, have limitations in size, efficiency, and noise. Electric wind cooling offers a promising alternative by enhancing heat dissipation using ion-induced airflow without mechanical moving parts. As shown in Figure I.7, the cooling process follows these steps:

- A high-voltage electric field ionizes air molecules near a small emitter electrode.
- The generated ions move toward a larger collector electrode, transferring momentum to neutral air molecules.
- The induced airflow enhances convective heat transfer, increasing the cooling rate of the LED.

Bulk flow augmentation refers to the enhancement of an existing airflow by adding momentum to it. In the context of ionic wind cooling, this occurs when the ionized air particles generated by an electric discharge interact with a pre-existing airflow, leading to an increase in velocity and improved heat transfer efficiency.

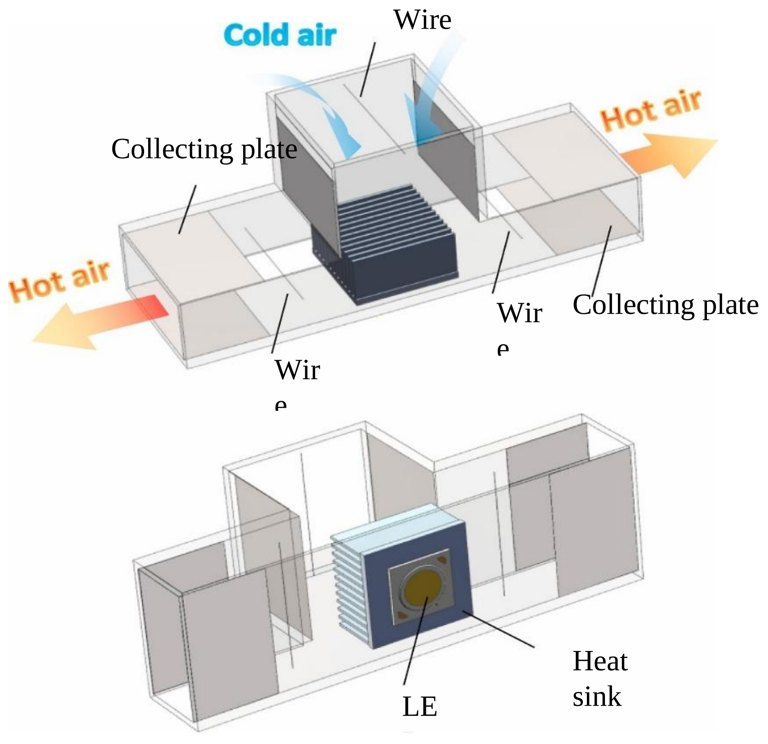

Figure I.7. Ionic wind pump used for cooling laminating LED chip.[5]

- **Mechanisms of Enhancement**

Momentum Injection into the Boundary Layer:

The boundary layer is the thin layer of air that forms near the surface of an object (such as a heated electronic component). Within this layer, airflow slows down due to viscosity, reducing heat transfer efficiency. Ionic wind injects additional momentum into this layer by accelerating neutral air molecules through ion-neutral collisions. This added momentum increases the velocity of airflow near the surface, reducing the thermal resistance and improving convective cooling.

Delaying Flow Separation:

Flow separation occurs when the airflow detaches from the surface of an object due to adverse pressure gradients, creating areas of low-velocity, recirculating air. This separation reduces effective cooling because stagnant air traps heat instead of carrying it away. Ionic wind can counteract this effect by energizing the near-surface flow, keeping it attached for a longer distance. The result is improved convective heat transfer and a more efficient removal of heat from electronic components.

Increasing Heat Advection:

Heat advection refers to the process of transporting thermal energy through bulk movement of air. By increasing the velocity of the cooling airflow, ionic wind enhances the ability of air to carry heat away from the surface. This effect is especially useful in applications where natural convection is insufficient, such as in compact electronic devices with limited airflow.

I.4.2 Particle Manipulation

Ionic wind, generated through electrohydrodynamic (EHD) forces, has significant applications in particle manipulation due to its ability to induce controlled airflow and charge-based interactions. Key applications include:

- **Aerosol Control and Filtration:**

The electric wind can be effectively used for aerosol control and filtration. The principle relies on ionizing air particles and generating airflow to manipulate and remove airborne contaminants such as dust, smoke, and pathogens. This technology has applications in air purifiers, cleanrooms, and industrial filtration systems. The mechanism of electric wind for aerosol control involves two key processes (See Figure I.8):

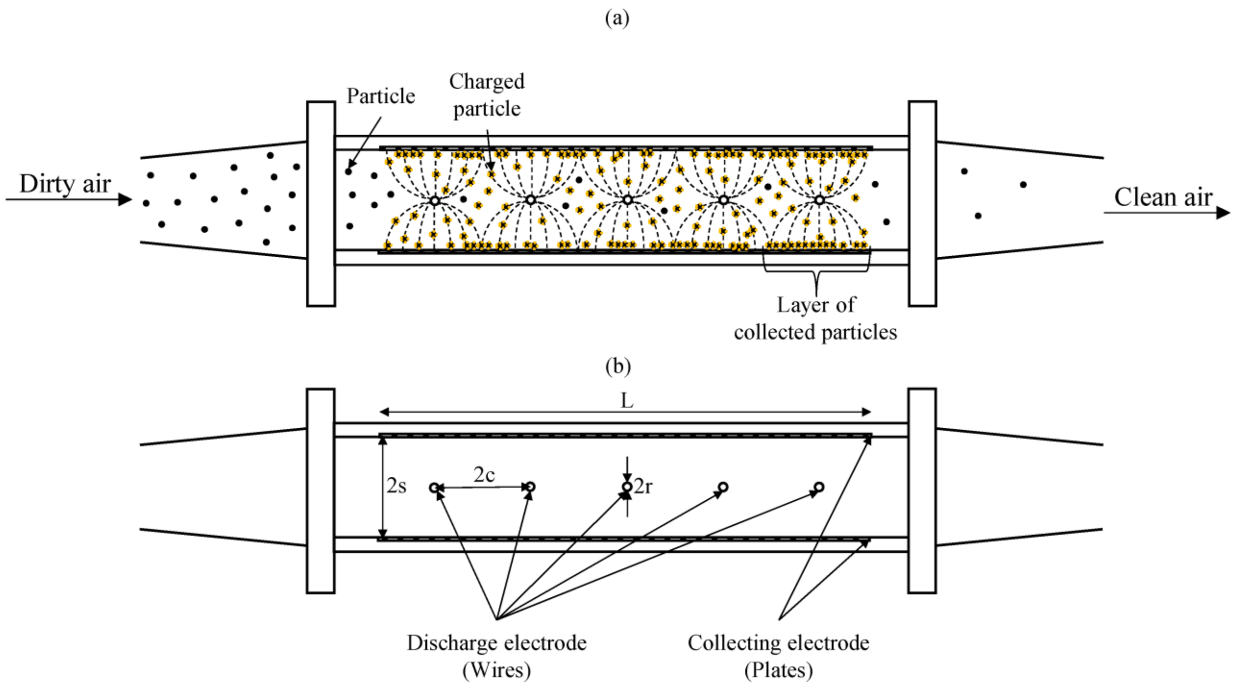

Figure I.8. (a) Representation of the electrostatic precipitation process and (b) the main dimensions and elements of a wire-plate electrostatic precipitator. [85]

a) Particle Charging: A high-voltage electrode ionizes air molecules, creating a region of charged particles (ions). These ions attach to airborne aerosol particles, charging them.

b) Electrostatic Precipitation and Airflow Enhancement: Once the aerosol particles are charged, they can be collected on oppositely charged surfaces (collector plates), effectively removing them from the air. Simultaneously, the electric wind induces a bulk airflow, improving the transport and dispersion of aerosols, which enhances filtration efficiency.

This dual-action approach enables efficient removal of fine particles, even at a microscopic scale, without the need for traditional mechanical fans or filters.

- **Microfluidic and Biomedical Applications:**

The electric wind can be efficiently used in microfluidic and biomedical applications [86-88]. It provides a non-mechanical method for fluid manipulation, particle transport, and enhanced cooling in lab-on-a-chip devices and medical instruments. The application of electric wind in microfluidics and biomedical systems is based on the ability of an electric field to generate airflow and influence particle or fluid motion at the microscale. For example, in biomedical applications, electric wind can be used to transport, separate, or collect micro/nanoparticles, such as cells, biomolecules, or aerosols. By adjusting the strength and configuration of the electric field, specific particles can be selectively moved or deposited in a controlled manner.

Electric wind can provide precise and localized cooling for temperature-sensitive biomedical devices, such as PCR (Polymerase Chain Reaction) systems and biosensors. It can also accelerate drying processes in sample preparation for medical and diagnostic tests.

The advantages of Electric Wind in Microfluidic and Biomedical Systems are:

- Precise and Contactless Fluid Control: Unlike mechanical pumps, electric wind can manipulate small volumes of fluid or particles without direct contact, reducing contamination risks.
- Silent and Energy-Efficient Operation: Since there are no moving parts, the system operates quietly and consumes less power, making it suitable for portable medical devices.
- Improved Mixing and Transport in Microfluidics: Enhances the mixing of reagents in microfluidic chips, leading to faster and more efficient biochemical reactions.
- Enhanced Cooling for Biomedical Instruments: Provides effective cooling for lab-on-a-chip devices, biosensors, and other heat-sensitive medical equipment.
- Non-Invasive and Safe for Biological Samples: Since electric wind does not require mechanical agitation or direct fluid contact, it is suitable for handling fragile biological samples like DNA, proteins, and live cells.

- **Powder Coating and Material Deposition:**

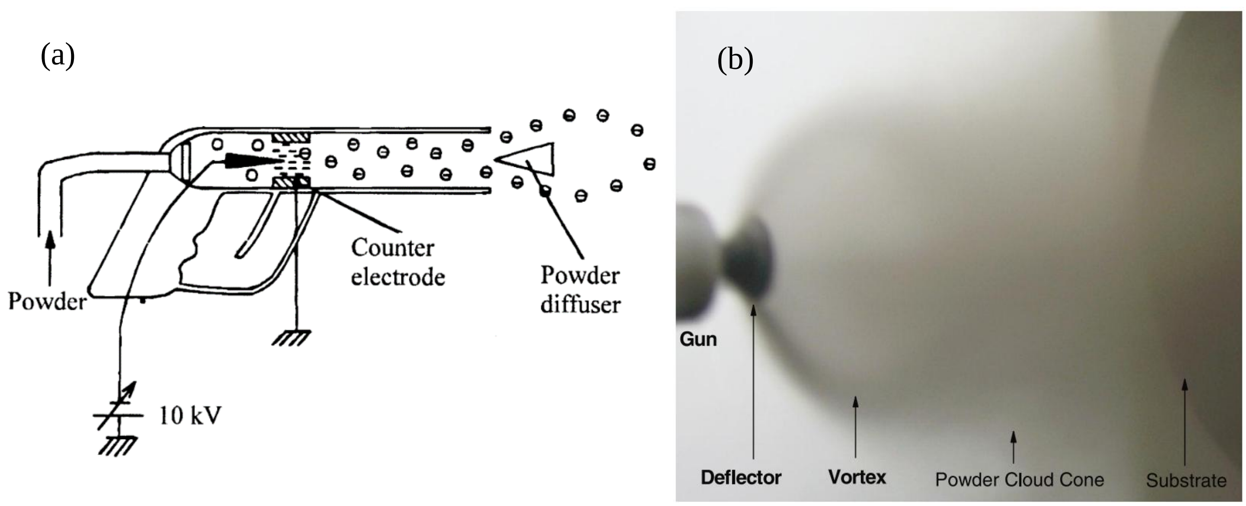

Figure I.9. (a):A conventional corona gun.[89]. (b):The pattern of powder cloud cone in powder coating processes [90].

The electric wind phenomenon can be utilized in powder coating and material deposition to improve the uniformity and efficiency of coating processes by controlling particle movement and deposition (see Figure I.9). The mechanisms involved are:

a) Electrostatic Charging and Particle Transport: A high-voltage electrode ionizes air molecules, creating charged ions. These ions transfer charge to powder particles (such as paint, polymers, or metallic coatings). Then, the charged particles are then attracted to the oppositely charged surface, ensuring efficient deposition.

b) Enhanced Powder Deposition Using Electric Wind: In addition to electrostatic attraction, electric wind enhances particle movement, ensuring a more uniform coating. Indeed, the ion-induced airflow distributes powder particles evenly, preventing clumping and improving adhesion. This effect is crucial for complex geometries; ensuring coating reaches recessed or hidden areas.

The advantages of Electric Wind in Powder Coating and Material Deposition are:

- Improved Coating Uniformity: Electric wind distributes powder particles more evenly, reducing defects and improving surface finish quality.
- Reduced Material Waste (Lower Overspray): By controlling powder movement, more material adheres to the surface, lowering costs and environmental impact.
- Better Coverage of Complex Shapes: Electric wind helps powder particles reach recessed or intricate surfaces, ensuring complete and uniform coverage.
- Enhanced Adhesion and Efficiency: The combination of electrostatic attraction and electric wind-induced movement improves the bonding of coating particles to surfaces.
- Environmentally Friendly and Energy Efficient: No need for compressed air or excessive heat, reducing energy consumption.

I.4.3 Electrohydrodynamic Propulsion

Just recently, on 21st of November 2018, a huge breakthrough was made by a team in MIT (Massachusetts Institute of Technology), where a team of engineers successfully performed a test flight of a drone with no moving parts, powered by ion thrusts (Figure I.10). While not exactly a lifter this craft proves that ionocraft have potential to be more than a fun science project. The teams final design was a large lightweight gilder, however the aircraft that has a giant long wing, underneath, two rows and 4 columns of wing long lifter thrusters, that consist of a wire set to a positive voltage of +20 kV, while behind it at a set distance there is an airfoil made of foam surrounded by aluminum foil set to a -20 kV [91]. The energized particles moving between them create a sort of wind effect that push the entire aircraft forward, and while it is unable to lift off unassisted, the possibility of extended periods of prolonged steady flight are available. The entire aircraft is super light weighing only at around 2.3 kg, while having an amazing 5-meter wingspan. In the fuselage of the plane are hidden stacks of lithium-polymer batteries. These are specially modified to provide the power to the six stage full-wave Cockcroft-Walkton voltage multiplier that they build in house to provide the 40 kV required to charge the wires and airfoils to create the electrical field required to accelerate the air particle around them.[92]

Another project that has been on the verge of breakthrough to mass EHD use is flying microrobot. Daniel S. Drew and Kristofer S. J. Pister at the University of Berkeley, California, have been working on micro scale flying craft for a few years now. Their vision is to use Electrohydrodynamic force to propel small drones, that could be used for a variety of applications, most important of which is search and rescue applications where swarms of drones could be used to look for survivors. Similar projects have been presented by Harvard University with their microrobots the Robobees [93], however, these types of devices use electromagnetic or piezoelectric mechanisms to flap the wings of the robot. This not only adds moving parts, but also increases the complexity of the device. These devices have a high level of degrees of freedom that is difficult to control when performing precise directional flight. With EHD devices there are no moving parts, they device is significantly easier to build, as well as the devices can use a quadcopter flight scheme that is extensively researched and has a variety of controller schemes available, instead of the highly unstable and hard to control winged device.

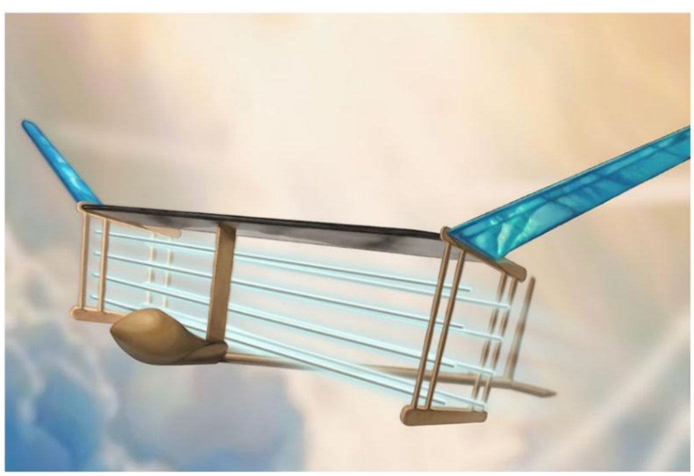

Figure I.10. MIT Ion powered drone plane [9]

I.4.4 EHD for Drying Applications

Drying food has been a predominant preservation technique since ancient times (Figure I.11). Most drying methods use heat to enhance mass transfer and drive moisture out of the food product; however, achieving high drying temperatures requires large amounts of energy and can degrade the quality of the product. Generating sufficient amounts of heat to remove moisture from products is such an energy intensive process it is said to be responsible for 10-20 % of the total energy used in the manufacturing industry [94, 95]. To reduce energy consumption, there is significant amount of interest in novel methods that can be used to dry food. Electric fields have been an active area of research for drying applications for decades after it was found that food products behave as a dielectric under an applied electric field, undergoing an exothermic interaction which can increase the rate of vaporization by up to 50× in the proper conditions [96, 97]. Additionally, an added EHD flow can enhance drying by modifying the boundary layer around the food product to enhance the mass transfer rate between the food and the air [98]. While the physical process is still not completely understood [99], EHD drying offers a nonthermal drying method that maintains high food quality while reducing energy consumption [100, 101].

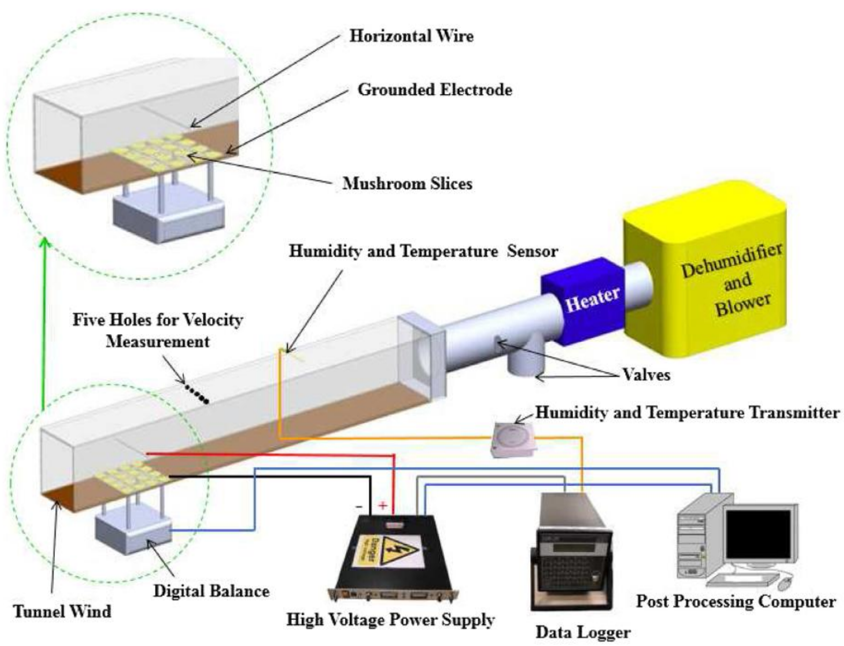

Figure I.11. A schematic of the configuration used to study EHD drying on mushroom slices, where a mushroom slice were placed under a corona discharge within a bulk air flow.[102]

I.4.5 Solar Panels Cleaning

Solar energy is a crucial component of the global transition to sustainable power generation. Photovoltaic (PV) panels convert sunlight into electricity, providing a clean and renewable energy source. However, maintaining their efficiency is a persistent challenge, particularly in arid and desert regions where dust accumulation significantly reduces their performance. Conventional cleaning methods, such as water-based washing or mechanical brushing, can be costly, labour-intensive, and environmentally unsustainable. To address this issue, Tilmatine's group in cooperation with our laboratory team have explored electrohydrodynamic (EHD) principles, specifically ionic wind cleaning, as a non-contact and energy-efficient method to remove dust from solar panels. The cleaning device features a high-voltage electrode composed of parallel sharp needles and a grounded frame electrode, positioned a few millimetres above the solar panel surface (Figure I.12). Dust removal is achieved by the ionic wind emerging from a 5 mm-wide opening at the bottom of the device (Figure I.13). The experiments with Algerian Sahara sand dust demonstrated an ionic wind velocity of 2 m/s and an impressive 95% cleaning efficiency, consuming only 20 W of power. This development holds significant potential for enhancing solar panel efficiency in dust-prone environments.

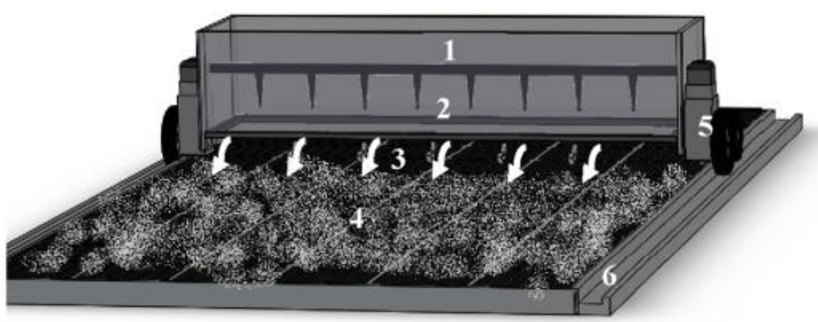

Figure I.12. The actuator mounted on the PV panel 1) HV electrode; 2) Ground electrode; 3) Exit of the ionic wind; 4) Dust; 5) Driven wheel; 6) Guide rail. [103]

These advancements in ionic wind-based cleaning technologies provide a sustainable, water-free alternative to conventional solar panel maintenance, ensuring higher efficiency and prolonged operational lifespan, particularly in dust-heavy regions.

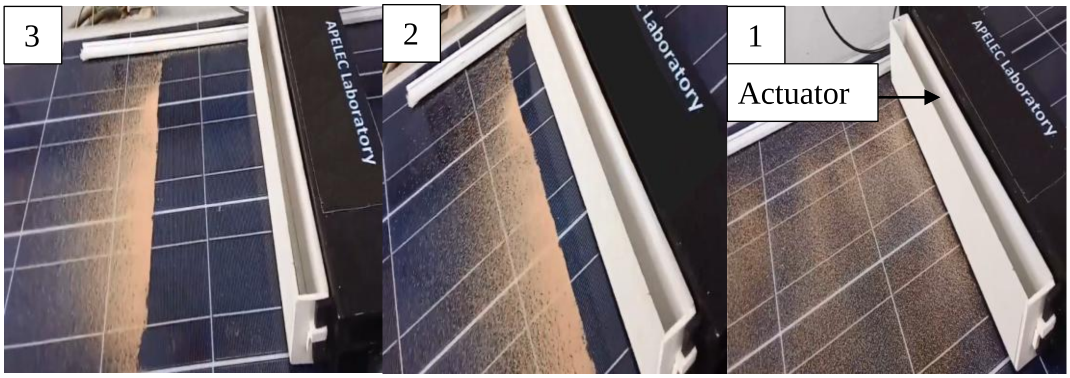

Figure I.13. Photovoltaic panel cleaning.[104]

I.5 Challenges and Research Directions

I.5.1 Energy Efficiency and Optimization

Significant research has been conducted to enhance the energy efficiency and performance of ionic wind generators through electrode configuration optimization and stacking techniques. Despite the remarkable advancements, energy efficiency and optimization present significant challenges when using electric wind generated by an electric discharge in industrial applications. These challenges stem from the complex physics of the discharge process and the need for precise control over energy input to maximize efficiency. Here are the key aspects:

- **Energy Losses in the Discharge Process:**

➢ A large portion of the electrical energy supplied to the system is lost as heat due to resistive heating, ion recombination, and radiative losses (such as ultraviolet and infrared radiation).[105, 106]

➢ The efficiency of converting electrical energy into useful kinetic energy (electric wind) is often low, with only a fraction of the energy being used for air movement.[107]

- **Inefficiencies in Ionization and Charge Transport:**

➢ The process of ionizing air molecules to generate a charged flow requires high voltages, leading to power consumption that is not always proportional to the generated thrust.[108]

➢ Non-uniform electric fields can lead to inefficiencies where some regions experience excessive ionization, while others do not contribute effectively to wind generation.[109]

- **Optimization of Electrode Geometry and Placement:**

➢ The shape, size, and material of electrodes significantly affect the efficiency of electric wind generation. Improper electrode design can lead to unnecessary energy losses, uneven discharge distribution, and increased power consumption.[110]

➢ Optimized electrode spacing and alignment can improve the conversion efficiency by ensuring a more uniform and controlled ionization process.

- **Power Supply and Control System Challenges:**

➢ High-voltage power supplies required for electric discharge systems must be carefully designed to minimize power losses and maintain stable operation.

➢ Real-time feedback and control systems are needed to adjust voltage levels dynamically, ensuring optimal energy use without excessive losses.

- **Heat Dissipation and Thermal Management:**

➢ Inefficient electric wind systems generate excess heat, requiring additional cooling mechanisms, which further increase energy consumption.[111]

I.5.2 Durability of Electrodes and Materials

- **Electrode Erosion**

In electric discharge processes, such as corona discharge or dielectric barrier discharge, electrodes are constantly exposed to high electric fields, ion bombardment, and sometimes thermal effects. Over time, these factors cause material degradation, leading to erosion and reduced electrode efficiency.[112]

- **Oxidation and Corrosion**

Many industrial applications involve humid or reactive gas environments. Electrodes and materials exposed to these conditions undergo oxidation or corrosion, which can alter their surface properties, reduce conductivity, and ultimately affect the efficiency of the electric wind.[109]

- **Thermal Stress and Fatigue**

Discharge-induced heating can lead to thermal expansion and contraction cycles. This repeated thermal stress may cause material fatigue, cracks, or even structural failure, especially in applications that require continuous operation.[113]

- **Material Aging and Surface Modifications**

Continuous exposure to energetic ions, UV radiation, and reactive species in the plasma can alter the electrode surface. This may change its electrical properties, leading to variations in discharge characteristics and reducing system performance.[109]

- **Contamination and Deposits**

Industrial environments often contain dust, aerosols, or chemical vapors. These contaminants can accumulate on electrode surfaces, modifying the discharge behavior and reducing the effectiveness of electric wind generation.[109]

Due to these challenges, selecting durable materials (such as tungsten, stainless steel, or specially coated electrodes) and implementing maintenance strategies (such as periodic cleaning and replacement) are critical for maintaining the reliability of electric wind-based systems.

I.5.3 Scaling up for Industrial Applications

The ionic wind technology is based on corona discharge under atmospheric pressure, the inherent properties of which present many challenges for transitioning ionic wind technologies to the market. For example, aside from the additional voltage boosters, the extremely high voltage also causes safety problems. The ozone produced during corona discharge can pose serious health risks to humans. Changes in ambient temperature and humidity alter the flow field of the ionic wind, causing it to deviate from the designed conditions. Moreover, when the ionic wind pump operates for a long time, there are still problems of durability, dust accumulation, and corrosion on the electrode surface. All these issues must be studied thoroughly and considered in the design of IWGs (Ionic Gind Generators) for specific applications.

- **Extremely High Voltage**

Conventionally, the formation of ionic wind requires a very high electric field strength to trigger the corona discharge in the vicinity of the emitting electrode, which is obtained by applying a high voltage between two metal electrodes. High voltages are prohibitive for some applications, such as portable electronics, because of safety, size, and weight constraints. In some applications, the upper limit of the applied voltage is also specified. Therefore, reducing the operating voltage of IWGs as much as possible is a requirement for their application. A simple and effective way of reducing the operating voltage of IWGs is to decrease the gap between the anode and cathode; however, this also decreases the range of operating voltage and significantly changes the designed performance of the IWG. Therefore, this method is not commonly adopted.

At present, an approach that can reduce the corona onset voltage without significantly changing the performance of the IWG through an ingenious electrode configuration. For example, Johnson and Tirumala *et al* [114, 115] used additional downstream electrodes from the primary collector to extend the discharge and form a direct current (DC) 'assisted discharge' (Figure I.14).

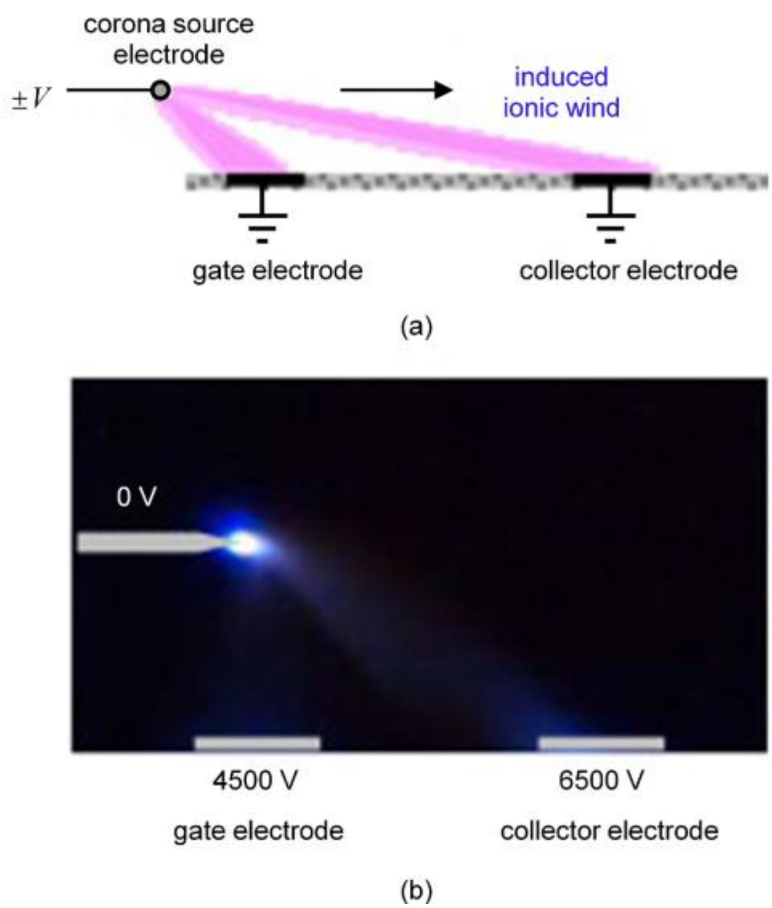

Figure I.14. DC assisted corona discharge. (a) Schematic of two distinct collecting electrodes (primary and secondary). (b) Photograph of discharge operated in negative DC mode. Reproduced from [115]

Compared with reducing the operating voltage of the IWG through an ingenious electrode configuration, emitting electrode decoration by using nanomaterials has attracted more attention. The basic principle of this method is to construct nanoscale 'emitting electrodes' by forming a large number of nanoscale protrusions on the electrode surface. As nanomaterials have large specific surface areas, high electrical conductivities, and very small tip curvatures, a strong electric field is produced around them, for example, graphene deposited on the surface of a metal electrode, as displayed in Figure I.15. The corona onset voltage is proportional to the irregularity factor (the ratio of the local electric field E_{loc} at the surface of a smooth conductor to the maximum E_{loc} of a roughened conductor [116]) and radius of curvature of the electrode surface. Therefore, both the two parameters of the electrode decorated with nanomaterials decrease (the surface is further roughened, and the radius of curvature on the electrode surface decreases from macro and micro to nanoscale owing to the presence of nanoparticles). This causes the nanoscale 'electrodes' to discharge at extremely low voltages, forming nanoscale plasma and ionic wind (Figure I.16).

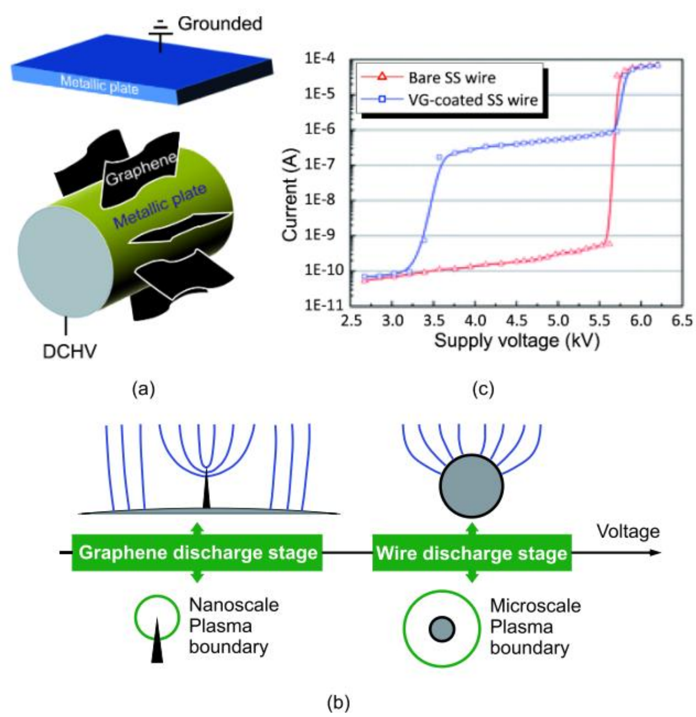

Figure I.15. Schematics of nanomaterial-enhanced discharges for reducing the corona onset voltage. (a) Simplified configuration of vertical graphene (VG)-coated wire discharge. (b) Electric field lines and plasma region for the discharge at 'graphene discharge stage' and 'wire discharge stage'. (c) I–V curves of corona discharges employing bare stainless steel (SS) wire and VG-coated SS wire for discharge of negative polarity. Different from the bare SS wire, the VG-coated SS wire can proceed to the 'graphene discharge stage' at low applied voltages. Reproduced from [117]

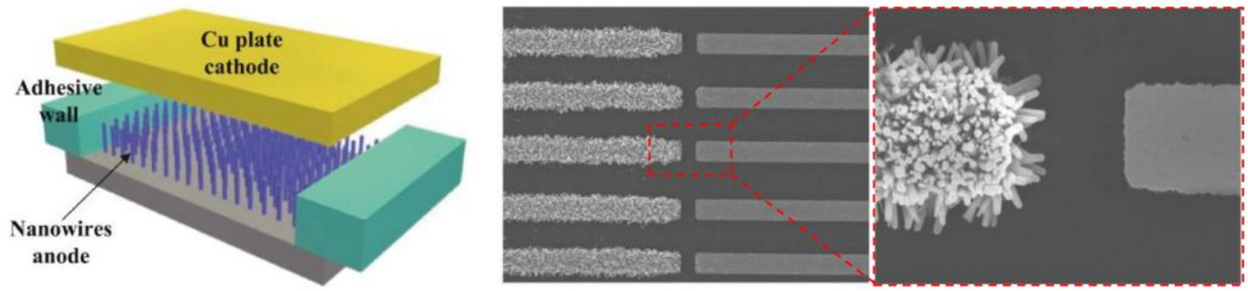

(a) (b)

Figure I.16. ZnO nanowire-based corona discharge devices. [118]

The basic principle of using nanomaterials to change the corona discharge characteristics and ionic wind velocity is to increase the discharge intensity by adding a large number of local micro-discharge sites on the electrode surface.

- **Ozone Generation**

Ozone and nitrogen oxides (NOx) are byproducts of ionic wind generation, with ozone being the primary concern due to its environmental and health implications. Ozone formation occurs in two main steps: the dissociation of oxygen molecules into atoms through electron impact, followed by the recombination of oxygen atoms with oxygen molecules to form ozone. Various secondary reactions involving nitrogen species also influence ozone production in dry air [119-121]. The generated ozone can be decomposed through interactions with free oxygen atoms, reducing its overall concentration. Additionally, when NOx levels reach a certain threshold, ozone formation is suppressed due to competing chemical reactions [119].

Ozone possesses strong oxidative properties, making it valuable for applications such as bacterial inactivation [122], food preservation [123], disinfection [124], and wastewater treatment [125]. However, excessive ozone exposure can harm the human respiratory system, degrade materials, and accelerate the aging of electrical insulation. Regulatory agencies, including the U.S. Environmental Protection Agency (EPA) and the World Health Organization, have set limits on ground-level ozone concentrations to mitigate health risks [117], [126]. Given these concerns, ozone emissions from ionic wind generators (IWGs) must be minimized to meet safety standards and prevent adverse effects on both humans and nearby materials.

The amount of ozone generated is influenced by several factors, including plasma chemistry, electron density, energy levels, and plasma volume [116], [117]. Increasing the temperature of the corona discharge zone can suppress ozone formation by altering the reaction rates, and some studies have shown that heating the corona electrode can reduce ozone emissions by up to 85% [127], [128]. However, this method also increases power consumption, making it impractical for many IWG applications.

From a microscopic perspective, reducing the size of the corona electrode has been shown to lower ozone emissions without significantly enhancing ozone production due to increased electron kinetic energy [129]. This principle applies to both positive and negative coronas. To further control ozone emissions, researchers have explored nanotechnology-based solutions, such as decorating electrodes with nanomaterials. For example, Wang et al. [130] demonstrated that carbon nanotube (CNT)-decorated electrodes combined with MnO_2 and activated carbon coatings reduced ozone concentrations by over 90%, while also improving energy conversion efficiency [116] (Figure I.17).

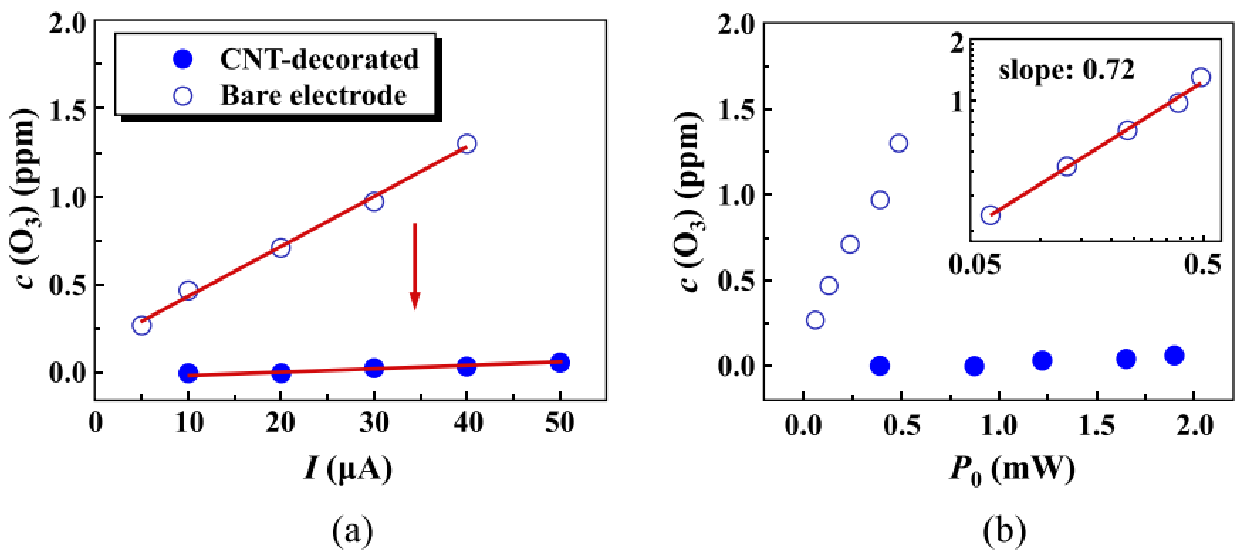

Figure I.17. Comparison of ozone concentrations of a CNT-decorated and bare electrode as a function of (a) corona current and (b) power output. Reprinted from [116]

- **Influence of Ambient Humidity and Temperature**

The performance of ionic wind generators (IWGs) is significantly influenced by environmental factors such as temperature and humidity, affecting parameters including corona onset and breakdown voltages, current–voltage characteristics, output wind velocity, electrode-material degradation, and ozone emission. These variations must be considered during the design phase to ensure optimal operation in different climates and geographic locations, Lee et al. [131].

Temperature also impacts corona discharge and IWG performance[132]. When increasing temperature both onset and breakdown voltages decrease. The underlying mechanism is attributed to increased ion mobility due to lower gas density and an extended mean free path for gas molecules [132]. Furthermore, high temperatures can induce additional corona currents through gas ionization, free-electron detachment, and thermionic emission from the cathode surface. However, these effects are only significant above 773 K, with gas density changes being the primary factor influencing corona discharge at lower temperatures.

Humidity affects corona discharge primarily through the formation of molecular clusters with low ion mobility. In positive coronas, water molecules interact with ions, forming hydrated positive charge carriers such as $H^+(H_2O)_n$ and $NO^+(H_2O)_n$ [25]. In negative coronas, similar hydration effects occur, leading to the formation of negative hydrated ions such as $O^-(H_2O)_n$.

For positive corona, higher humidity decreases pulse amplitude but increases repetition frequency. Conversely, in negative coronas, pulse amplitude increases while repetition frequency decreases. In both cases, the average discharge current declines with increasing humidity [77]. The reduction in positive corona intensity is attributed to ion accumulation, whereas the higher pulse amplitude in negative coronas is linked to an increase in the effective ionization integral. Humidity also influences voltage–current characteristics as indicated in [76].

I.6 Conclusion

The unique features of ionic wind make it promising for extensive applications. In this chapter, the detailed principle of ionic wind generation is presented. It can be concluded from these existing studies that the ionic wind technology continues to be an active research field that has attracted the attention of both scholars and engineers worldwide. Many creative studies have been carried out to advance this field, both in fundamental research and application-driven investigations. The commercialization of ionic wind still requires a large amount of time and effort. In particular, understanding the underlying mechanisms of some physical phenomena that hinder its use is still not comprehensive and intensive. Breakthroughs in theoretical research and numerical methods, as well as further development of new materials and new techniques for electrode surface treatment, are necessary. Only when these obstacles are effectively resolved can the widespread application of ionic wind in the industry be truly realized.

Reference

[1] I. Y. Chen, M.-Z. Guo, K.-S. Yang, and C.-C. Wang, "Enhanced cooling for LED lighting using ionic wind," *International Journal of Heat and Mass Transfer*, vol. 57, no. 1, pp. 285–291, Jan. 2013, doi: 10.1016/j.ijheatmasstransfer.2012.10.015.

[2] I. Y. Chen, C.-J. Chen, and C.-C. Wang, "Influence of electrode configuration on the heat transfer performance of a LED heat source," *International Journal of Heat and Mass Transfer*, vol. 77, pp. 795–801, Oct. 2014, doi: 10.1016/j.ijheatmasstransfer.2014.06.023.

[3] J. Wang, T. Zhu, Y. Cai, J. Zhang, and J. Wang, "Review on the recent development of corona wind and its application in heat transfer enhancement," *International Journal of Heat and Mass Transfer*, vol. 152, p. 119545, May 2020, doi: 10.1016/j.ijheatmasstransfer.2020.119545.

[4] M. Abdel-Salam, A. Hashem, A. Yehia, A. Mizuno, A. Turky, and A. Gabr, "Characteristics of corona and silent discharges as influenced by geometry of the discharge reactor," *J. Phys. D: Appl. Phys.*, vol. 36, no. 3, p. 252, Jan. 2003, doi: 10.1088/0022-3727/36/3/306.

[5] J. Qu, D. Zhang, J. Zhang, and W. Tao, "LED chip cooling system using ionic wind induced by multi-wire corona discharge," *Applied Thermal Engineering*, vol. 193, p. 116946, Jul. 2021, doi: 10.1016/j.applthermaleng.2021.116946.

[6] C. Xu *et al.*, "Enhanced Cooling of LED Filament Bulbs Using an Embedded Tri-Needle/Ring Ionic Wind Device," *Energies*, vol. 13, no. 11, Art. no. 11, Jan. 2020, doi: 10.3390/en13113008.

[7] Y. Zhang, L. Liu, Y. Chen, and J. Ouyang, "Characteristics of ionic wind in needle-to-ring corona discharge," *Journal of Electrostatics*, vol. 74, pp. 15–20, Apr. 2015, doi: 10.1016/j.elstat.2014.12.008.

[8] K. Iranshahi, A. Martynenko, and T. Defraeye, "Cutting-down the energy consumption of electrohydrodynamic drying by optimizing mesh collector electrode," *Energy*, vol. 208, p. 118168, Oct. 2020, doi: 10.1016/j.energy.2020.118168.

[9] S. J. Lee, L. Li, K. Kwon, W. Kim, and D. Kim, "Parallel integration of ionic wind generators on PCBs for enhancing flow rate," *Microsyst Technol*, vol. 21, no. 7, pp. 1465–1471, Jul. 2015, doi: 10.1007/s00542-014-2320-7.

[10] D. B. Go, S. V. Garimella, T. S. Fisher, and R. K. Mongia, "Ionic winds for locally enhanced cooling," *Journal of Applied Physics*, vol. 102, no. 5, p. 053302, Sep. 2007, doi: 10.1063/1.2776164.

[11] J. Wang, R. Fu, and X. Hu, "Experimental study on EHD heat transfer enhancement with a wire electrode between two divergent fins," *Applied Thermal Engineering*, vol. 148, pp. 457–465, Feb. 2019, doi: 10.1016/j.applthermaleng.2018.11.058.

[12] N. Zehtabiyan-Rezaie, M. Saffar-Avval, and K. Adamiak, "Forced convection heat transfer enhancement using a coaxial wire-tube corona system," *Journal of Electrostatics*, vol. 103, p. 103415, Jan. 2020, doi: 10.1016/j.elstat.2019.103415.

[13] A. Świerczok and M. Jędrusik, "The collection efficiency of ESP model - Comparison of experimental results and calculations using Deutsch model," *Journal of Electrostatics*, vol. 91, pp. 41–47, Feb. 2018, doi: 10.1016/j.elstat.2017.12.004.

[14] Y. Wang *et al.*, "Insights into the role of ionic wind in honeycomb electrostatic precipitators," *Journal of Aerosol Science*, vol. 133, pp. 83–95, Jul. 2019, doi: 10.1016/j.jaerosci.2019.04.011.

[15] T. Defraeye and A. Martynenko, "Electrohydrodynamic drying of multiple food products: Evaluating the potential of emitter-collector electrode configurations for upscaling," *Journal of Food Engineering*, vol. 240, pp. 38–42, Jan. 2019, doi: 10.1016/j.jfoodeng.2018.07.011.

[16] T. Defraeye and A. Martynenko, "Electrohydrodynamic drying of food: New insights from conjugate modeling," *Journal of Cleaner Production*, vol. 198, pp. 269–284, Oct. 2018, doi: 10.1016/j.jclepro.2018.06.250.

[17] X. Yan and Y. Jiang, "Numerical evaluation of thefog collection potential of electrostatically enhanced fog collector," *Atmospheric Research*, vol. 248, p. 105251, Jan. 2021, doi: 10.1016/j.atmosres.2020.105251.

[18] J.-S. Leu, J.-Y. Jang, and Y.-H. Wu, "Optimization of the wire electrode height and pitch for 3-D electrohydrodynamic enhanced water evaporation," *International Journal of Heat and Mass Transfer*, vol. 118, pp. 976–988, Mar. 2018, doi: 10.1016/j.ijheatmasstransfer.2017.11.056.

[19] E. Moreau, "Airflow control by non-thermal plasma actuators," *J. Phys. D: Appl. Phys.*, vol. 40, no. 3, p. 605, Jan. 2007, doi: 10.1088/0022-3727/40/3/S01.

[20] W. Wang *et al.*, "Regulation-controlling of boundary layer by multi-wire-to-cylinder negative corona discharge," *Applied Thermal Engineering*, vol. 119, pp. 438–448, Jun. 2017, doi: 10.1016/j.applthermaleng.2017.03.092.

[21] H. Xu *et al.*, "Flight of an aeroplane with solid-state propulsion," *Nature*, vol. 563, no. 7732, pp. 532–535, Nov. 2018, doi: 10.1038/s41586-018-0707-9.

[22] S. Chen, Y. Zhu, J. Tu, and F. Wang, "Numerical investigation of an electroaerodynamic driven aeroplane: electrical properties, ionic wind and flight performance," *J. Phys. D: Appl. Phys.*, vol. 52, no. 36, p. 365203, Jul. 2019, doi: 10.1088/1361-6463/ab2b2a.

[23] N. Cabeo, *Philosophia magnetica*. Apud F. Succium, 1629.

[24] M. Robinson, "A History of the Electric Wind," *American Journal of Physics*, vol. 30, no. 5, pp. 366–372, May 1962, doi: 10.1119/1.1942021.

[25] B. Zhang, J. He, and Y. Ji, "Prediction of average mobility of ions from corona discharge in air with respect to pressure, humidity and temperature," *IEEE Transactions on Dielectrics and Electrical Insulation*, vol. 26, no. 5, pp. 1403–1410, Oct. 2019, doi: 10.1109/TDEI.2019.008001.

[26] L. Zhao and K. Adamiak, "Numerical simulation of the effect of EHD flow on corona discharge in compressed air," in *2011 IEEE Industry Applications Society Annual Meeting*, Oct. 2011, pp. 1–7. doi: 10.1109/IAS.2011.6074283.

[27] B. XingMing *et al.*, "The role of low air pressure in the variation of negative corona-generated space charge in a rod to plane electrode," *High Voltage*, vol. 3, no. 2, pp. 126–132, 2018, doi: 10.1049/hve.2017.0108.

[28] S. Chen, K. Li, F. Wang, Q. Sun, and L. Zhong, "Effect of humidity and air pressure on the discharge modes transition characteristics of negative DC corona," *IET Science, Measurement & Technology*, vol. 13, no. 8, pp. 1212–1218, 2019, doi: 10.1049/iet-smt.2019.0032.

[29] H. Y. Sun, B. X. Lu, M. Wang, Q. F. Guo, and Q. K. Feng, "The role of photoionization in negative corona discharge: The influences of temperature, humidity, and air pressure on a corona," *Physics of Plasmas*, vol. 24, no. 10, p. 103506, Sep. 2017, doi: 10.1063/1.4990480.

[30] Q. Hu, L. Shu, X. Jiang, C. Sun, Z. Qiu, and R. Lin, "Influence of air pressure and humidity on positive direct current corona discharge performances of the conductor in a corona cage," *International Transactions on Electrical Energy Systems*, vol. 24, no. 5, pp. 723–735, 2014, doi: 10.1002/etep.1732.

[31] N. H. de V. H. B.Sc.Ph.D, "Guericke's sulphur globe," *Annals of Science*, Mar. 1950, doi: 10.1080/00033795000201981.

[32] F. Hauksbee, *Physico-mechanical experiments*. in Newtonianism in eighteenth-century Britain. Thoemmes Continuum, 2004. Accessed: Feb. 20, 2025. [Online]. Available: https://cir.nii.ac.jp/crid/1130282268698739328

[33] I. Newton, *Opticks; or, A treatise of the reflections, inflections and colours of light*. London : Printed for W. and J. Innys, Printers to the royal Society, at the prince's-Arms in St. Paul's Church-Yard, 1718. Accessed: Nov. 25, 2024. [Online]. Available: http://archive.org/details/opticksortreatis1718newt

[34] T. Cavallo, *A complete treatise of electricity*. 1795.

[35] M. Faraday, *Experimental researches in electricity*. London, R. and J. E. Taylor, 1839. Accessed: Nov. 25, 2024. [Online]. Available: http://archive.org/details/experimentalres04faragoog

[36] J. C. Maxwell, *A treatise on electricity and magnetism*. Oxford : Clarendon Press, 1873. Accessed: Nov. 25, 2024. [Online]. Available: http://archive.org/details/electricandmagne01maxwrich

[37] A. P. Chattock, "XLIV. On the velocity and mass of the ions in the electric wind in air," *The London Edinburgh and Dublin Philosophical Magazine and Journal of Science*, vol. 48, no. 294, 1899, doi: 10.1080/14786449908621431.

[38] E. Lob, "Archiv Der Elektrischen Uebertragung," *Baden-Württemberg, Germany: Stuttgart*, 1954.

[39] D. J. Harney, "An Aerodynamic Study of the 'Electric Wind,'" engd, California Institute of Technology, 1957. doi: 10.7907/Z774-ZM53.

[40] M. Robinson, "Movement of air in the electric wind of the corona discharge," *Transactions of the American Institute of Electrical Engineers, Part I: Communication and Electronics*, vol. 80, no. 2, pp. 143–150, May 1961, doi: 10.1109/TCE.1961.6373091.

[41] O. M. Stuetzer, "Magnetohydrodynamics and Electrohydrodynamics," *Physics of Fluids*, vol. 5, pp. 534–544, May 1962, doi: 10.1063/1.1706654.

[42] *Gas Discharge Physics*. Accessed: Feb. 21, 2025. [Online]. Available: https://link.springer.com/book/9783642647604

[43] J.-S. Chang, P. A. Lawless, and T. Yamamoto, "Corona discharge processes," *IEEE Transactions on Plasma Science*, vol. 19, no. 6, pp. 1152–1166, Dec. 1991, doi: 10.1109/27.125038.

[44] P. Bruggeman and R. Brandenburg, "Atmospheric pressure discharge filaments and microplasmas: physics, chemistry and diagnostics," *J. Phys. D: Appl. Phys.*, vol. 46, no. 46, p. 464001, Oct. 2013, doi: 10.1088/0022-3727/46/46/464001.

[45] U. Kogelschatz, Y. S. Akishev, and A. P. Napartovich, "History of non-equilibrium air discharges," *Non-equilibrium air plasmas at atmospheric pressure*, pp. 17–60, 2005.

[46] A. Schutze, J. Y. Jeong, S. E. Babayan, J. Park, G. S. Selwyn, and R. F. Hicks, "The atmospheric-pressure plasma jet: a review and comparison to other plasma sources," *IEEE Transactions on Plasma Science*, vol. 26, no. 6, pp. 1685–1694, Dec. 1998, doi: 10.1109/27.747887.

[47] R. Brandenburg, "Dielectric barrier discharges: progress on plasma sources and on the understanding of regimes and single filaments," *Plasma Sources Sci. Technol.*, vol. 26, no. 5, p. 053001, Apr. 2017, doi: 10.1088/1361-6595/aa6426.

[48] U. Kogelschatz, "Dielectric-Barrier Discharges: Their History, Discharge Physics, and Industrial Applications," *Plasma Chemistry and Plasma Processing*, vol. 23, no. 1, pp. 1–46, Mar. 2003, doi: 10.1023/A:1022470901385.

[49] B. Eliasson and U. Kogelschatz, "Modeling and applications of silent discharge plasmas," *IEEE Transactions on Plasma Science*, vol. 19, no. 2, pp. 309–323, Apr. 1991, doi: 10.1109/27.106829.

[50] W. Kim, H. Do, M. G. Mungal, and M. A. Cappelli, "On the role of oxygen in dielectric barrier discharge actuation of aerodynamic flows," *Applied Physics Letters*, vol. 91, no. 18, p. 181501, Oct. 2007, doi: 10.1063/1.2803755.

[51] G. I. Font, C. L. Enloe, J. Y. Newcomb, A. L. Teague, A. R. Vasso, and T. E. McLaughlin, "Effects of Oxygen Content on Dielectric Behavior Barrier Discharge Plasma Actuator Behavior," *AIAA Journal*, vol. 49, no. 7, pp. 1366–1373, 2011, doi: 10.2514/1.J050450.

[52] K. Hassouni, F. F. Massines, and J.-M. Pouvesle, "Plasmas hors-équilibre à des pressions atmosphériques," in *Plasmas froids. Génération, caractérisation et technologies*, F. Massines, Ed., in Intégrations [des savoirs et savoir-faire], no. 3. , PUSE-MRCT-CNRS, 2004, pp. 49–108. Accessed: Feb. 21, 2025. [Online]. Available: https://hal.science/hal-01481541

[53] A. Fridman, A. Fridman, L. A. Kennedy, and L. A. Kennedy, *Plasma Physics and Engineering*. Boca Raton: CRC Press, 2004. doi: 10.1201/9781482293630.

[54] D. Xiao, *Gas Discharge and Gas Insulation*, vol. 6. in Energy and Environment Research in China, vol. 6. Berlin, Heidelberg: Springer Berlin Heidelberg, 2016. doi: 10.1007/978-3-662-48041-0.

[55] *Plasma Engineering*. 2018. Accessed: Feb. 21, 2025. [Online]. Available: https://shop.elsevier.com/books/plasma-engineering/keidar/978-0-12-813702-4

[56] "Atmospheric electricity. By B. F. J. Schonland. London (Methuen), 2nd Edition, 1953. Pp. vii, 95; 20 Figs, 8 tables. 7s. 6d," *Quarterly Journal of the Royal Meteorological Society*, vol. 80, no. 343, pp. 122–123, 1954, doi: 10.1002/qj.49708034336.

[57] G. Berger, E. Marode, O. Belabed, B. Senouci, I. Gallimberti, and A. Osgualdo, "Effect of water vapour on the discharge regimes and the deviations from similarity law in compressed SF6 for positive polarity," *J. Phys. D: Appl. Phys.*, vol. 24, no. 9, p. 1551, Sep. 1991, doi: 10.1088/0022-3727/24/9/006.

[58] B. Senouci, "Influence des impuretes sur la formation et le mode de la decharge dans le sf : :(6) comprime en polarite positive," These de doctorat, Paris 6, 1987. Accessed: Feb. 21, 2025. [Online]. Available: https://theses.fr/1987PA066623

[59] D. G. Boyers and W. A. Tiller, "Corona discharge photography," *Journal of Applied Physics*, vol. 44, no. 7, pp. 3102–3112, Jul. 1973, doi: 10.1063/1.1662715.

[60] L. Colli and U. Facchini, "Secondary Electron Emission by Photoelectric Action and Ion Bombardment at the Cathode in Corona Breakdown of Argon," *Phys. Rev.*, vol. 96, no. 1, pp. 1–4, Oct. 1954, doi: 10.1103/PhysRev.96.1.

[61] A. Fridman, *Plasma Chemistry*. Cambridge University Press, 2008.

[62] L. B. Loeb and J. M. Meek, *The mechanism of the electric spark*. Stanford University Press, 1941.

[63] E. M. Bazelyan and N. L. Aleksandrov, "Electric Field in a Positive Streamer in Long Air Gaps," *Plasma Phys. Rep.*, vol. 48, no. 7, pp. 789–797, Jul. 2022, doi: 10.1134/S1063780X22700222.

[64] M. L. Coulibaly, "Caractérisation des décharges électriques se propageant aux interfaces gaz/solide – Relation entre propriétés des matériaux et dimension fractale," phdthesis, Ecole Centrale de Lyon, 2009. Accessed: Feb. 21, 2025. [Online]. Available: https://theses.hal.science/tel-00419967

[65] Y. P. Raizer and J. E. Allen, *Gas discharge physics*, vol. 2. Springer, 1997. Accessed: Feb. 21, 2025. [Online]. Available: https://link.springer.com/gp/book/9783642647604

[66] E. Karakas, A. Begum, and M. Laroussi, "A Positive Corona-Based Ion Wind Generator," *IEEE Transactions on Plasma Science*, vol. 36, no. 4, pp. 950–951, Aug. 2008, doi: 10.1109/TPS.2008.924401.

[67] T. Zhang, Y. Zhang, Q. Ji, B. Li, and J. Ouyang, "Characteristics and underlying physics of ionic wind in dc corona discharge under different polarities*," *Chinese Phys. B*, vol. 28, no. 7, p. 075202, Jul. 2019, doi: 10.1088/1674-1056/28/7/075202.

[68] J. F. Loiseau, J. Batina, F. Noël, and R. Peyrous, "Hydrodynamical simulation of the electric wind generated by successive streamers in a point-to-plane reactor," *J. Phys. D: Appl. Phys.*, vol. 35, no. 10, p. 1020, Apr. 2002, doi: 10.1088/0022-3727/35/10/310.

[69] M. Goldman and R. S. Sigmond, "Corona and Insulation," *IEEE Transactions on Electrical Insulation*, vol. EI-17, no. 2, pp. 90–105, Apr. 1982, doi: 10.1109/TEI.1982.298543.

[70] E. Moreau and E. Defoort, "Effect of the high voltage waveform on the ionic wind produced by a needle-to-plate dielectric barrier discharge," *Scientific Reports*, vol. 12, no. 1, p. 18699, 2022.

[71] L. B. Loeb, *Electrical coronas: their basic physical mechanisms*. Univ of California Press, 2023. Accessed: Feb. 21, 2025. [Online]. Available: https://books.google.com/books?hl=en&lr=&id=NWLhEAAAQBAJ&oi=fnd&pg=PA1&dq=Loeb,+L.+B.+Electrical+Coronas:+Their+Basic+Physical+Mechanisms+(Berkeley:+University+of+California+Press,+1965).&ots=VA7sgWMvu0&sig=LP8iCaHNrDsfImuIuEQwwjVLz1w

[72] S. Sato, H. Furukawa, A. Komuro, M. Takahashi, and N. Ohnishi, "Successively accelerated ionic wind with integrated dielectric-barrier-discharge plasma actuator for low-voltage operation," *Scientific reports*, vol. 9, no. 1, p. 5813, 2019.

[73] R. S. Sigmond and M. Goldman, “Corona Discharge Physics and Applications,” in *Electrical Breakdown and Discharges in Gases*, E. E. Kunhardt and L. H. Luessen, Eds., Boston, MA: Springer US, 1983, pp. 1–64. doi: 10.1007/978-1-4615-9311-9_1.

[74] M. Hering, J. Speck, S. Großmann, and U. Riechert, “Influence of gas temperature on the breakdown voltage in gas-insulated systems,” *IEEE Transactions on Dielectrics and Electrical Insulation*, vol. 24, no. 1, pp. 401–408, Feb. 2017, doi: 10.1109/TDEI.2016.006099.

[75] S. R. Mahmoudi, K. Adamiak, P. Castle, and M. Ashjaee, “The effect of corona discharge on free convection heat transfer from a horizontal cylinder,” *Experimental Thermal and Fluid Science*, vol. 34, no. 5, pp. 528–537, Jul. 2010, doi: 10.1016/j.expthermflusci.2009.11.006.

[76] X. Wang and C. You, “Effect of humidity on negative corona discharge of electrostatic precipitators,” *IEEE Transactions on Dielectrics and Electrical Insulation*, vol. 20, no. 5, pp. 1720–1726, 2013.

[77] P. Xu, B. Zhang, S. Chen, and J. He, “Influence of humidity on the characteristics of positive corona discharge in air,” *Physics of Plasmas*, vol. 23, no. 6, 2016, Accessed: Feb. 23, 2025. [Online]. Available: https://pubs.aip.org/aip/pop/article/23/6/063511/319946

[78] M. J. Zeng, Z. G. Qu, and J. F. Zhang, “Negative corona discharge and flow characteristics of a two-stage needle-to-ring configuration ionic wind pump for temperature and relative humidity,” *International Journal of Heat and Mass Transfer*, vol. 201, p. 123561, 2023.

[79] L. Fouad and S. Elhazek, “Effect of humidity on positive corona discharge in a three electrode system,” *Journal of Electrostatics*, vol. 35, no. 1, pp. 21–30, 1995.

[80] M. Tabrizchi and F. Rouholahnejad, “Corona discharge ion mobility spectrometry at reduced pressures,” *Review of scientific instruments*, vol. 75, no. 11, pp. 4656–4661, 2004.

[81] J.-R. Riba, P. Bas-Calopa, and M. Moreno-Eguilaz, “Analysing the influence of geometry and pressure on corona discharges,” *European journal of physics*, vol. 43, no. 5, p. 055201, 2022.

[82] H. Li, C. Guo, Y. Li, X. Hong, J. Zhu, and Z. Chen, “Effects of atmospheric-pressure discharge type on ionic wind velocity for needle-to-cylinder electrode,” *Journal of Vacuum Science & Technology A*, vol. 34, no. 3, 2016, Accessed: Mar. 18, 2025. [Online]. Available: https://pubs.aip.org/avs/jva/article/34/3/031308/595681

[83] L. Li, J. Li, Z. Zhao, and C. Li, “Effect of pressure on repetitive performance of a corona-stabilized plasma closing switch,” *Physics of Plasmas*, vol. 27, no. 2, 2020, Accessed: Mar. 18, 2025. [Online]. Available: https://pubs.aip.org/aip/pop/article/27/2/023508/1062752

[84] M. Kaci, H. Ait Said, A. Laifaoui, M. Aissou, H. Nouri, and Y. Zebboudj, “Investigation on the Corona Discharge in Blade-to-Plane Electrode Configuration,” *Braz J Phys*, vol. 45, no. 6, pp. 643–655, Dec. 2015, doi: 10.1007/s13538-015-0357-4.

[85] F. de A. Lima, G. B. Medeiros, P. A. M. Chagas, M. L. Aguiar, and V. G. Guerra, “Aerosol nanoparticle control by electrostatic precipitation and filtration processes—A review,” *Powders*, vol. 2, no. 2, pp. 259–298, 2023.

[86] Q. Tang, M. Liu, J. Zhang, C. Wang, and X. Cui, “Ionic wind tweezer based on multi-needle corona discharge for programmable droplet manipulation,” *Sensors and Actuators B: Chemical*, vol. 413, p. 135796, Aug. 2024, doi: 10.1016/j.snb.2024.135796.

[87] Y. Morabit, M. I. Hasan, R. D. Whalley, E. Robert, M. Modic, and J. L. Walsh, “A review of the gas and liquid phase interactions in low-temperature plasma jets used for biomedical applications,” *Eur. Phys. J. D*, vol. 75, no. 1, p. 32, Jan. 2021, doi: 10.1140/epjd/s10053-020-00004-4.

[88] S. Zhou, G. Li, H. Zheng, and S. Liu, “A New Method for 3D Microstructure Fabrication via Ionic Wind,” in *2017 IEEE 67th Electronic Components and Technology Conference (ECTC)*, May 2017, pp. 1823–1828. doi: 10.1109/ECTC.2017.44.

[89] A. G. Bailey, “The science and technology of electrostatic powder spraying, transport and coating,” *Journal of electrostatics*, vol. 45, no. 2, pp. 85–120, 1998.

[90] X. Meng, H. Zhang, and J. J. Zhu, “The characteristics of particle charging and deposition during powder coating processes with coarse powder,” *Journal of Physics D: Applied Physics*, vol. 41, no. 19, p. 195207, 2008.

[91] “MIT proof-of-concept demo of ionic wind propulsion for aircraft,” Green Car Congress. Accessed: Feb. 22, 2025. [Online]. Available: https://www.greencarcongress.com/2018/11/20181122-mitead.html

[92] “MIT engineers fly first-ever plane with no moving parts,” MIT News | Massachusetts Institute of Technology. Accessed: Feb. 22, 2025. [Online]. Available: https://news.mit.edu/2018/first-ionic-wind-plane-no-moving-parts-1121

[93] “RoboBees: Autonomous Flying Microrobots,” Wyss Institute. Accessed: Feb. 22, 2025. [Online]. Available: https://wyss.harvard.edu/technology/robobees-autonomous-flying-microrobots/

[94] G. V. Raghavan, T. J. Rennie, P. S. Sunjka, V. Orsat, W. Phaphuangwittayakul, and P. Terdtoon, “Overview of new techniques for drying biological materials with emphasis on energy aspects,” *Brazilian Journal of Chemical Engineering*, vol. 22, pp. 195–201, 2005.

[95] L.-T. Li, J.-F. Sun, and E. Tatsumi, “Effect of electrohydrodynamic (EHD) technique on drying process and appearance of okara cake,” *Journal of Food Engineering*, vol. 77, no. 2, pp. 275–280, 2006.

[96] J. A. Moses, T. Norton, K. Alagusundaram, and B. K. Tiwari, “Novel Drying Techniques for the Food Industry,” *Food Eng Rev*, vol. 6, no. 3, pp. 43–55, Sep. 2014, doi: 10.1007/s12393-014-9078-7.

[97] Y. Asakawa, “Promotion and retardation of heat transfer by electric fields,” *Nature*, vol. 261, no. 5557, pp. 220–221, 1976.

[98] F. X. Hart and Ch. H. Bachman, “The effect of air ions on liquid evaporation rates,” *Int J Biometeorol*, vol. 12, no. 3, pp. 251–261, Jul. 1968, doi: 10.1007/BF01553425.

[99] A. Martynenko and T. Kudra, “Electrically-induced transport phenomena in EHD drying – A review,” *Trends in Food Science & Technology*, vol. 54, pp. 63–73, Aug. 2016, doi: 10.1016/j.tifs.2016.05.019.

[100] T. R. Bajgai, G. S. V. Raghavan, F. Hashinaga, and M. O. Ngadi, “Electrohydrodynamic Drying—A Concise Overview,” *Drying Technology*, vol. 24, no. 7, pp. 905–910, Aug. 2006, doi: 10.1080/07373930600734091.

[101] F. C. Lai and K.-W. Lai, “EHD-ENHANCED DRYING WITH WIRE ELECTRODE,” *Drying Technology*, vol. 20, no. 7, pp. 1393–1405, Jul. 2002, doi: 10.1081/DRT-120005858.

[102] S. Taghian Dinani and M. Havet, “The influence of voltage and air flow velocity of combined convective-electrohydrodynamic drying system on the kinetics and energy consumption of mushroom slices,” *Journal of Cleaner Production*, vol. 95, pp. 203–211, May 2015, doi: 10.1016/j.jclepro.2015.02.033.

[103] A. Tilmatine, N. Kadous, K. Yanallah, Y. Bellebna, Z. Bendaoudi, and A. Zouaghi, “Experimental investigation of a new solar panels cleaning system using ionic wind produced by corona discharge,” *Journal of Electrostatics*, vol. 124, p. 103827, Jul. 2023, doi: 10.1016/j.elstat.2023.103827.

[104] Z. Bendaoudi *et al.*, “A novel ionic wind actuator for cleaning of photovoltaic panels,” in *2024 IEEE Industry Applications Society Annual Meeting (IAS)*, 2024. Accessed: Feb. 22, 2025. [Online]. Available: https://hal.science/hal-04923535/

[105] J.-S. Chang, P. A. Lawless, and T. Yamamoto, “Corona discharge processes,” *IEEE Transactions on Plasma Science*, vol. 19, no. 6, pp. 1152–1166, Dec. 1991, doi: 10.1109/27.125038.

[106] R. Bartnikas and G. L. d’Ombrain, “A Study of Corona Discharge Rate and Energy Loss in Spark Gaps,” *IEEE Transactions on Power Apparatus and Systems*, vol. 84, no. 9, pp. 770–779, Sep. 1965, doi: 10.1109/TPAS.1965.4766256.

[107] C. Kim, D. Park, K. C. Noh, and J. Hwang, “Velocity and energy conversion efficiency characteristics of ionic wind generator in a multistage configuration,” *Journal of Electrostatics*, vol. 68, no. 1, pp. 36–41, Feb. 2010, doi: 10.1016/j.elstat.2009.09.001.

[108] S. B. Leonov, I. V. Adamovich, and V. R. Soloviev, “Dynamics of near-surface electric discharges and mechanisms of their interaction with the airflow,” *Plasma Sources Sci. Technol.*, vol. 25, no. 6, p. 063001, Nov. 2016, doi: 10.1088/0963-0252/25/6/063001.

[109] J. Qu *et al.*, “A review on recent advances and challenges of ionic wind produced by corona discharges with practical applications,” *J. Phys. D: Appl. Phys.*, vol. 55, no. 15, p. 153002, Dec. 2021, doi: 10.1088/1361-6463/ac3e2c.

[110] J. Zhang, L. Kong, J. Qu, S. Wang, and Z. Qu, “Numerical and experimental investigation on configuration optimization of the large-size ionic wind pump,” *Energy*, vol. 171, pp. 624–630, Mar. 2019, doi: 10.1016/j.energy.2019.01.086.

[111] D. H. Shin, S. H. Baek, and H. S. Ko, “Development of heat sink with ionic wind for LED cooling,” *International Journal of Heat and Mass Transfer*, vol. 93, pp. 516–528, Feb. 2016, doi: 10.1016/j.ijheatmasstransfer.2015.10.029.

[112] F. Llewellyn-Jones, “The mechanism of electrode erosion in electrical discharges,” *Platinum Metals Review*, vol. 7, no. 2, pp. 58–65, 1963.

[113] V. Yadav, V. K. Jain, and P. M. Dixit, “Thermal stresses due to electrical discharge machining,” *International Journal of Machine Tools and Manufacture*, vol. 42, no. 8, pp. 877–888, 2002.

[114] R. Tirumala and D. B. Go, “Multi-electrode assisted corona discharge for electrohydrodynamic flow generation in narrow channels,” *IEEE Transactions on Dielectrics and Electrical Insulation*, vol. 18, no. 6, pp. 1854–1863, 2012.

[115] M. J. Johnson, R. Tirumala, and D. B. Go, “Analysis of geometric scaling of miniature, multi-electrode assisted corona discharges for ionic wind generation,” *Journal of Electrostatics*, vol. 74, pp. 8–14, 2015.

[116] Y. Wu *et al.*, “Greener corona discharge for enhanced wind generation with a simple dip-coated carbon nanotube decoration,” *Journal of Physics D: Applied Physics*, vol. 50, no. 39, p. 395304, 2017.

[117] Z. Bo, K. Yu, G. Lu, S. Cui, S. Mao, and J. Chen, “Vertically oriented graphene sheets grown on metallic wires for greener corona discharges: lower power consumption and minimized ozone emission,” *Energy & Environmental Science*, vol. 4, no. 7, pp. 2525–2528, 2011.

[118] W. Yang, R. Zhu, and X. Zong, “ZnO Nanowire-Based Corona Discharge Devices Operated Under Hundreds of Volts,” *Nanoscale Res Lett*, vol. 11, no. 1, p. 90, Dec. 2016, doi: 10.1186/s11671-015-1217-4.

[119] A. Yehia and A. Mizuno, “Ozone generation by negative direct current corona discharges in dry air fed coaxial wire-cylinder reactors,” *Journal of applied physics*, vol. 113, no. 18, 2013, Accessed: Feb. 23, 2025. [Online]. Available: https://pubs.aip.org/aip/jap/article/113/18/183301/1014282

[120] B. Eliasson, U. Kogelschatz, and P. Baessler, “Dissociation of O2 in N2/O2 mixtures,” *Journal of Physics B: Atomic and Molecular Physics*, vol. 17, no. 22, p. L797, 1984.

[121] X. Zhang, B. J. Lee, H. G. Im, and M. S. Cha, “Ozone production with dielectric barrier discharge: effects of power source and humidity,” *IEEE transactions on plasma science*, vol. 44, no. 10, pp. 2288–2296, 2016.

[122] A. Zukeran *et al.*, “Investigation of inactivation process for microorganism collected in an electrostatic precipitator,” *Journal of Electrostatics*, vol. 93, pp. 70–77, 2018.

[123] Y. H. Usta, E. Çukur, Ç. Yıldırım, and U. K. Ercan, “Design of a portable, battery-powered non-thermal atmospheric plasma device and characterization of its antibacterial efficacies,” *Journal of Electrostatics*, vol. 99, pp. 1–8, 2019.

[124] J. Hyun, S.-G. Lee, and J. Hwang, “Application of corona discharge-generated air ions for filtration of aerosolized virus and inactivation of filtered virus,” *Journal of Aerosol Science*, vol. 107, pp. 31–40, 2017.

[125] R. G. Rice, “Applications of ozone for industrial wastewater treatment — A review,” *Ozone: Science & Engineering*, vol. 18, no. 6, pp. 477–515, Jan. 1996, doi: 10.1080/01919512.1997.10382859.

[126] H.-J. Kim, B. Han, C. G. Woo, and Y.-J. Kim, “Ozone emission and electrical characteristics of ionizers with different electrode materials, numbers, and diameters,” *IEEE transactions on industry applications*, vol. 53, no. 1, pp. 459–465, 2016.

[127] M. B. Awad and G. S. P. Castle, “Ozone Generation in an Electrostatic Precipitator With a Heated Corona Wire,” *Journal of the Air Pollution Control Association*, vol. 25, no. 4, pp. 369–374, Apr. 1975, doi: 10.1080/00022470.1975.10470092.

[128] T. Ohkubo, S. Hamasaki, Y. Nomoto, J.-S. Chang, and T. Adachi, “The effect of corona wire heating on the downstream ozone concentration profiles in an air-cleaning wire-duct electrostatic precipitator,” *IEEE transactions on industry applications*, vol. 26, no. 3, pp. 542–549, 1990.

[129] Z. Bo, K. Yu, G. Lu, S. Mao, J. Chen, and F. Fan, “Nanoscale Discharge Electrode for Minimizing Ozone Emission from Indoor Corona Devices,” *Environ. Sci. Technol.*, vol. 44, no. 16, pp. 6337–6342, Aug. 2010, doi: 10.1021/es903917f.

[130] J. Wang, T. Zhu, J. Wang, Y. Cai, and X. Li, “Optimization of a green solid-state fan for electronics cooling applications,” *Sustainable Energy Technologies and Assessments*, vol. 39, p. 100703, 2020.

[131] J. R. Lee and E. Von Lau, “Effects of relative humidity in the convective heat transfer over flat surface using ionic wind,” *Applied Thermal Engineering*, vol. 114, pp. 554–560, 2017.

[132] G. Xiao, X. Wang, J. Zhang, M. Ni, X. Gao, and K. Cen, “Characteristics of DC discharge in a wire-cylinder configuration at high ambient temperatures,” *Journal of Electrostatics*, vol. 72, no. 1, pp. 13–21, 2014.

CHAPTER II : Modelling of the electric wind

In this chapter, we first present the mathematical model used to simulate the corona discharge and the resulting electric wind. Then, we introduce a novel approach for addressing complex electrode configurations. This approach requires numerically integrating only the Laplacian electric field to determine the electric field lines. Then, using the semi-analytical formulations previously developed, which consist in satisfactory approximations of the electric field and the space charge density, to determine the EHD force density. Therefore, the proposed method is easy to implement and computationally very efficient, as it does not require iterating on an unstructured mesh to solve the electrical equations, which is usually required in FEM or FVM. Furthermore, it avoids the convergence problems that may arise when solving the Gauss equation coupled to the continuity equations of the charged species. By optimizing the modeling process, we aim to achieve more accurate and realistic simulations of the corona discharge and the electrical wind over a wide variety of electrode configurations

II.1 Introduction

The first step in the modeling of the ionic wind is to calculate the electric field, the space charge density, and the EHD force density, which usually requires solving a system of coupled electrical equations composed of the Gauss equation and the continuity equations of the charged particles. Once the EHD force density is obtained, the next step is to solve the Navier–Stokes equations, to determine the spatial distribution of the gas velocity generated by the EHD force.

The system of electrical equations and the Navier–Stokes equations can be solved separately because the electric drift velocity of ions ($\sim 102\ \mathrm{m.s^{-1}}$) is, typically, two orders of magnitude higher than the electric wind velocity ($\sim 1\ \mathrm{m.s^{-1}}$). However, in certain applications of corona discharge, such as airflow control around airfoils [1], or corona discharge in air with high wind speeds [2], the background velocity of the gas can affect electric drift of ions. In such cases, the electrical equations and the Navier–Stokes equations cannot be decoupled.

The solution of electrical equations that describe the corona discharge phenomena has been approached with a wide variety of numerical techniques. For instance, early studies by Atten [3] and McDonald et al [4] used the finite difference method to iteratively solve the Gauss equation coupled with the continuity equation. Davies and Hoburg [5] proposed an alternative technique, employing the finite element method (FEM) combined with the method of characteristic (MOCs). However, in these studies, the charge density on the wire is taken as a boundary condition and, since it is unknown, different strategies must be followed to determine its value. According to the method proposed by Kaptsov [6], the narrow ionization region around the coronating electrode can be dealt as an effective boundary condition for the electric field. This approach, often referred to as Kaptsov's assumption, states that electric field on the corona wire remains constant at the threshold value for corona onset. This approximation has been used by Zhao and Adamiak [7, 8] to evaluate the charge density on the corona electrode surface in the simulation of corona discharge in pin-plate and pin-grid configurations. They developed a hybrid numerical algorithm based on the boundary element method, the FEM, and the MOCs. Other numerical techniques employed by researchers include combining FEM and a donor cell method [9], using pseudo transient relaxation and finite volume discretization (FVM) [10], or implementing a particle-in-cell method to simulate transient corona [11].

Although all these numerical approaches have certainly helped improve our understanding of corona discharge, their implementation can be complex and computationally expensive. Furthermore, after solving the electrical equations, the Navier–Stokes equations must be integrated, which is normally done using computational fluid dynamics (CFD) simulations based on FEM or FVM [7, 8]. Therefore, to speed up the computation time, asymptotic and semi-analytical models of the stationary corona discharge have been developed in the past. For example, Seimandi et al [12] have proposed an asymptotic model for wire-to-wire corona discharges that divides the discharge space into two narrow ionization regions around the electrodes and one larger region between them. Inside each region, they established a simplified quasi-analytical solution for the electric field and the space charge. This solution is then used to estimate the velocity of the ionic wind. In previous studies, the authors have also obtained semi-analytical solutions of the corona discharge [13-15], which provided simple relations for the spatial distributions of electrons, ions, electric field, and the EHD force density. Using this information, the ionic wind has been successfully simulated [16-18]. However, these semi-analytical solutions are only applicable to simple electrode configurations, such as wire-to-cylinder, wire-to-plate, and point-to-plate.

II.2 Modelling electric discharge: Fluid model

The modeling of corona discharge often relies on the fluid model, which simplifies the complexity of electromagnetic and transport phenomena within a plasma environment. This type of model is based on the concept of a continuous medium, where particles (electrons, ions, and neutrals) are treated as continuous phases rather than discrete entities [19, 20]. The fluid model thus enables the description of the plasma's macroscopic properties, such as charge density, drift velocity, and partial pressures, which vary as functions of space and time.

In this framework, the plasma generated by the corona discharge is considered as an electrical fluid, where charged particles move under the influence of electric fields. The continuous medium approach uses conservation equations and constitutive laws to describe the motion of charges. Fluid equations account for momentum and energy transfers, incorporating specific terms to represent interactions among electrons, ions, and neutral particles. This typically includes Poisson's equation for the distribution of the electric field, the continuity equations for charge conservation, and the Navier-Stokes or momentum conservation equation to describe flow dynamics. These equations can be summarized as follows:

II.2.1 Continuity Equations (for ions and electrons)

The continuity equations for particles generated within an electric discharge describe the conservation of charge and mass in the plasma created during the discharge process. These equations are crucial for understanding the dynamics of charged particles, such as electrons and ions, in various types of electrical discharges, including corona, glow, and arc discharges.

The continuity equation for charge density in an electric discharge is expressed mathematically as:

$$\frac{\partial N_i}{\partial t} + \nabla.\mathbf{J}_i = R_i \tag{II.1}$$

Here, N_i is the number density of species i (electrons or ions), $\mathbf{J}_i$ is the flux of species i, and R_i is the production rate of species i: it represents the balance between ionization and recombination processes which controls the distribution of charged species.

II.2.2 Momentum transport Equations

The momentum transport of the species, which in the case of a discharge can be a mixture of electrons, ions, and neutral particles. They are typically written as:

$$m_i \left(\frac{\partial v_i}{\partial t} + (v_i.\nabla) v_i \right) = -\nabla p_i + \mathbf{F}_i + \boldsymbol{\nabla}.\boldsymbol{\tau_i} \tag{II.2}$$

where m_i is the mass of species i, v_i is the velocity, p_i is the pressure, and $\mathbf{F}_i$ is the force on species i, often due to electric and magnetic fields, with $\boldsymbol{\tau_i}$ representing the viscous stress tensor.

II.2.3 Poisson's Equation (for the electric potential)

The spatial distribution of the electric field is obtained by solving Poisson's equation with the boundary conditions provided by the electrode geometry and the charge density distribution.

$$\nabla^2 \phi = \frac{\rho_c}{\varepsilon_0} \tag{II.3}$$

where ϕ is the electric potential, ρ_c is the charge density (sum of ion and electron charges), and ε_0 is the permittivity of free space.

The electric field E is then obtained from the gradient of the electric potential:

$$E = -\nabla\phi \tag{II.4}$$

II.2.4 Navier-Stokes equations

The Navier-Stokes equations are fundamental in fluid dynamics and describe the motion of viscous fluid substances, such as those found in electrical discharges. In the context of an electric discharge, these equations help model the behavior of charged and neutral particles in a plasma state, where both fluid dynamics and electromagnetic forces are in interaction.

The Navier-Stokes equations can be expressed in their general form as:

$$\rho\frac{Dv}{Dt} = -\nabla p + \mu\nabla^2 v + \mathbf{f} \tag{II.5}$$

where:

- ρ is the fluid density,
- v is the velocity field of the fluid,
- p is the pressure,
- μ is the dynamic viscosity,
- **f** represents body forces (such as gravitational or electromagnetic forces),
- $\frac{D}{Dt} = \frac{\partial}{\partial t} + (v.\nabla)$ is the material derivative, which accounts for changes following a fluid particle.

II.2.5 Coupling Between the Equations

The coupling between these four equations — **continuity equations**, **momentum equations**, **Poisson's equation**, and **Navier-Stokes equations** — can be summarized as follows:

II.2.5.1 Electric Field and Charge Density

- Poisson's equation connects the electric field ($E = -\nabla\phi$) to the charge density ρ , which is determined by the number densities of electrons and ions.
- The charge density is influenced by the continuity equations, which describe how particle densities change over time due to ionization, recombination, and transport processes.

II.2.5.2 Particle Motion and Fluid Flow

- The momentum equations for the charged particles and the Navier-Stokes equations for the gas particle describe the motion of particles under the influence of forces such as the electric force ($q_i E$), pressure force and viscous forces.
- The velocities of the particles affect the flux terms in the continuity equations, and the charge density distribution influences the electric field, which, in turn, affects the particle velocities.
- Therefore, the motion of the particles (as described by the momentum equations and the Navier-Stokes equations) and the change in particle densities (as described by the continuity equations) are coupled.

II.2.5.3 Feedback Loop

- The electric field (calculated from Poisson's equation) affects the particle motion via the forces in the Navier-Stokes equations, which in turn affects the charge densities (via the continuity equations).
- As the particles move and undergo ionization/recombination, the charge density changes, altering the electric field via Poisson's equation.
- This creates a dynamic feedback loop between the electric field, the charge densities, and the fluid flow.

II.2.6 Numerical Solution

Due to the complexity of these coupled equations particularly because they are nonlinear and involve multiple scales (e.g., space, time, and velocity) they are typically solved numerically. As discussed above the common methods used include:

- Finite Difference Method (FDM)
- Finite Element Method (FEM)
- Finite Volume Method (FVM)

These methods allow for the simulation of how the electric field, charge densities, and fluid motion evolve over time, which is essential for understanding and predicting the behavior of corona discharge and other plasma phenomena.

II.3 Modelling corona discharge

In the study of corona discharge, a common approximation is to consider only three types of charged particles: electrons, positive ions, and negative ions. This simplification is based on the predominant roles these particles play in the ionization processes and charge transport within the discharge region. Another reason for these simplifications is the reduction of complexity: Including only these three particle types simplifies mathematical models and simulations, making it feasible to analyse and predict discharge behaviour without losing essential physical insights. In this context, assuming a stationary corona discharge, the governing equations can be simplified to:

$$-\nabla.\mathbf{J}_e = (\alpha - \eta)|\mathbf{J}_e| \quad \text{(II.6)}$$

$$\nabla.\mathbf{J}_p = \alpha|\mathbf{J}_e| \quad \text{(II.7)}$$

$$-\nabla.\mathbf{J}_n = \eta|\mathbf{J}_e| \quad \text{(II.8)}$$

$$\nabla.\mathbf{E} = \frac{e_0}{\varepsilon_0}\left(N_p - N_e - N_n\right) \quad \text{(II.9)}$$

where subscripts e, p and n correspond to electrons, positive ions and negative ions; $\mathbf{J}_i$ and N_i denotes the flux and the number density of particles of type i ($i = e, p$ and n), respectively; E is the electric field, α and η are the ionization and attachment coefficients, respectively; and e_0 is the elementary charge($e_0 \approx 1.602 \times 10^{-19}$C). The flux of each type is given as $\mathbf{J}_i = \mu_i N_i E$, where μ_i is the electrical mobility of particle i($\mu_p = 1.8$ and $\mu_n = 2.4\ \mathrm{cm}^2.\mathrm{s}^{-1}.\mathrm{V}^{-1}$) [21].

The ionization coefficient is expressed by the following expression [22]:

$$\alpha = A_1 \exp\left(-\frac{B_1}{E}\right) \tag{II.10}$$

where $A_1 = 8.97 \times 10^3 \text{cm}^{-1}$ and $B_1 = 1.45 \times 10^3 \text{V/cm}$.

And the attachment coefficient can be interpolated from the data provided by Eliasson and Kogelschatz [22] as follows:

$$\eta = \alpha_1 + \alpha_2 E + \alpha_3 E^2 + \alpha_4 E^3, \quad (1.1 \times 10^4 \leq E \leq 2.0 \times 10^5 \text{ V/cm}) \tag{II.11}$$

where $\alpha_1 = 100.7 \text{ cm}^{-1}$, $\alpha_2 = -1.27 \times 10^{-3} \text{V}^{-1}$, $\alpha_3 = 6.618 \times 10^{-9} \text{cm/V}^2$ and $\alpha_4 = -1.416 \times 10^{-14} \text{cm}^2/\text{V}^3$.

II.3.1 New Approach for modeling DC corona discharge

To solve Equation (II.6)-(II.11), K. Yanallah et al. [23] introduced a novel approach that, for the first time, derived analytical expressions for the electric field, electron density, and ion density across wire-to-cylinder, wire-to-plate, and point-to-plate electrode configurations. This breakthrough significantly reduced the computational effort required for numerical simulations. In the present work, this novel approach was adapted to address complex electrode configurations. The method relies only on numerically integrating the Laplacian electric field equation to determine the electric field lines. Using semi-analytical formulations previously developed by K. Yanallah et al. [15], accurate approximations of the Gaussian electric field and space-charge density are achieved, facilitating the determination of the electro-hydrodynamic (EHD) force density. The proposed method offers notable advantages in terms of simplicity and computational efficiency, as it eliminates the need for iterative computations on unstructured meshes, a common requirement in finite element methods (FEM) or finite volume methods (FVM). Additionally, this approach circumvents the convergence challenges typically associated with solving the Gauss equation in conjunction with the continuity equations for charged species. By optimizing the modeling process, we seek to enable more accurate and realistic simulations of corona discharge phenomena and the resulting electrical wind across a broad range of electrode configurations.

In the DC corona discharge, both the drift of electrons and ions are parallel to the electric field, the system of partial differential equations (II.6)-(II.11) can be transformed into a system of ordinary differential equations using the electric field lines as coordinate lines. Thus, applying the divergence theorem to a flux tube of electric field lines (see Figure II.1), the governing equations along any field line can be written as

$$\pm\frac{1}{\Delta S}\frac{d}{dl_a}[\Delta S J_e] = (\alpha - \eta)J_e, \tag{II.12}$$

$$\mp\frac{1}{\Delta S}\frac{d}{dl_a}\left[\Delta S J_p\right] = \alpha J_e, \tag{II.13}$$

$$\pm\frac{1}{\Delta S}\frac{d}{dl_a}[\Delta S J_n] = \eta J_e, \tag{II.14}$$

$$\frac{1}{\Delta S}\frac{d}{dl_a}[\Delta S E] = \mp\frac{e_0}{\varepsilon_0}\left(N_p - N_e - N_n\right), \tag{II.15}$$

$$J_e = \mu_e N_e E, J_p = \mu_p N_p E \text{ and } J_n = \mu_n N_n E, \tag{II.16}$$

where the upper (lower) sign is for the negative (positive) polarity, J_e, J_p, J_n, and E are the magnitudes of their corresponding vectors, dl_a is an infinitesimal displacement along the electric field line, and ΔS is an element of surface perpendicular to the field line, which is a function of l_a (the arc length along the field line). If the physical problem has continuous translational symmetry (2D problem), ΔS reduces to an elementary line segment perpendicular to the field line.

The conservation equation for the corona current density, $j = e_0(J_e + J_p + J_n)$, can be obtained by combining (II.12)-(II.14),

$$\frac{1}{\Delta S}\frac{d}{dl_a}[\Delta S j] = 0 \tag{II.17}$$

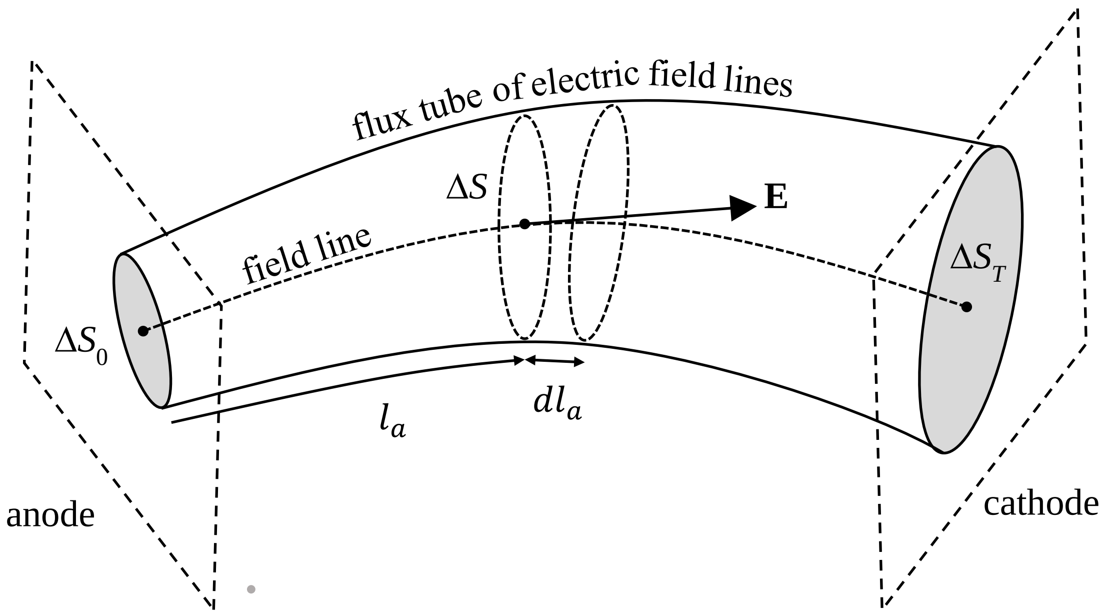

Figure II.1. Schematic illustration of a flux tube of electric field lines connecting the anode and the cathode.

The set of equations (II.12)-(II.15) is analogous to those derived by Seimandi et al. [12] for modeling steady wire-to-wire corona discharges, yielding results that align well with experimental observations.

The integration of (II.12)-(II.14) yields

$$J_e \quad = \frac{\Delta S_0 J_{e0}}{\Delta S} \exp\left[\mp \int_0^{l_a} (\alpha - \eta) dl_a\right] \tag{II.18}$$

$$J_p = \frac{\Delta S_0}{\Delta S} J_{p_0} \mp \frac{1}{S}\int_0^{l_a} \alpha J_e \Delta S dl_a = \frac{\Delta S_0}{\Delta S}\left(J_{p_0} \mp J_{e_0}\int_0^{l_a} \alpha\, exp\left(\pm\int_0^{l_a}(\alpha-\eta)dl_a{}'\right)dl_a\right) \tag{II.19}$$

$$J_n = J\,\frac{\Delta S_0}{\Delta S} J_{n_0} \pm \frac{1}{S}\int_0^{l_a} \eta J_e \Delta S dl_a = \frac{\Delta S_0}{\Delta S}\left(J_{n_0} \pm J_{e_0}\int_0^{l_a} \eta\, exp\left(\pm\int_0^{l_a}(\alpha-\eta)dl_a{}'\right)dl_a\right) \tag{II.20}$$

where J_{e0}, J_{p_0}, J_{n_0} and ΔS_0 are evaluated at the sharp high voltage electrode.

Moreover, integrating (II.17) we obtain

$$j\Delta S = j_0 \Delta S_0 = \text{const.} \tag{II.21}$$

In the positive corona (negative corona), the space charge is mostly due to the positive ions (negative ions). Therefore, as shown in previous works [15], the magnitude of the electric field along the field line can be obtained by direct integration of (II.15):

$$E(l_a) = \frac{1}{\Delta S}\sqrt{(\Delta S_0 E_0)^2 + c_p \Delta S_T \int_0^{l_a} \Delta S dl_a} \tag{II.22}$$

where subscripts 0 and T denote that the corresponding physical quantities are evaluated at the corona electrode and at the ground (the cathode), respectively, and $c_i = 2j_T/(\varepsilon_0 \mu_i)$, where $j_T$is the current density at the cathode.

The value of E_0 can be determined using Kaptzov's assumption, which states that the electric field on the corona electrode remains constant for a wide range of applied voltages. Therefore, Peek's law for the threshold field of corona discharge can be used to obtain E_0. Kaptsov's hypothesis is especially suitable for corona wires centered inside axisymmetric grounded electrodes, or corona wires away from grounded electrodes, since these configurations favor the charge density and electric field to be constant at any plane section of the corona wire [24]. However, refined simulations of corona discharge in hyperbolic point-plane configuration using direct ionization criteria show that Kaptsov's hypothesis, even if it may not be entirely accurate, does not introduce significant errors in predicting the total corona current [25]. Of course, some deviations can be expected with increasing voltage, as the effect of the space charge becomes more important. Kaptsov's hypothesis may not be applicable to corona discharge with high gas velocities, which can modify the space charge distribution [2].

For single curvature corona electrodes, which is the case for wires, the electric field on the corona electrode predicted by Peek's law is given as [26]

$$E_0 = 31 \text{ kV cm}^{-1} \delta \left(1 + \frac{0.308}{\sqrt{\delta r_0}}\right) \tag{II.23}$$

where r_0 is the equivalent radius of the wire in cm and $\delta = (p/p_0)/(T/T_0)$ is an environmental factor that depends on the ratios of the actual gas pressure to the atmospheric pressure ($p_0 = 101325\, Pa$), and the actual gas temperature to the room temperature ($T_0 = 298$ K). For electrodes with curvature (e.g., needles, spheres, etc.), Peek's equation can still be used provided that r_0 is replaced by an equivalent radius electrode [25, 26].

In complex geometries, the numerical integration of the set of partial differential equations (II.6)-(II.8). can often be time consuming. However, using (II.22) and adopting the Deutsch assumption of undistorted field lines [27], the solution of the problem can be reduced to integrating only the Laplace equation, followed by an iterative root-finding algorithm. This strategy which is schematically presented in Figure II.2, consists of the following steps:

1. Numerically integrating Laplace's equation for the electric potential, ϕ, subjected to the appropriate boundary conditions:

$$\nabla^2\phi = 0 \tag{II.24}$$

   where the electric potential at the anode (the corona electrode) is fixed, $\phi = \phi_0$, and at the cathode it is zero, $\phi = 0$.

2. Calculating the electric field,

$$E = -\nabla\phi \tag{II.25}$$

3. Computing the electric field lines and the value of ΔS along the field lines.
4. Assigning a trial value to the current density on the cathode, j_T.
5. Computing the magnitude of the electric field along the field lines using (II.22) and (II.23).

6. Evaluating the path integral of the electric field between the anode and the cathode along the field lines,

$$\phi_{calc} = \int_0^{L_a} E\, dl_a \tag{II.26}$$

   where L_a is the total length of the electric field line.

7. Testing whether the difference between ϕ_0 and ϕ_{calc} meets the desired convergence criterion, ζ

$$|\phi_{calc} - \phi_0| = \zeta \tag{II.27}$$

If it does not, the value of j_T must be decreased if $\phi_{calc} > \phi_0$, or, conversely, it must be increased if $\phi_{calc} < \phi_0$. Steps 5 to 7 are then repeated until the convergence criterion is finally satisfied.

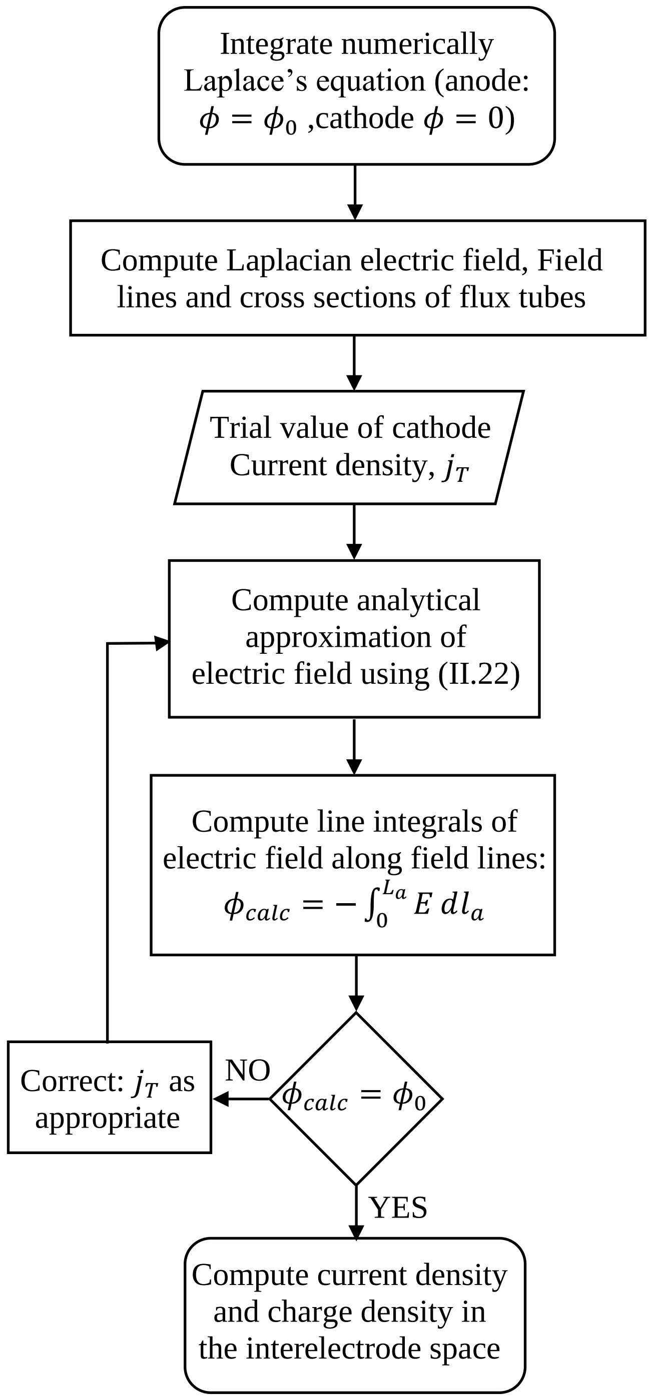

Figure II.2. Flow chart of the calculation procedure

When the convergence criterion is met, both the electric field magnitude inside the physical domain and the electric current density on the cathode are then known. Therefore, the current density and the (positive) space charge density at any point in interelectrode space can be determined as

$$j = \frac{j_T \Delta S_T}{\Delta S} \tag{II.28}$$

$$q_p = e_0 N_p = \frac{j_T \Delta S_T}{\mu_p E \Delta S} \tag{II.29}$$

Therefore, if a more accurate solution is required, the process can be restarted by integrating Poisson's equation in place of Laplace's equation, using the computed space charge density.

II.3.2 Analytical approach for the DC corona discharge

Equations (II.18)-(II.20) can be solved analytically or semi-analytically for certain symmetric and simple electrode configurations, such as wire-to-cylinder or wire-to-plate arrangements.

II.3.2.1 Analytical Solution for a Wire-Cylinder Configuration

The system under study consists of a long wire w inside a coaxial cylinder (see Figure II.3), with dry air at atmospheric pressure filling the space between the wire and the coaxial cylinder. The wire, with a radius r_0, is subjected to a negative DC voltage ϕ, while the outer electrode, with radius R_c, is grounded. The applied voltage is sufficiently high to stabilize the corona discharge in a steady-state condition.

In the cylindrical coordinates, the surface ΔS will be replaced in equations (II.12)-(II.15) by $2\pi r$. Therefore, the expressions of the electric field and the electrons and the ions density will be obtained.

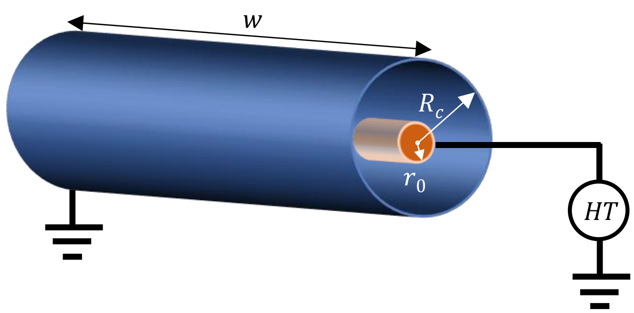

Figure II.3. Wire-Cylinder Corona Discharge Configuration

II.3.2.1.1 Electric field distribution

After integrating equation (II.15), the electric field distribution can be expressed as:

$$E = \sqrt{\frac{c^2}{r^2} + D^2} \tag{II.30}$$

where $c \approx E_0 r_0$ and $D = \sqrt{I/(2\pi\varepsilon_0 L\mu_n)}$.

The value of the parameter c can be obtained from the integral of the electric field between the electrodes.

$$\phi = c\left[\ln\left(\frac{R}{r_0}\right) - \ln\left(1 + \sqrt{1 + \left(\frac{DR}{c}\right)^2}\right) + \ln(2) + \sqrt{1 + \left(\frac{DR}{c}\right)^2} - 1\right] \tag{II.31}$$

where ϕ is the absolute value of the negative high voltage applied to the wire. Soria et al. and Feng, among others, have derived similar expression for the electric field and potential [28, 29].

II.3.2.1.2 Electron density distribution

The electron density is only important in the active region of the corona discharge. According to the numerical simulation results [13], the electric field in that region can be satisfactorily approximated by the Laplacian electric field. Therefore, the ionization and attachment coefficient will be expressed as

$$\alpha = A_1 \exp(-B_2 r) \tag{II.32}$$

$$\eta = \alpha_1 + \frac{\alpha_2}{r} + \frac{\alpha_3}{r^2} + \frac{\alpha_4}{r^3} \tag{II.33}$$

Where $B_2 = B_1/(E_0 r_0), \alpha_1 = \alpha_1$, $\alpha_2 = \alpha_2 E_0 r_0$, $\alpha_3 = \alpha_3 (E_0 r_0)^2$ and $\alpha_4 = \alpha_4 (E_0 r_0)^3$.

Substituting (II.32) and (II.33) in (II.12) and integrating along the radial coordinate, the following expression for the electron density is obtained,

$$N_{\mathrm{e}}(r) = N_e(r_0) \frac{\mu_e(r_0) E_0}{\mu_e E} \left(\frac{r_0}{r}\right)^{\alpha_2 + 1} \times \exp \begin{bmatrix} \frac{A_1}{B_2} \exp(-B_2 r_0) - \exp\left((-B_2 r)\right) - \alpha_1 (r - r_0) \\ + \alpha_3 \left(\frac{1}{r} - \frac{1}{r_0}\right) + \frac{\alpha_4}{2} \left(\frac{1}{r^2} - \frac{1}{r_0^2}\right) \end{bmatrix} \tag{II.34}$$

where the ratio of electron velocities, $\mu_e(r_0) E_0 / \mu_e E$ can be evaluated using

$$\mu_e E = b_1 + b_2 E = b_1 + b_2 \frac{E_0 r_0}{r} \tag{II.35}$$

with $b_1 = 1.42 \times 10^7 \mathrm{cm/s}$ and $b_2 = 257.3\ \mathrm{cm}^2/(\mathrm{Vs})$.

II.3.2.1.3 Positive ion density distribution

The electric current is mainly transported by the positive ions in the ionization region. Therefore, the current on the wire surface is given by

$$I = 2\pi e_0 r L \mu_p N_p(r_0) E_0, \tag{II.36}$$

Integrating (II.13) and using (II.36) as a boundary condition for the positive ion density on the wire, the spatial distribution of positive ions is expressed as

$$N_{\mathrm{p}}(r) = \frac{I}{2\pi L e_0 E_0 r_0 \mu_{\mathrm{p}}} \left[\frac{A_1}{2\pi L e_0} - A_1 r_0 E_0 \int_{r_0}^{r} B_2 r_0 \exp(-B_2 r_0) \mathrm{d}r \right] \tag{II.37}$$

II.3.2.1.4 Negative ion density distribution

The density of negative ions can also be expressed as

$$N_n(r) = \frac{I}{2\pi L e_0 \mu_{\mathrm{n}} r E} = \frac{1}{2\pi L e_0 \mu_{\mathrm{n}} r \sqrt{\frac{C^2}{r^2} + D^2}} \tag{II.38}$$

It is worth noting that a similar approach was used for analyzing the positive corona discharge, focusing on the electric field, electron density, and positive ion density. Negative ions were not considered in the positive polarity due to their low concentration.

II.3.2.2 Analytical solution for a wire-plate electrodes configuration

For a wire-to-plate electrodes configuration, the surface ΔS is expressed using bipolar coordinates [30, 31] which are particularly adequate to formulate electrostatic problems in wire-plate electrode geometry, since the coordinate curves $\sigma = \text{const.}$ coincides with the Laplacian field lines Figure II.4. Therefore, in order to solve semi-analytically (II.6)-(II.9), the same strategy as that adopted for wire-to-cylinder electrodes configuration is used.

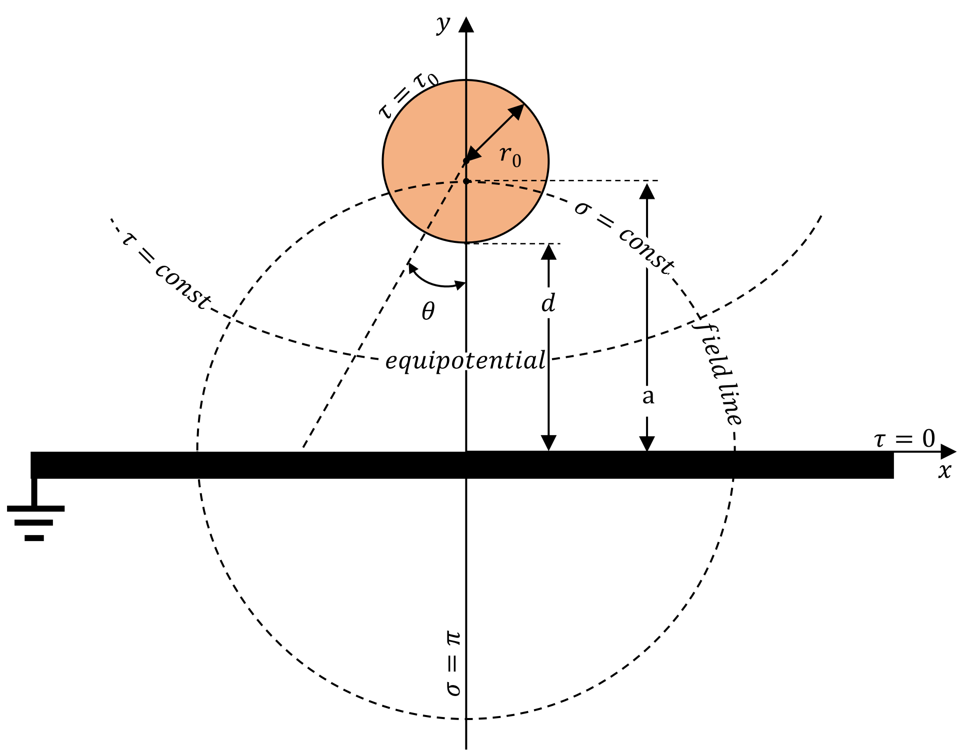

Figure II.4. Fig-Bipolar coordinates system (σ, τ) used to describe the corona discharge in the wire to-plate electrode geometry. Coordinate lines are shown as dashed lines. (Not to scale).

The equations defining the surface ΔS as function of the bipolar coordinates σ and τ and the correspondence between Cartesian coordinates are

$$\Delta S = \frac{\mathrm{a}}{\cosh\tau - \cos\sigma}, \qquad x = \frac{\mathrm{a}\sin\sigma}{\cosh\tau - \cos\sigma}, \qquad y = \frac{\mathrm{a}\sinh\tau}{\cosh\tau - \cos\sigma}, \tag{II.39}$$

Where distance a is related to the wire radius, r_0, and the electrode separation, d, as $\mathrm{a} = \sqrt{(d + r_0)^2 - r_0^2}$.

The elementary displacement along the coordinate lines is expressed as:

$$dl_a = \Delta S\ d\Delta S \tag{II.40}$$

II.3.2.2.1 Electric field

In the drift region, the space charge is mainly constituted by ions with the same polarity as that of the corona wire, that is, $N_i = J_i/(\mu_i E) = J_T S_T/(\mu_i E S)$, where $i = p$ in the positive corona, and $i = n$ and in the negative corona. Therefore, integration of (II.15) using the expression of ΔS gives [15],

$$E(\sigma,\tau) = \frac{1}{\Delta S(\sigma,\tau)}\left[\frac{(\Delta S_0 E_0)^2 - c_i \dfrac{a^3/\sin^2\sigma}{1-\cos\sigma}}{\left(\dfrac{2}{\tan\sigma}\tan^{-1}\left[\left(\dfrac{1+\cos\sigma}{\sin\sigma}\right)\tanh\left(\dfrac{\tau}{2}\right)\right] + \dfrac{\sinh\tau}{\cosh\ \tau - \cos\ \sigma}\right)_{\tau_0}^{\tau}}\right]^{1/2}, \tag{II.41}$$

where $c_i = 2j_T/(\varepsilon_0\mu_i)$ and E_0 is the electric field on the wire surface, which can be estimated using Peek's law [101].

II.3.2.2.2 Electron density distribution

Since electrons are confined to the plasma region, bipolar coordinates can be approximated by polar coordinates, and the flux of electrons can be obtained by direct integration of (II.12).

$$J_e \quad = \frac{\Delta S_0 J_{e0}}{\Delta S}\exp\left[\mp\int_0^l (\alpha-\eta)dl_a{}'\right] \approx \frac{S_0 J_{e0}}{S}\exp\left[\mp\int_{r0}^r (\alpha-\eta)dr'\right] = J_{e0} f(r) \tag{II.42}$$

where

$$f(r) = \left(\frac{r_0}{r}\right)^{1\mp a_2} \exp\left[\begin{array}{c} \pm\frac{A_1}{B_2}(\exp(-B_2 r) - \exp(-B_2 r_0)) \pm a_1(r - r_0) \\ \mp a_3\left(\frac{1}{r} - \frac{1}{r_0}\right) \mp \frac{a_4}{2}\left(\frac{1}{r^2} - \frac{1}{r_0^2}\right) \end{array}\right] \quad \text{(II.43)}$$

and J_{e0} is the electron flux on the wire surface. As usual, the upper (lower) sign corresponds to positive (negative) corona.

Then the electron density can be calculated by the relation $J_e = \mu_e n_e \mathrm{E}$

II.3.2.2.3 Positive ions density distribution

Within the plasma region, the flux of positive ions can be obtained from (II.13) as follows

$$J_p = \frac{\Delta S_0}{\Delta S} J_{p0} \pm \frac{1}{\Delta S}\int_0^{l_a} \Delta S \alpha J_e dl_a{}' \approx \frac{r_0}{r} J_{p0} \pm \int_{r_0}^{r} A_1 r' \exp\left(-B_2 r'\right) J_{e0} f(r') dr' \quad \text{(II.44)}$$

where J_{p0} is the flux of positive ions on the wire.

In the positive corona, it must be $J_{p0} = 0$, owing to the polarity of the wire. In the negative corona, the current on the wire is contributed by positive ions and electrons, but $J_{p0} \gg J_{e0}$. Therefore $J_0 \approx J_{p0}$, and flux of positive ions on the wire can be linked to the current on the plate using (II.21),

$$J_{p0} \approx \frac{1}{e_0} J_T \frac{\Delta S_T}{\Delta S_0} \quad \text{(II.45)}$$

Equation (II.44) is particularly useful in the case of a negative corona, since positive ions are confined to the plasma region. However, in a positive corona, positive ions accumulate in the drift region. In such a case, a more straightforward evaluation of the positive ion flux can be obtained using (II.21),

$$J_p \approx \frac{\Delta S_T J_T}{\Delta S} - J_e \quad \text{(II.46)}$$

which further simplifies in the drift region to $J_p \approx \Delta S_T J_T / \Delta S$, since $J_p \gg J_e$.

The positive ions density can be calculated by the relation $J_p = \mu_p n_p$E.

II.3.2.2.4 Negative ions density distribution

In the positive corona, the number density of negative ions is much weaker than that of electrons, and they are confined to a short distance from the wire. Therefore, they will not contribute significantly to the electric force and will be omitted. In contrast, in the negative corona, negative ions are present both in the corona plasma region and in the drift region. In the corona plasma region, the flux of negative ions can be deduced from (II.14) as

$$J_n = \frac{\Delta S_0}{\Delta S} J_{n0} + \frac{1}{\Delta S}\int_0^{l_a} \Delta S \eta J_e dl_a{}' \approx \frac{1}{r}\int_{r_0}^{r} r' \left(\alpha_1 + \frac{\alpha_2}{r'} + \frac{\alpha_3}{r'^2} + \frac{\alpha_4}{r'^3}\right) J_{e0} f(r') dr' \quad \text{(II.47)}$$

where it has been taken into account that $J_{n0} = 0$, due to the polarity of the wire.

However, once the electron flux and the positive ion flux have been previously determined, a more convenient relation can be obtained using (II.21),

$$J_n = \frac{\Delta S_T J_T}{\Delta S} - J_p - J_e \quad \text{(II.48)}$$

which is valid in the whole discharge gap. In the drift region, where $J_n \gg J_e$ and $J_n \gg J_p$, the above equation can be approximated as $J_n \approx \Delta S_T J_T / \Delta S$.

Finally, the negative ions density can be calculated by the relation $J_n = \mu_n n_n$E.

II.4 The EHD force expression

In general, the EHD force acting on air is calculated using the Coulomb force [33]:

$$\boldsymbol{F} = e_0 \left(N_p\text{-N}_n\text{-N}_e\right)\boldsymbol{E} \quad \text{(II.49)}$$

It can be expressed as a function of the flux of charged species,

$$\mathbf{F} = e_0\left(\frac{\mathbf{J}_p}{\mu_p} - \frac{\mathbf{J}_n}{\mu_n} - \frac{\mathbf{J}_e}{\mu_e}\right) \quad \text{(II.50)}$$

II.4.1 The EHD force for the positive polarity using the new approach

In positive corona discharge, ionization is confined to a thin layer around the wire electrode, within which the electron density dominates over that of the other charged species [34, 35]. However, since the thickness of this layer is negligible compared to the inter-electrode distance (d), the majority of momentum transfer from the charged particles to the neutral molecules occurs in the drift region, where positive ions are predominant. Consequently, the force density acting on the fluid can be simplified as:

$$\boldsymbol{F} \approx e_0 N_p \boldsymbol{E} = e_0 \frac{\mathbf{J}_p}{\mu_p} \tag{II.51}$$

Since the current transport in the drift region is primarily due to positive ions$(J \approx J_p)$, the electric force density is ultimately expressed as

$$F = \frac{1}{\mu_p} j_T \frac{\Delta S_T}{\Delta S} \tag{II.52}$$

II.4.2 The EHD force for the negative polarity using the new approach

Based on the modelling [17], asymptotic expressions of the EHD force can be obtained for the EHD force where the force is predominantly by the negative ions in the drift region. Using (II.52), and taking into account that $e_0(J_e + J_p + J_n)\,\Delta S = \text{const} = J_T S_T$, the EHD force can be approximated as

$$F = \frac{1}{\mu_n} e_0 J_n \approx \frac{1}{\mu_n} j_T \frac{\Delta S_T}{\Delta S} \tag{II.53}$$

Near the wire, positive ions are predominant therefore, the EHD force can be expressed as

$$F = \frac{1}{\mu_p} e_0 J_p \approx \frac{1}{\mu_p} j_T \frac{\Delta S_T}{\Delta S} \tag{II.54}$$

Between the ionization region and the drift region, the fluxes of positive and negative ions are nearly equal in magnitude but flow in opposite directions. Consequently, the electrohydrodynamic (EHD) force can be neglected in this narrow region: $F = 0$.

II.5 Hydrodynamic Model of the Gas

During the generation of the electric discharge, an interaction between the plasma and the neutral gas takes place. This interaction results in the movement of the gas, which has acquired part of the momentum from the charged species, and can be described by the Navier-Stokes equations, which are partial differential equations.

Indeed, the Navier-Stokes equations represent the conservation of momentum and mass density. Assuming that the flow is Newtonian and that the gas, “air,” is incompressible, the EHD-induced flow from the corona discharge will generally be turbulent [7, 36]. In this context, the conventional time-averaging approach for the conservation equations of momentum and mass density, known as the Reynolds-Averaged Navier-Stokes (RANS) equations, will be used in this work. If we neglect gravity and assume a steady-state regime, these equations can be written as follows:

$$\rho(v.\nabla)v = -\nabla p + \lambda\nabla^2 v + \nabla.\boldsymbol{\tau}_R + \mathbf{F} \tag{II.55}$$

$$\nabla.v = 0 \tag{II.56}$$

Where v is the average velocity of the gas, λ is the dynamic viscosity of air, p is the gas pressure, and $\boldsymbol{\tau}_R$ is the Reynolds stress tensor. The system of partial differential equations (the Navier-Stokes equations) will be closed using the standard two-equation turbulence model, k -epsilon $(k - \varepsilon)$ [37].

k -epsilon model

The k -epsilon model is one of the most commonly used models for turbulence modeling. It is a two-equation transport model proposed by Jones and Launder [38]. The Reynolds stresses are calculated using the Boussinesq relation [39]:

$$\boldsymbol{\tau}_R = -\frac{2}{3}\rho k\mathbf{I} + \mu_i\left(\frac{\partial V_i}{\partial x_j} - \frac{\partial V_j}{\partial x_i}\right) \tag{II.57}$$

where $\mathbf{I}$ is the identity tensor, k is the turbulent kinetic energy, and μ_t is the turbulent viscosity.

The transport equations for turbulent kinetic energy k and dissipation rate ε are:

$$\rho\nabla\cdot(k\mathbf{V}) = \nabla\cdot\left[\left(\eta+\frac{\mu_i}{\sigma_k}\right)\nabla k\right] + \mu_t\left(\frac{\partial V_j}{\partial x_i}+\frac{\partial V_i}{\partial x_j}\right)\frac{\partial V_j}{\partial x_i} - \rho\varepsilon$$
$$\rho\nabla\cdot(\varepsilon\mathbf{V}) = \nabla\cdot\left[\left(\eta+\frac{\mu_i}{\sigma_\varepsilon}\right)\nabla\varepsilon\right] + C_{\varepsilon 1}C_\mu\rho k\left(\frac{\partial V_j}{\partial x_i}+\frac{\partial V_i}{\partial x_j}\right)\frac{\partial V_j}{\partial x_i} - C_{\varepsilon 2}\rho\frac{\varepsilon^2}{k} \quad \text{(II.58)}$$

where ε is the turbulent dissipation rate.

The turbulent viscosity (μ_t), turbulent kinetic energy (k), and dissipation rate (ε) are related by the expression:

$$\mu_t = \rho C_\mu \frac{k^2}{\varepsilon} \quad \text{(II.59)}$$

The values of the empirical parameters $C_\mu, C_{\varepsilon 1}, \sigma k, \sigma_\varepsilon$et $C_{\varepsilon 2}$are given in the following table.

Table II.1. Les constantes empiriques utilisées dans le modèle k-ε [37]

C_μ	$C_{\varepsilon l}$	σ_k	σ_ε	$C_{\varepsilon 2}$
0,09	1,44	1,00	1,30	1,92

We chose to use the OpenFOAM (Open-Source Field Operation and Manipulation) [40] to model electric wind, as several authors have done [41-43]. It supports both structured and unstructured meshes, offering options for internal mesh generation with tools like “block Mesh” and “snappy Hex Mesh”, or importing meshes from external software. The software uses the finite volume method (FVM) as its primary numerical approach, with various options for discretization schemes (such as upwind and central-difference), linear solvers (e.g., PCG, GMRES), and time integration schemes (e.g., Euler, Crank-Nicolson), all aimed at achieving accurate and efficient solutions. Boundary conditions in OpenFOAM are highly flexible, allowing users to specify types like velocity, pressure, and temperature, as well as advanced conditions such as periodic and symmetry boundaries each essential for accurately defining physical constraints on the model.

II.6 Conclusion

In this chapter, we have shown the possibility of successfully modeling a steady corona discharge by taking as the starting point the Laplacian electric field lines and using approximated analytical expressions of the electric field intensity along the field lines. Then, applying a simple root-finding algorithm to match the electric field circulation along each field line to the actual voltage drop, the space charge and the EHD force density can be determined. The proposed approach has the advantage of being able to easily treat arbitrary electrode configurations of practical interest, since only the Laplace equation needs to be integrated numerically. Furthermore, the model is robust, since it avoids the convergence problems that may arise when integrating the Gauss equation coupled to the continuity equation for charge species. Finally, we presented previously established analytical expressions for the electric field and charged particles in the inter-electrode space have been obtained for both positive and negative wire-to-cylinder and wire-to-plate DC corona discharge in air.

Reference

[1] E. Moreau, C. Louste, G. Artana, M. Forte, and G. Touchard, “Contribution of Plasma Control Technology for Aerodynamic Applications,” Plasma Processes and Polymers, vol. 3, no. 9, pp. 697–707, 2006, doi: 10.1002/ppap.200600059.

[2] C. Guerra-Garcia, N. C. Nguyen, T. Mouratidis, and M. Martinez-Sanchez, “Corona Discharge in Wind for Electrically Isolated Electrodes,” Journal of Geophysical Research: Atmospheres, vol. 125, no. 16, p. e2020JD032908, 2020, doi: 10.1029/2020JD032908.

[3] P. Atten, “Etude mathématique du problème du champ électrique affecté par un flux permanent d’ions unipolaires et application à la théorie de la sonde froide,” Nov. 1969.

[4] J. R. McDonald, W. B. Smith, H. W. Spencer III, and L. E. Sparks, “A mathematical model for calculating electrical conditions in wire-duct electrostatic precipitation devices,” Journal of Applied Physics, vol. 48, no. 6, pp. 2231–2243, Jun. 1977, doi: 10.1063/1.324034.

[5] J. L. Davis and J. F. Hoburg, “Wire-duct precipitator field and charge computation using finite element and characteristics methods,” Journal of Electrostatics, vol. 14, no. 2, pp. 187–199, Aug. 1983, doi: 10.1016/0304-3886(83)90006-2.

[6] A. A. Petrov, E. A. Pushkareva, and B. A. Shabdukaȓimov, “Effect of pressure in correlation spectral analysis of multicomponent gases,” J Appl Spectrosc, vol. 46, no. 3, pp. 235–240, Mar. 1987, doi: 10.1007/BF00660204.

[7] L. Zhao and K. Adamiak, “Effects of EHD and External Airflows on Electric Corona Discharge in Point-Plane/Mesh Configurations,” IEEE Transactions on Industry Applications, vol. 45, no. 1, pp. 16–21, Jan. 2009, doi: 10.1109/TIA.2008.2009389.

[8] L. Zhao and K. Adamiak, “Numerical simulation of the effect of EHD flow on corona discharge in compressed air,” in 2011 IEEE Industry Applications Society Annual Meeting, Oct. 2011, pp. 1–7. doi: 10.1109/IAS.2011.6074283.

[9] P. L. Levin and J. F. Hoburg, “Donor cell-finite element descriptions of wire-duct precipitator fields, charges, and efficiencies,” IEEE Transactions on Industry Applications, vol. 26, no. 4, pp. 662–670, Jul. 1990, doi: 10.1109/28.55991.

[10] A. J. Medlin, C. A. J. Fletcher, and R. Morrow, “A pseudotransient approach to steady state solution of electric field-space charge coupled problems,” Journal of Electrostatics, vol. 43, no. 1, pp. 39–60, Mar. 1998, doi: 10.1016/S0304-3886(97)00167-8.

[11] B.-L. Qin and P. D. Pedrow, “Particle-in-cell simulation of bipolar dc corona,” IEEE Transactions on Dielectrics and Electrical Insulation, vol. 1, no. 6, pp. 1104–1118, Dec. 1994, doi: 10.1109/94.368652.

[12] P. Seimandi, G. Dufour, and F. Rogier, “An asymptotic model for steady wire-to-wire corona discharges,” Mathematical and Computer Modelling, vol. 50, no. 3, pp. 574–583, Aug. 2009, doi: 10.1016/j.mcm.2009.03.005.

[13] K. Yanallah, F. Pontiga, Y. Meslem, and A. Castellanos, “An analytical approach to wire-to-cylinder corona discharge,” Journal of Electrostatics, vol. 70, no. 4, pp. 374–383, Aug. 2012, doi: 10.1016/j.elstat.2012.05.002.

[14] K. Yanallah and F. Pontiga, “A semi-analytical stationary model of a point-to-plane corona discharge,” Plasma Sources Sci. Technol., vol. 21, no. 4, p. 045007, Jul. 2012, doi: 10.1088/0963-0252/21/4/045007.

[15] K. Yanallah, F. Pontiga, and J. H. Chen, “A semi-analytical study of positive corona discharge in wire–plane electrode configuration,” J. Phys. D: Appl. Phys., vol. 46, no. 34, p. 345202, Aug. 2013, doi: 10.1088/0022-3727/46/34/345202.

[16] K. Yanallah, F. Pontiga, M. R. Bouazza, and J. H. Chen, “The effect of the electric wind on the spatial distribution of chemical species in the positive corona discharge,” J. Phys. D: Appl. Phys., vol. 50, no. 33, p. 335203, Jul. 2017, doi: 10.1088/1361-6463/aa7b24.

[17] M. R. Bouazza, K. Yanallah, F. Pontiga, and J. H. Chen, “A simplified formulation of wire-plate corona discharge in air: Application to the ion wind simulation,” Journal of Electrostatics, vol. 92, pp. 54–65, Apr. 2018, doi: 10.1016/j.elstat.2018.02.001.

[18] M. Bouadi, K. Yanallah, M. R. Bouazza, and F. Pontiga, “Effect of the Variation of the Electrode Geometrical Configuration on the Electric Wind Velocity Produced by an Electric Corona Discharge,” in ICREEC 2019, A. Belasri and S. A. Beldjilali, Eds., Singapore: Springer, 2020, pp. 465–474. doi: 10.1007/978-981-15-5444-5_58.

[19] A. A. Kulikovsky, “The mechanism of positive streamer acceleration and expansion in air in a strong external field,” J. Phys. D: Appl. Phys., vol. 30, no. 10, p. 1515, May 1997, doi: 10.1088/0022-3727/30/10/019.

[20] R. Morrow, “Theory of negative corona in oxygen,” Phys. Rev. A, vol. 32, no. 3, pp. 1799–1809, Sep. 1985, doi: 10.1103/PhysRevA.32.1799.

[21] S. Ohashi and K. Hidaka, “A method for computing current density and electric field in electrical discharge space using current flow-line coordinate1,” Journal of Electrostatics, vol. 43, no. 2, pp. 101–114, Apr. 1998, doi: 10.1016/S0304-3886(97)00165-4.

[22] B. Eliasson, Basic Data for Modelling of Electrical Discharges in Gases: Oxygen. ABB Asea Brown Boveri, 1986.

[23] K. Yanallah et al., “A new numerical approach for efficient modeling of positive corona discharge and its associated electric wind,” J. Phys. D: Appl. Phys., vol. 56, no. 41, p. 415201, Jul. 2023, doi: 10.1088/1361-6463/ace456.

[24] “Computational study of glow corona discharge in wind: Biased conductor - ScienceDirect.”

[25] K. Adamiak, V. Atrazhev, and P. Atten, “Corona discharge in the hyperbolic point-plane configuration: direct ionization criterion versus an approximate formulation,” IEEE Transactions on Dielectrics and Electrical Insulation, vol. 12, no. 5, pp. 1015–1024, Oct. 2005, doi: 10.1109/TDEI.2005.1522195.

[26] M. Goldman and A. Goldman, “Chapter 4 - Corona Discharges,” in Gaseous Electronics, M. N. Hirsh and H. J. Oskam, Eds., Academic Press, 1978, pp. 219–290. doi: 10.1016/B978-0-12-349701-7.50009-2.

[27] R. S. Sigmond, “The unipolar corona space charge flow problem,” Journal of Electrostatics, vol. 18, no. 3, pp. 249–272, Oct. 1986, doi: 10.1016/0304-3886(86)90021-5.

[28] C. Soria, F. Pontiga, and A. Castellanos, “Plasma chemical and electrical modelling of a negative DC corona in pure oxygen,” Plasma Sources Sci. Technol., vol. 13, no. 1, p. 95, Nov. 2003, doi: 10.1088/0963-0252/13/1/012.

[29] J. Q. Feng, “An analysis of corona currents between two concentric cylindrical electrodes,” Journal of Electrostatics, vol. 46, no. 1, pp. 37–48, Mar. 1999, doi: 10.1016/S0304-3886(98)00057-6.

[30] R. B. Harvey, “Methods of Theoretical Physics. By P.M. Morse and H. Feschbach. 2vols., Pp.xxii, 1978. 120s. each vol. 1953.(McGraw-Hill),” The Mathematical Gazette, vol. 39, no. 327, pp. 80–81, Feb. 1955, doi: 10.2307/3611130.

[31] M. R. Spiegel, J. Liu, and S. Lipschutz, Mathematical handbook of formulas and tables, 3. ed. in Schaum’s outline series. New York: McGraw-Hill, 2009.

[32] F. W. (Frank W. Peek, Dielectric phenomena in high-voltage engineering. New York [etc.] McGraw-Hill Book Company, inc., 1929.

[33] J. P. Boeuf and L. C. Pitchford, “Electrohydrodynamic force and aerodynamic flow acceleration in surface dielectric barrier discharge,” Journal of Applied Physics, vol. 97, no. 10, p. 103307, May 2005, doi: 10.1063/1.1901841.

[34] J. Chen and J. H. Davidson, “Electron Density and Energy Distributions in the Positive DC Corona: Interpretation for Corona-Enhanced Chemical Reactions,” Plasma Chemistry and Plasma Processing, vol. 22, no. 2, pp. 199–224, Jun. 2002, doi: 10.1023/A:1014851908545.

[35] “Experimental investigation and numerical modelling of positive corona discharge: ozone generation - IOPscience.”

[36] S. Ould Ahmedou and M. Havet, "Effect of process parameters on the EHD airflow," Journal of Electrostatics, vol. 67, no. 2, pp. 222–227, May 2009, doi: 10.1016/j.elstat.2009.01.055.

[37] H. K. (Henk K. Versteeg, An introduction to computational fluid dynamics : the finite volume method. Harlow, Essex, England ; Longman Scientific & Technical : New York : Wiley, 1995.

[38] W. P. Jones and B. E. Launder, "The prediction of laminarization with a two-equation model of turbulence," International Journal of Heat and Mass Transfer, vol. 15, no. 2, pp. 301–314, Feb. 1972, doi: 10.1016/0017-9310(72)90076-2.

[39] J. (1842-1929) A. du texte Boussinesq, Essai sur la théorie des eaux courantes / par J. Boussinesq. 1877.

[40] "OpenFOAM." Available: https://www.openfoam.com/

[41] J. Batina, F. Noël, S. Lachaud, R. Peyrous, and J. F. Loiseau, "Hydrodynamical simulation of the electric wind in a cylindrical vessel with positive point-to-plane device," J. Phys. D: Appl. Phys., vol. 34, no. 10, p. 1510, May 2001, doi: 10.1088/0022-3727/34/10/311.

[42] P. Bérard, "Etude du vent ionique produit par décharge couronne à pression atmosphérique pour le contrôle d'écoulement aérodynamique," 2008.

[43] M. Goldman, A. Goldman, and R. S. Sigmond, "The corona discharge, its properties and specific uses," Pure and Applied Chemistry, vol. 57, no. 9, pp. 1353–1362, Jan. 1985, doi: 10.1351/pac198557091353.

CHAPTER III : Modeling of Positive Corona Discharge and its Associated Electric Wind

In this chapter, we will evaluate the accuracy and reliability of the numerical modeling of corona discharge presented in CHAPTER II. This evaluation involves validating the model against experimental measurements reported in the literature. The focus will be on both the electrical characteristics and the electrohydrodynamic (EHD) effects of the corona discharge. Additionally, we will explore the potential application of the numerical model in the design and optimization of EHD pumping such in heat transfer.

III.1 Introduction

The study of corona discharge phenomena has been a topic of significant interest due to its wide range of applications, from air purification to electrostatic precipitation and EHD pumps. Numerous researchers have contributed to the understanding and modeling of these phenomena. For instance, Yamamoto and Velkoff [1] investigated the electrical characteristics of wire-duct electrode configurations, providing experimental data crucial for model validation. Similarly, Elagin et al. [2] studied the gas velocity distribution generated by corona discharges, using particle image velocimetry (PIV) to measure flow velocities. Jewell-Larsen et al. [3] focused on the application of EHD air movers for cooling systems, presenting experimental setups that serve as benchmarks for numerical simulations. These works collectively provide a foundation for the validation and improvement of numerical models aimed at predicting both electrical and EHD behaviors of corona discharges. Similarly, to these works, in the present study, we will comprehensively evaluate the accuracy and reliability of the numerical modeling presented in the previous chapter by comparing its predictions with experimental measurements extensively reported in the literature. This evaluation serves a dual purpose.

First, it focuses on demonstrating the numerical model's ability to accurately predict the current-voltage characteristics of the corona discharge. The model's accuracy in replicating the spatial distribution of current intensity on the cathode will also be examined. This validation is crucial as it ensures that the numerical model can reliably simulate the electrical behavior of corona discharges, which are essential in various applications such as air purification, electrostatic precipitation, and surface treatment.

Second, the evaluation aims to verify the model's capability to quantitatively describe the ionic wind generated by the corona discharge. The validation process will involve comparing the numerical model's predictions of ionic wind characteristics with experimental data to ensure its accuracy and practical applicability.

After establishing the validity of the numerical technique through these rigorous tests, we will address the specific problem of EHD pumping between two parallel plates using positive corona discharge. This problem involves using the validated numerical model to explore and optimize the design and performance of EHD pumps, which are devices that use electrically induced flows to move fluids without mechanical components. The focus will be on understanding the underlying mechanisms, optimizing the parameters for efficient pumping, and evaluating the potential practical applications of this technology in various domains.

III.2 Results and discussion

As mentioned above, the validations of our model are twofold (1) electrical, to demonstrate the ability of the numerical modeling to accurately predict the current-voltage characteristic of the corona discharge and the spatial distribution of the current intensity on the cathode, and (2) EHD, to demonstrate its capability to quantitatively describe the ionic wind generated by the corona discharge.

III.2.1 Electrical validation

The wire-duct electrode configuration (Figure III.1), is commonly utilized as a case study in electrostatic precipitator research. In this setup, the corona wire, with a radius of r_0, is subjected to a high voltage, while the plates, positioned at a distance d from the wire, are grounded. Due to the symmetrical nature of this configuration, the problem can be analyzed in two dimensions. As detailed in CHAPTER II, the elementary normal section of the electric field flux tube, ΔS, simplifies to the line segment P_1P_2.

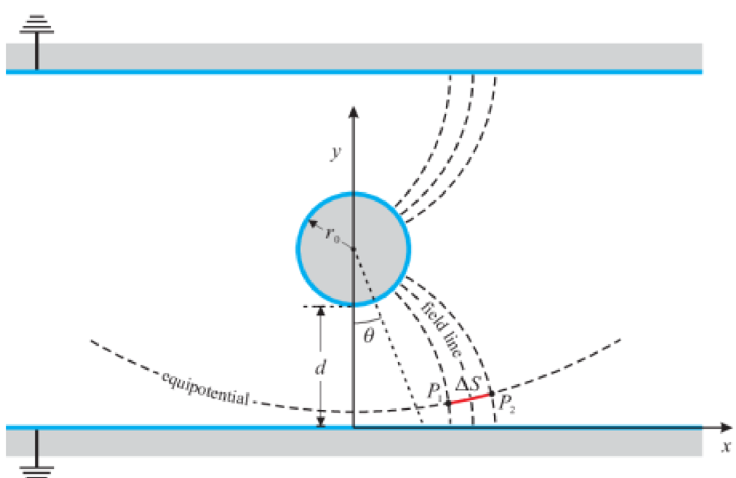

Figure III.1. Schematic representation of a wire-duct electrostatic precipitator (not to scale).

III.2.1.1 Current-Voltage Characteristic

Among other researchers, Yamamoto and Velkoff [1] have both experimentally and numerically investigated different variations of this electrode configuration. In their experimental setup, they used a corona discharge wire with a length of 19 cm and a radius of $r_0 = 0.1$ mm, with a wire-to-plate spacing of $d = 2.9$ cm. The wire was subjected to a high positive electrical potential ranging from 10 kV to 17.5 kV.

Figure III.2, the experimental measurements of the current intensity reported in [1] for different applied voltages are compared with the numerical results obtained in this study for the same geometrical parameters. The agreement with the experimental measurements is clearly satisfactory. The current-voltage characteristic adheres to the classical law $= c_1\,\phi(\phi - \phi_{onset})$ where c_1 is a constant and ϕ_{onset} is the corona inception voltage [4, 5].

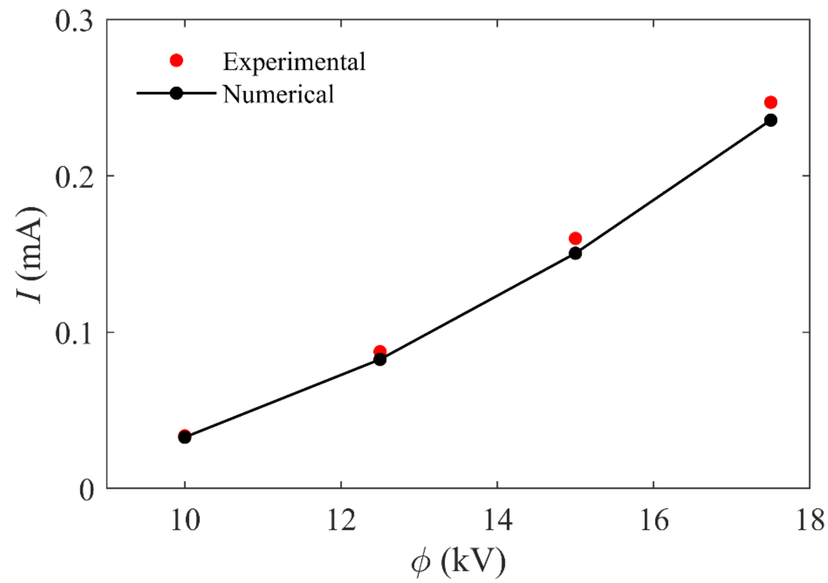

Figure III.2.Current-voltage characteristic of a positive corona wire-duct electrostatic precipitator, for a wire radius $r_0 = 0.1$ mm and a wire-plate separation $d = 2.9$ cm. The experimental points (solid circles) correspond to the measurements of Yamamoto and Velkoff [1].

In the HV laboratory at the Czech Technical University in Prague, a wire-duct electrostatic precipitator (ESP) was set up by Ziedan et al to compare the calculated and measured corona current-voltage characteristics for various ESP configurations [6]. The experimental setup, includes several key components:

- **Regulating Transformer:** A 220 V input transformer that feeds the HV circuit through a contactor switch, allowing the supply to be connected or disconnected.

- **High Voltage Transformer:** This transformer steps up the voltage from the regulating transformer. Its output is rectified by a circuit immersed in transformer oil and smoothed by a capacitor bank (two 0.25 μF, 100 kV capacitors in series). The resulting DC voltage, adjustable from 0 to 200 kV, is applied to the ESP through an 80 kΩ resistor to limit current in case of a flashover.

- **Discharge Wires:** Steel conductor with radius of 0.26 mm is suspended vertically between two collecting plates. The wire is terminated with smoothing steel spheres to avoid field intensification.

- **Collecting Plates:** Two steel plates, each measuring 125 cm in height and 250 cm in length, form the ESP duct. They are suspended vertically with adjustable spacing of 30 cm and 40 cm. The edges are curved outward to prevent field concentration.

- **Micro-Ammeter:** A shielded micro-ammeter measures the corona current from the discharge wire. The readings are recorded by a digital camera connected to a computer.

To measure the corona current-voltage characteristics from each discharge wire, a shielded micro-ammeter is connected to the discharge wire and the corona current is recorded with the increase of the applied voltage. All the measurements are made in HV laboratory of pressure = 1001.3 kPa and temperature = 22°C.

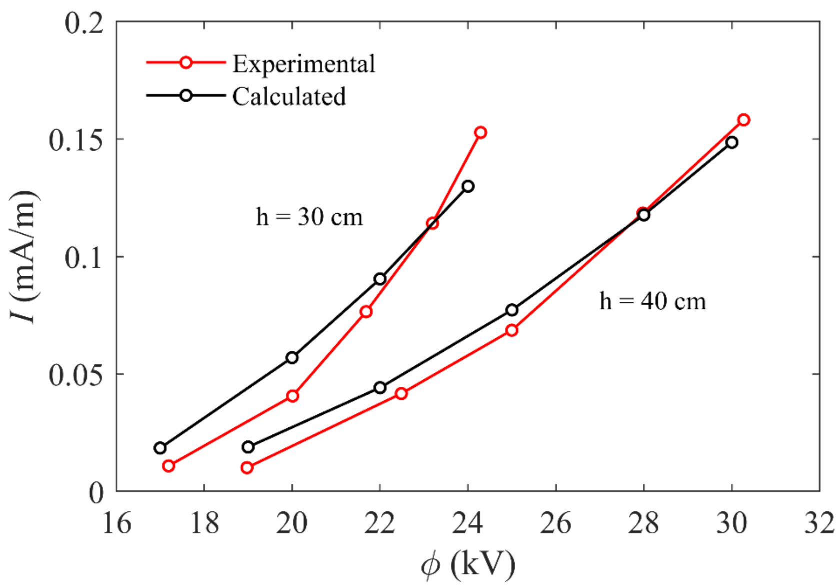

Figure III.3. Effect of plate-to-plate spacing on current-voltage characteristics of one-wire ESP $r_0 = 0.26\ mm$ *[6].*

As shown in Figure III.3, Ziedan's experimental current-voltage measurements are in satisfactory agreement with our calculations.

III.2.1.2 Current density distribution

Yamamoto and Velkoff [1] also measured the current density distribution on the cathode using an array of brass rods with a diameter of 1.6 mm, spaced 6.4 mm apart. The current density at each rod was measured by a micro-ammeter connected to the rod, while the rest were grounded. These measurements are compared with the results of the present numerical modeling in Figure III.4. The current density is normalized to its maximum value, which occurs at x = 0 cm, directly beneath the wire. Once again, the agreement between the numerical simulation and the experimental data is quite satisfactory. The current distribution follows a $cos^m\theta$ Warburg-type law, with $m \approx 4$.

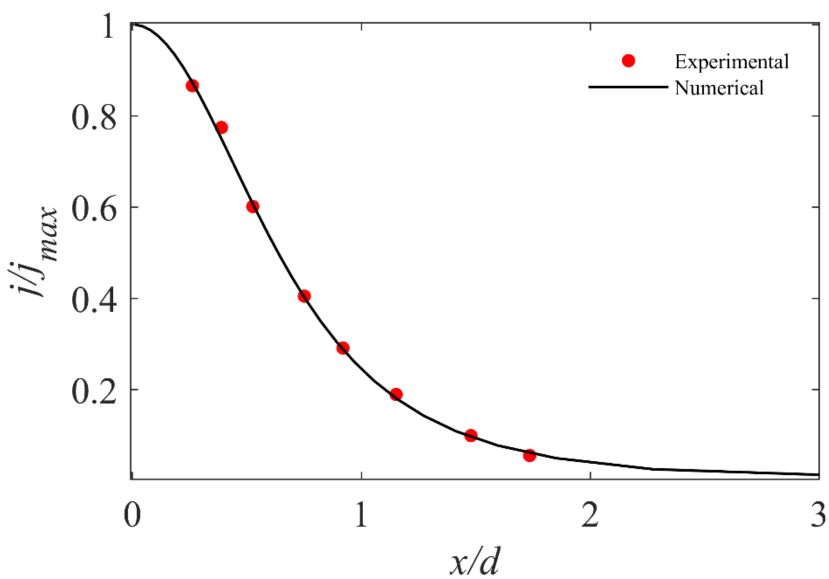

Figure III.4. Normalized current density distribution on the cathode of a wire-duct electrostatic precipitator for an applied voltage of $+15\ kV$ (wire radius $r_0 = 0.1\ mm$, wire-plate separation: $d = 2.9\ cm$. The experimental points (circles) correspond to the measurements of Yamamoto and Velkoff [1].

III.2.2 Electrohydrodynamic validation

To determine the gas velocity distribution generated by the corona discharge, it is essential to first evaluate the electrohydrodynamic (EHD) force, which is the driving force behind the gas motion. As discussed in CHAPTER II, once the EHD force is determined, the Navier-Stokes equations are integrated. For accurate integration, we assume the no-slip condition at all solid boundaries, which means that the fluid velocity at the boundary (relative to the boundary) is zero, reflecting the common physical situation where fluid adheres to the surface.

For this computational task, we will use the open-source solver OpenFOAM [7], which is a Computational Fluid Dynamics (CFD) software based on the finite-volume method. OpenFOAM is particularly well-suited for this purpose as it can model both laminar and turbulent flows with high accuracy. When dealing with fluid flows confined within narrow channels, we will assume laminar flow conditions. This assumption is based on the fact that in such narrow channels, the Reynolds number a dimensionless quantity used to predict flow patterns will not exceed the critical value required for the onset of turbulence. Therefore, the flow remains smooth and orderly.

In configurations where the flow is expected to be turbulent, we will employ the Reynolds-Averaged Navier-Stokes (RANS) k-epsilon turbulence model. This model is widely used in fluid dynamics to simulate the effects of turbulence, providing a good balance between computational efficiency and accuracy.

III.2.2.1 First validation

The electrohydrodynamic validation of the numerical model will be carried out by comparing the results with experimental measurements of gas velocity. These measurements have been reported for two different electrode arrangements: parallel wire-plate and wire-duct configurations. The first configuration, the parallel wire-plate, has been experimentally investigated by Elagin et al. [2]. They measured the gas velocity distribution using particle image velocimetry (PIV), a technique that allows for the visualization and measurement of flow velocities. In their experiments, Elagin et al. used a corona wire with a radius of $r_0 = 50$ μm and a wire-plate separation of $d = 15$ mm. The electric potential applied to the wire was varied within the range of 5 kV to 35 kV to study its effects on the gas velocity.

III.2.2.1.1 EHD force distribution

Figure III.5 illustrates the spatial distribution of the magnitude of the EHD force, which has been calculated numerically for the same electrode configuration used by Elagin et al., with an applied voltage of $+13.5$ kV. In the case of a positive corona discharge, the ionization region is confined to a thin layer around the anode, which is of negligible extent. Therefore, the space charge in the system is predominantly positive throughout. This causes the electric force to be directed towards the cathode along the electric field lines, represented by solid lines in the figure. The magnitude of this force is particularly significant directly beneath the wire, where both the electric field strength and the space charge density reach their maximum values. This concentration of force explains the localized effects observed in the experimental measurements and underscores the accuracy of the numerical model in replicating real-world phenomena.

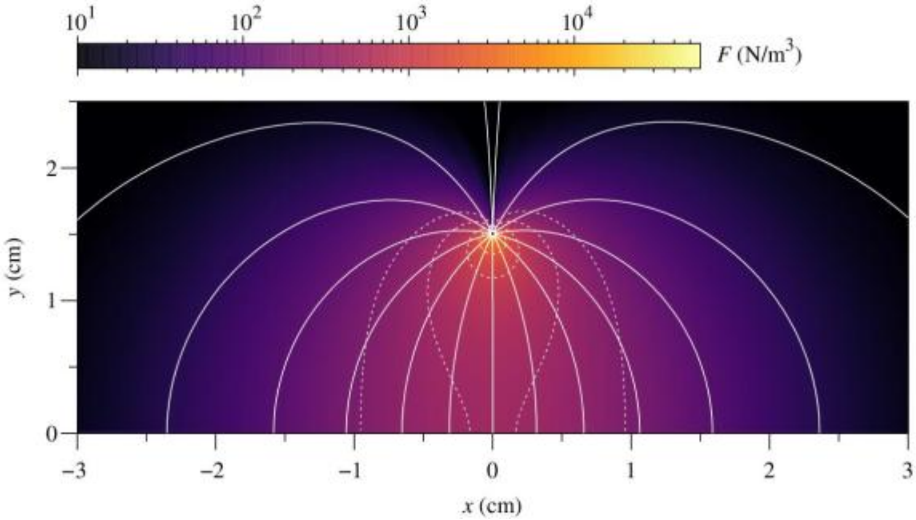

Figure III.5. 2D-spatial distribution of the EHD force density magnitude and electric field lines (solid lines) in the vicinity of the wire for an applied voltage $\phi = +13.5\ kV$ (wire radius: $r_0 = 50\ \mu m$, wire-plate separation: $d = 15\ mm$). Isolines of the force density (dashed lines) are drawn at 2×10^3, 10^3, 4×10^2 and $2 \times 10^2\ N/m^3$.

III.2.2.1.2 Gas velocity distribution

The 2D gas velocity field generated by this force density, simulated with the RANS k-epsilon turbulence model, is shown in Figure III.6 (a) and can be compared with the experimental measurements by Elagin et al., which are presented in Figure III.6 (b). As can be readily seen, both spatial distributions of velocity are globally very similar. The fluid is accelerated along the symmetry axis and, after impinging on the ground plate, the gas flow is deflected in opposite directions. The regions with the highest fluid velocities are located along the symmetry axis and along the plate. A quantitative comparison can be made based on the maximum values of velocities observed in each case: according to the numerical modeling, the maximum velocity is 3.6 m/s, while according to the experimental observation it is about 3.5 m/s. Therefore, the agreement is quite satisfactory.

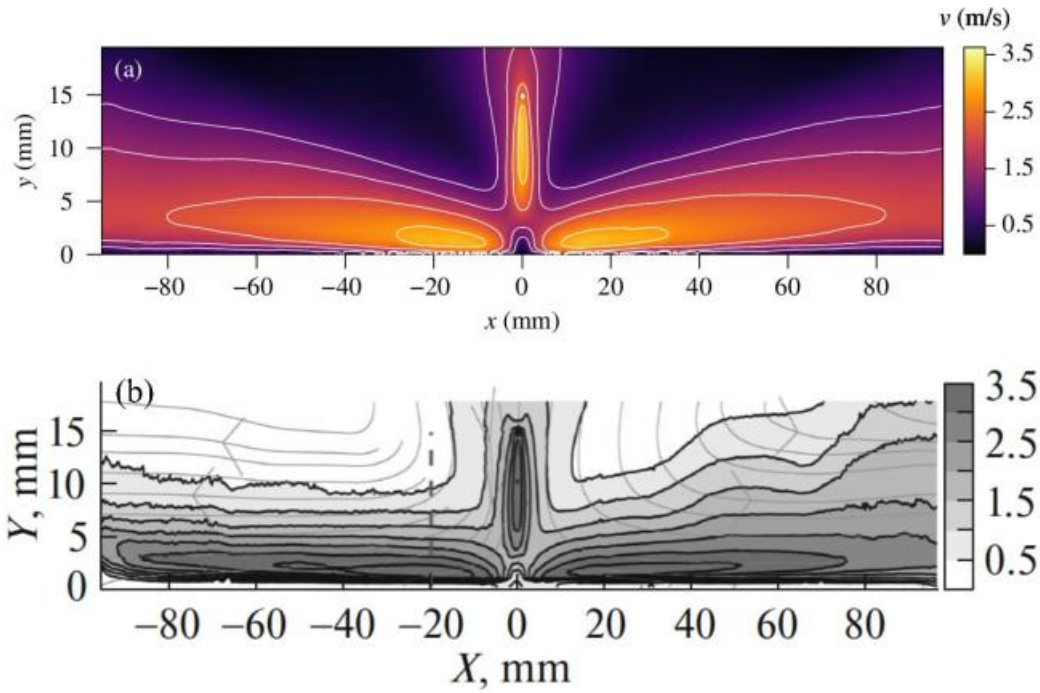

Figure III.6. 2D-spatial distribution of the velocity magnitude and their corresponding contour lines for an applied voltage $\phi = +13.5\ kV$ (wire radius: $r_0 = 50\ \mu m$, wire-plate separation: $d = 15\ mm$). (a) Numerical modeling. Isolines of the velocity magnitude are drawn at $2.8, 2.1, 1.5$ and $1\ m/s$. (b) Experimental measurements using PIV reported by Elagin et al [2].

III.2.2.2 Second validation

The second electrode arrangement chosen for electrohydrodynamic validation is the one utilized by Jewell-Larsen et al. [3] in their studies of EHD air movers based on positive corona discharge. This configuration is particularly significant for the development of efficient EHD cooling systems for laptop applications [8]. As illustrated in Figure III.7, the setup involves a wire-duct arrangement where the duct walls are made from insulating acrylic sheets measuring 7 cm in length and spaced 6 mm apart. Two gold-plated aluminum strips attached to the walls and grounded serve as collector electrodes. A corona wire with a radius of $r_0 = 12.5$ μm is used, and the collector strips, which are 5 mm wide, protrude 0.1 mm from the duct walls. The wire is positioned 4 cm from the duct entrance, with a horizontal distance of 6 mm between the wire's center and the strips.

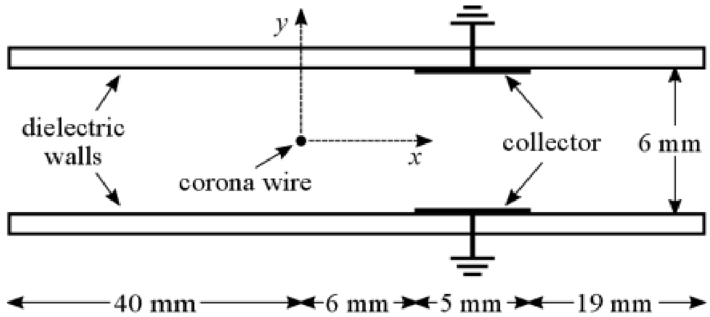

Figure III.7. Schematic representation of the EHD air mover device used by Jewell-Larsen et al [3] (not to scale).

III.2.2.2.1 EHD force distribution

As previously discussed, the first step in obtaining the velocity distribution involves determining the force density from the solution of the electrical equations. An example of such a computation is shown in Figure III.8, which presents the magnitude of the EHD force density along with the corresponding electric field lines for the same electrode arrangement used by Jewell-Larsen et al, with an applied voltage of $+10$ kV on the corona wire. The computational domain depicted in this figure is limited to the region between the anode and the cathode, where the EHD force is significant. Similar to the wire-plate configuration, the EHD force is particularly strong around the corona wire, reaching a magnitude of approximately 1.3×10^5 $\mathrm{N/m^3}$, which is two orders of magnitude higher than at the grounded electrodes.

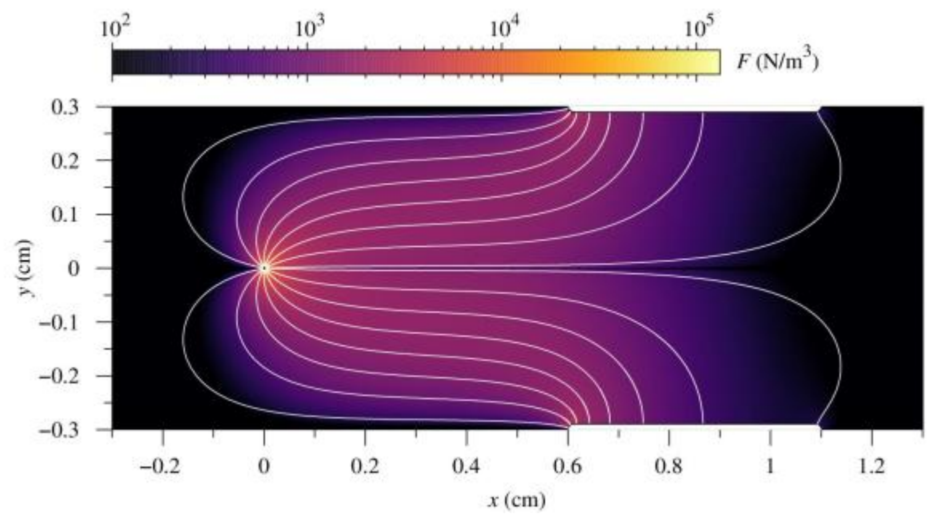

Figure III.8. 2D-spatial distribution of the EHD force density magnitude and electric field lines (solid lines) inside the EHD blower, for an applied voltage $\phi = +10$ kV (wire radius: $r_0 = 12.5$ μm).

III.2.2.2.2 Gas velocity distribution

After evaluating the EHD force density, the Navier-Stokes equations can be solved numerically to obtain the gas velocity distribution. For this simulation, the no-slip boundary condition is applied at the solid surfaces, and open boundary conditions for pressure are imposed at the duct's inlet and outlet. The simulation results, assuming laminar flow, are shown in Figure III.9. This figure illustrates the 2D spatial distribution of the gas velocity magnitude and the corresponding streamlines. The highest gas velocity is observed along the axis of symmetry, specifically at the entrance of the collector plates.

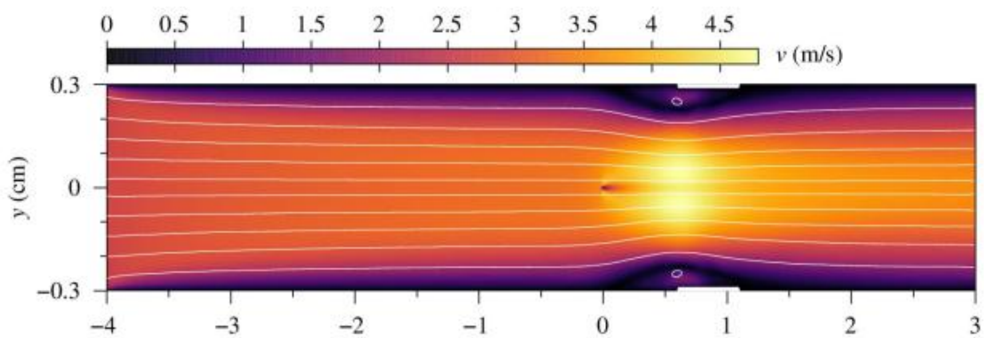

Figure III.9. 2D-spatial distribution of the velocity magnitude and their corresponding streamlines for an applied voltage $\phi = +10\ kV$ (wire radius: $r_0 = 12.5\ \mu m$).

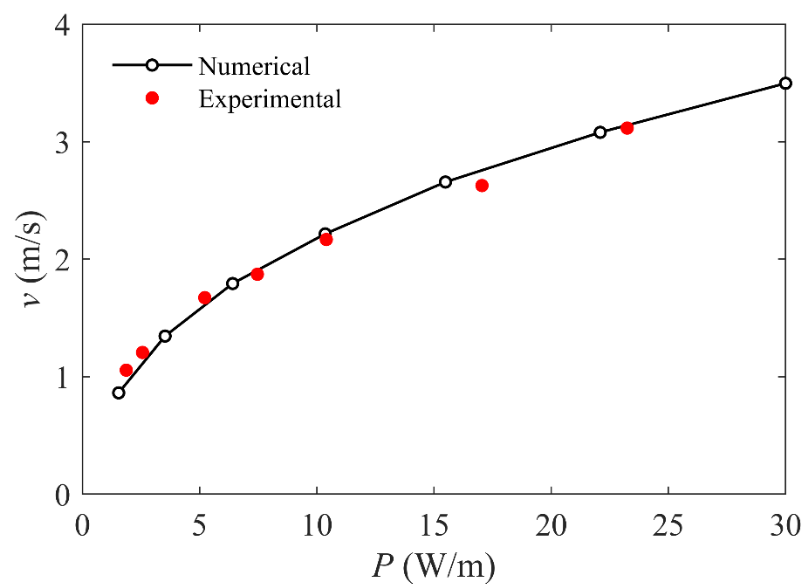

Figure III.10. Average velocity at the outlet of the duct as a function of the electric power per unit of length of corona wire according to the numerical simulation and its comparison with experiments. The experimental points (black circles) correspond to the measurements of Jewell-Larsen et al [3].

To determine the gas flow rate and the average velocity at the duct outlet, Jewell-Larsen et al. connected the EHD air mover to a wind tunnel. They measured the relative pressure drop across a calibrated nozzle using a digital pressure gauge. This setup allowed them to evaluate the airflow performance of the device as a function of the input electric power per unit length of the wire. Figure III.10 presents the measurements of the mean outlet velocity and compares them with the results of the current numerical simulation. The comparison indicates that the numerical model accurately replicates the EHD gas flow generated by the corona discharge in this electrode configuration.

III.3 Improved electrode configuration for EHD air movers

As previously discussed, the ongoing trend towards miniaturizing electronic components necessitates highly efficient cooling solutions to handle heat dissipation. In this context, EHD air pumps offer notable advantages over conventional rotary fans, particularly due to their superior heat transfer capabilities in small-scale applications. An optimal design for EHD air pump electrodes should be straightforward and durable without sacrificing efficiency, ensuring extended operational life before failure.

The electrode configuration of the EHD air blower depicted in Figure III.11 presents a significant drawback: the corona wire must be precisely positioned equidistantly between the two insulating plates. This task becomes increasingly difficult and error-prone as the blower's dimensions are reduced. Additionally, the corona wire can obstruct airflow and is prone to mechanical vibrations caused by electrical forces [9].

Therefore, this section introduces a modified electrode configuration inspired by Jewell-Larsen et al. [3]. As shown in Figure III.11, instead of a single corona wire positioned centrally in the channel, the proposed design features two corona electrodes with a radius of $r_0 =$ 12.5 μm, each partially embedded in the dielectric walls that confine the flow. This design maintains an effective corona discharge surface area similar to that of a single wire. As in the original configuration [3], two 5 mm wide strips protruding 0.1 mm from the walls serve as collectors for the corona discharge current, with a maintained separation of 6 mm between the wire and the collector strips.

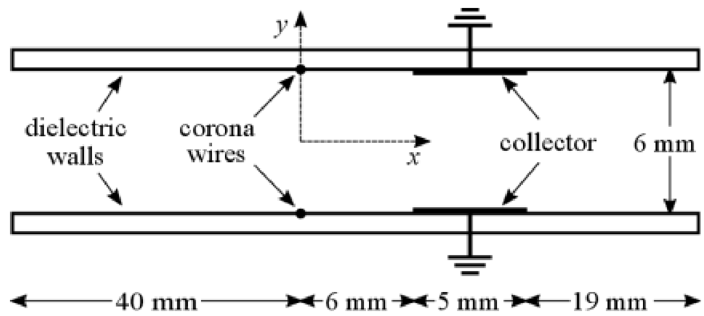

Figure III.11. Schematic representation of the improved EHD air mover (not to scale).

Figure III.12 presents the results of the numerical simulation for the current-voltage characteristics of the new configuration (with two corona wires) compared with the previous configuration (with one corona wire). The current intensity is slightly lower with two corona wires, although both configurations can be satisfactorily modeled with a $\phi(\phi - \phi_{onset})$ dependence, where $\phi_{onset} \approx 4.5$ kV. In the two-wire configuration, the usual shielding effect between adjacent discharge electrodes is certainly present. However, this effect is offset by the shorter distance between each corona wire and its nearest collector, resulting in higher ion density, electric field, and current density values within the fluid compared to the single-wire configuration. Thus, the lower current intensity observed in the new electrode configuration can be attributed to the different ways in which the current density is distributed over the collector strips in the two cases.

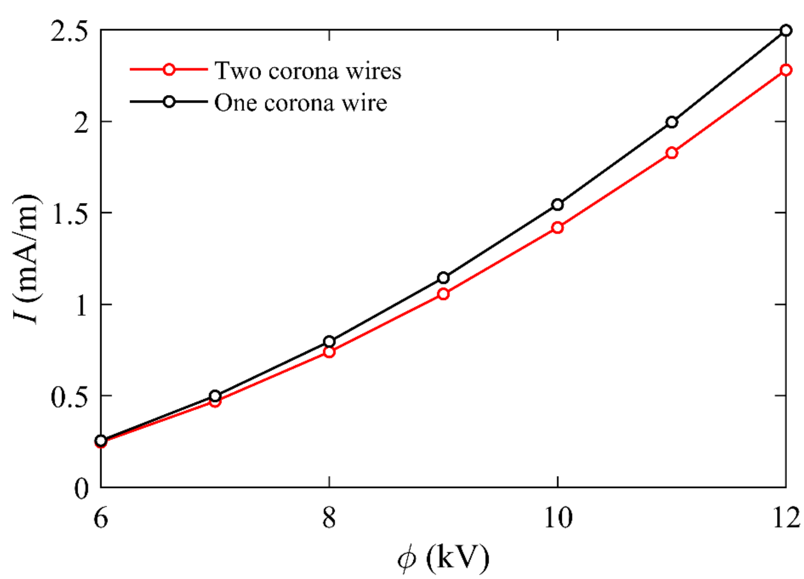

Figure III.12. Numerical simulation results for the current-voltage characteristic corresponding to the EHD blower with a single central corona wire (black circles) and two corona wires half embedded in the dielectric walls (white circles).

Figure III.13 and Figure III.14 illustrate the 2D spatial distributions of charge density and electric force density, respectively, for a voltage of 10 kV applied to the wires. In the new configuration, the maximum value of the electric force density is approximately 30 % higher than in the single-wire setup. Most of the space charge is concentrated near the dielectric plates, where the electric field lines run almost parallel to the plates. Conversely, the force density in the central part of the channel is negligible. This is in stark contrast to the single central wire configuration (shown in Figure III.8), where the electric force density was negligible near the dielectric walls but significant near the axis of symmetry.

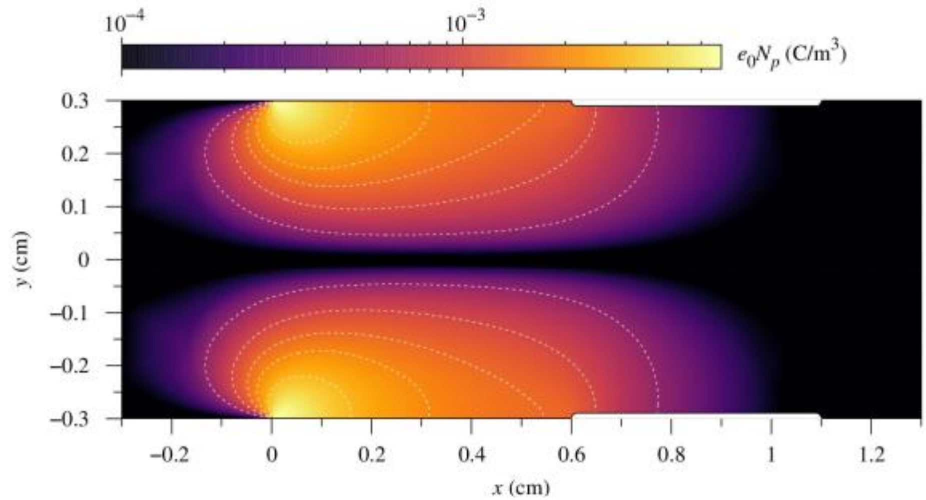

Figure III.13. 2D-spatial distribution of the charge density inside the improved EHD blower, for an applied voltage $\phi = +10\ kV$ and corona wires of radius $r_0 = 12.5\ \mu m$. Isolines of the charge density (dashed lines) are drawn at $5 \times 10^{-4}, 10^{-3}, 1.5 \times 10^{-3}, 2 \times 10^{-3}$ and $3 \times 10^{-3}\ C/m^3$

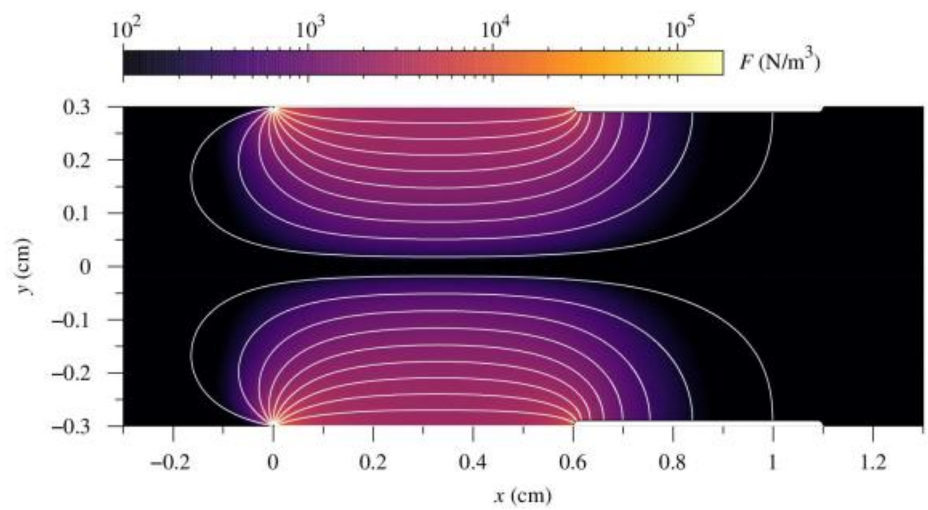

Figure III.14. 2D-spatial distribution of the EHD force density magnitude and electric field lines (solid lines) inside the improved EHD blower, for an applied voltage $\phi = +10\ kV$ and corona wires of radius $r_0 = 12.5\ \mu m$.

However, the current electrode configuration has the inherent advantage of accelerating the fluid near the walls, where the retarding force due to shear stress is stronger. This advantage is clearly illustrated in Figure III.15, which presents the 2D velocity distribution for an applied voltage of 10 kV to the corona wires. This flow pattern is particularly advantageous for cooling applications, as high fluid velocity along the walls enhances heat transfer between the walls and the fluid.

Compared to Figure III.9, the maximum velocity values in the current setup are now located closer to the walls and further downstream, between the two collector strips. Additionally, the recirculating eddies that previously formed near the collector strips (as seen in Figure III.9) have been completely eliminated. Although the maximum gas velocity within the blower in this configuration is about 10% lower than with a single corona wire, the average velocity at the duct's exit is nearly the same, if not slightly higher in the new setup. Naturally, as depicted in Figure III.16, the velocity profiles at the outlet differ significantly, reflecting the upstream EHD force distribution that drives the gas flow.

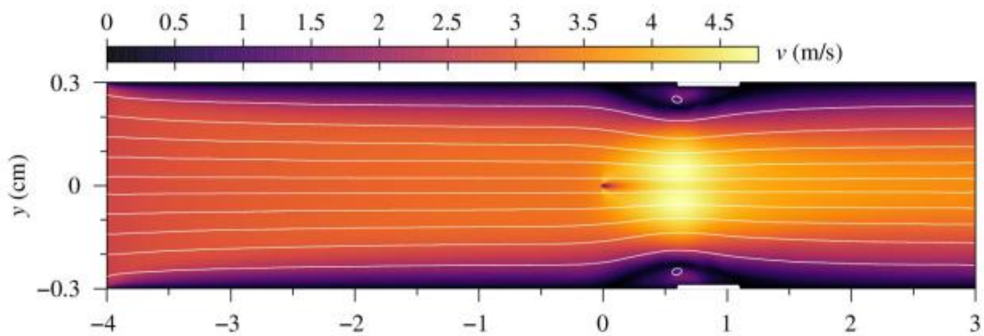

Figure III.15. 2D-spatial distribution of the velocity magnitude and their corresponding streamlines inside the improved EHD blower for an applied voltage $\phi = +10\ kV$ and corona wires of radius $r_0 = 12.5\ \mu m$.

Although the improved EHD blower's electrode arrangement offers advantages such as simpler construction and superior heat transfer from the walls to the fluid, it is important to determine whether these benefits come at the expense of higher energy consumption. To address this question, Figure III.17 presents the averaged outlet velocity as a function of electrical power. This figure directly compares the numerical simulation results for the new electrode configuration with the experimental measurements conducted by Jewell-Larsen et al. [3], which pertain to a single corona wire.

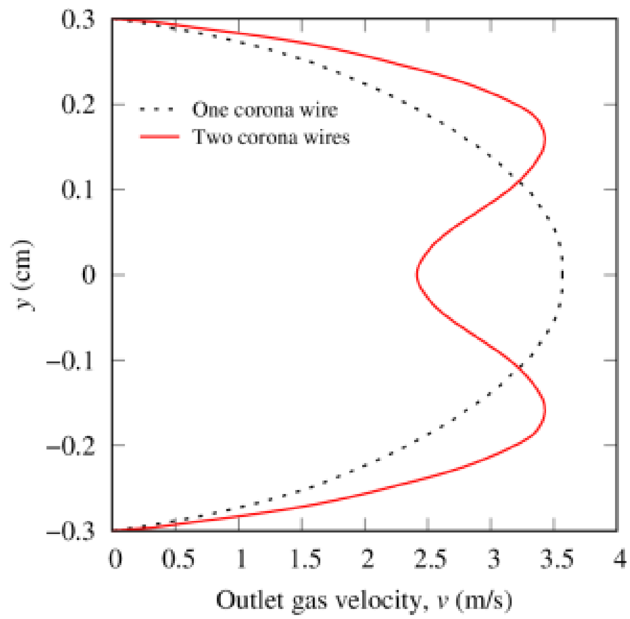

Figure III.16. Spatial distribution of the velocity magnitude at the exit of the EHD blower using an electrode configuration with a single central corona wire (dashed line) and two corona wires half embedded in the dielectric walls (solid line). for an applied voltage $\phi = +10\ kV$ and corona wires of radius $r_0 = 12.5\ \mu m$.

As shown, for the same electrical power, the outlet velocity is slightly higher when using the modified EHD blower (with two corona wires), particularly at higher electrical power levels. Therefore, the proposed electrode arrangement not only simplifies construction and improves heat transfer but also demonstrates better energy efficiency.

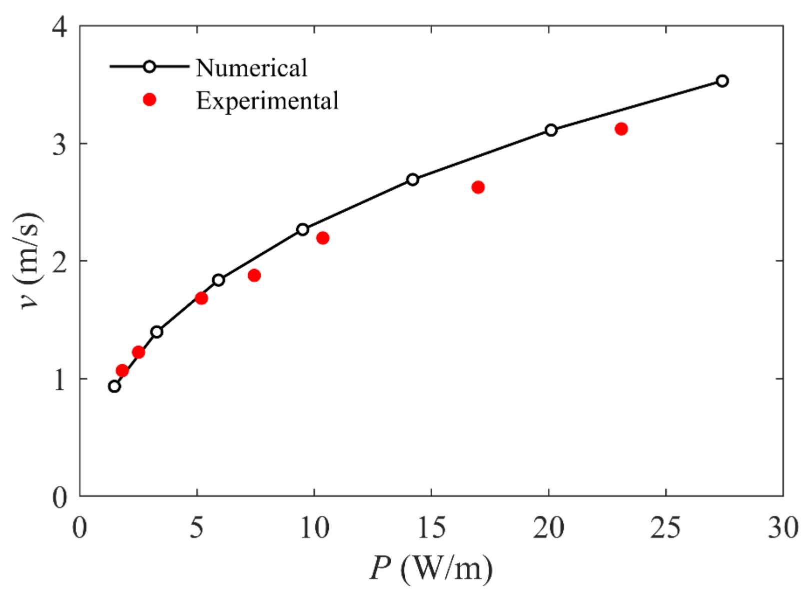

Figure III.17. Average velocity at the outlet of the duct as a function of the electric power per unit of length of corona wire according to the numerical simulation and its comparison with experiments. The experimental points (black circles) correspond to the measurements of Jewell-Larsen et al [3] using a single corona wire.

III.4 Conclusion

The comprehensive evaluation of the numerical modeling presented in this study has confirmed its accuracy and reliability in predicting both electrical and electrohydrodynamic (EHD) characteristics of corona discharges. By comparing the numerical model's predictions with extensively reported experimental measurements, we have demonstrated that the model accurately replicates the current-voltage characteristics and spatial distribution of current intensity on the cathode. This electrical validation ensures the model's robustness in simulating the behavior of corona discharges, which is critical for applications in air purification, electrostatic precipitation, and surface treatment.

The electrohydrodynamic validation has also shown that the model effectively describes the ionic wind generated by the corona discharge. The numerical model's predictions of ionic wind characteristics, such as gas velocity distribution, closely match the experimental data, affirming its practical applicability in designing cooling systems and EHD pumps. This capability is especially relevant for applications requiring efficient cooling, as the EHD air pumps offer superior heat transfer performance compared to conventional rotary fans.

Furthermore, the study introduced an improved electrode configuration for EHD air movers, demonstrating significant advantages over the traditional design. The new configuration, featuring two corona wires embedded in dielectric walls, simplifies construction and enhances heat transfer by accelerating the fluid near the walls. The numerical simulations revealed that this design not only improves the velocity distribution and eliminates recirculating eddies but also offers better energy efficiency compared to the single corona wire configuration.

In conclusion, the validated numerical model provides a powerful tool for optimizing EHD pump designs and exploring their potential applications in various fields. The improved electrode configuration presents a promising approach for enhancing the performance and energy efficiency of EHD air movers, making them a viable solution for the cooling challenges posed by the miniaturization of electronic components. Future work could further refine these designs and investigate their practical implementation in microfluidics, HVAC systems, and electronic cooling applications.

Reference

[1] T. Yamamoto and H. R. Velkoff, "Electrohydrodynamics in an electrostatic precipitator," Journal of Fluid Mechanics, vol. 108, pp. 1–18, Jul. 1981, doi: 10.1017/S002211208100195X.

[2] I. A. Elagin, V. V. Yakovlev, I. A. Ashikhmin, and Yu. K. Stishkov, "Experimental investigation of cooling of a plate by ionic wind from a corona-forming wire electrode," Tech. Phys., vol. 61, no. 8, pp. 1214–1219, Aug. 2016, doi: 10.1134/S1063784216080077.

[3] N. E. Jewell-Larsen, G. G. Joseph, and K. A. Honer, "Scaling Laws for Electrohydrodynamic Air Movers," presented at the ASME/JSME 2011 8th Thermal Engineering Joint Conference, American Society of Mechanical Engineers Digital Collection, Mar. 2011. doi: 10.1115/AJTEC2011-44626.

[4] R. S. Sigmond, "The unipolar corona space charge flow problem," Journal of Electrostatics, vol. 18, no. 3, pp. 249–272, Oct. 1986, doi: 10.1016/0304-3886(86)90021-5.

[5] P. Cooperman, "A theory for space-charge-limited currents with application to electrical precipitation," Transactions of the American Institute of Electrical Engineers, Part I: Communication and Electronics, vol. 79, no. 1, pp. 47–50, Mar. 1960, doi: 10.1109/TCE.1960.6368541.

[6] H. Ziedan, J. Tlustý, A. Mizuno, A. Sayed, and A. Ahmed, "Corona Current-Voltage Characteristics in Wire-Duct Electrostatic Precipitators 'Theory versus Experiment,'" 2010.

[7] "OpenFOAM." Available: https://www.openfoam.com/

[8] A. A. Ramadhan, N. Kapur, J. L. Summers, and H. M. Thompson, "Numerical development of EHD cooling systems for laptop applications," Applied Thermal Engineering, vol. 139, pp. 144–156, Jul. 2018, doi: 10.1016/j.applthermaleng.2018.04.119.

[9] M. Kawasaki and T. Adachi, "Mechanism and preventive method of self-excited vibration of corona wire in an electrostatic precipitator," Journal of Electrostatics, vol. 36, no. 3, pp. 235–252, Jan. 1996, doi: 10.1016/0304-3886(95)00047-X.

CHAPTER IV : Impact of Electrode Wire Interaction on EHD Flow generated in Two-Wire-to-Plate positive Corona discharge

The present study conducts a numerical investigation of the shielding effect between adjacent corona discharge electrodes in two-wire-to-plate corona devices. The primary focus of the study is to analyze the impact of mutual electrostatic interaction or shielding effect between two high-voltage wires on the electrohydrodynamic (EHD) force's direction and magnitude, as well as the overall structure of the EHD flow. Moreover, the shielding effect is closely related to the wire-plate electrode space and wire radius. The aim of modeling investigation is to highlight the importance of considering the shielding effect in designing and optimizing electrostatic precipitators and other corona devices that rely on the EHD flow.

IV.1 Introduction

In the context of enhancing devices that use electric corona discharge, researchers experiment with multielectrode configurations and use various methods for theoretical research. Findings reveal the electric field's dependence on the electrode system, encompassing studies like bacteria chelation in water [1], airflow effects in "multielectrode" corona discharge [2], enhanced drying [3], and ozone generation in "multipoint" electrode corona discharge [4] and more.

Each industrial application requires a specific design of corona discharge electrodes. However, wire electrodes are the most widely used due to their simplicity and low cost. When using a "multiwire" electrode configuration for corona discharge, it is crucial to consider the distance between the wires. When the interwire distance is large enough, the mutual electrostatic interaction between the wires, referred to as the shielding effect, becomes negligible [5, 6]. However, the shielding effect becomes significant when the distance between wires is sufficiently small. The electric field of each stressed electrode (wire) is influenced by the field of the other nearby electrode (i.e., neighboring stressed wire). The shielding effect, which results from the interaction of electric field lines when stressed wires are sufficiently close, was reported by Arif et al. [7] in a numerical study of multielectrode electrostatic precipitators and by Chibane et al. [8] in an experimental investigation concerning the loading of polypropylene films using a multiwire coil electrode configuration. In another numerical study, Marciulionis and Zebrauskas [9] reported a reduction in the space charge density as the number of wires was increased.

The characteristics of a multiwire corona discharge have also been the subject of geometric [5, 8-10], electrical [5, 10-13], and parametric simulation investigations, some of which have been confirmed by experiments [7, 10-14]. Some of these investigations have revealed the influence of the shielding on specific physical characteristics [5, 12, 15], its reinforcement by increasing the number of stressed wires [9], and/or decreasing the interwire spacing [13].

To the best of our knowledge, no research has yet focused on the effect of shielding on the EHD force and the resulting 2-D distribution of EHD wind velocity. However, understanding these two crucial physical parameters is essential for controlling and optimizing devices exploiting electric wind. Our research group has recently studied the influence of shielding only on the 2-D distribution of the electric field, the space charge, and the EHD force [16]. To further investigate this phenomenon, the objective of the present study is to evaluate the physical characteristics of the electric wind generated by a system of two-wire electrodes where these two electrodes have a shielding effect on each other. These characteristics are assessed by varying the distance between the wires and other geometrical parameters in the case of a direct positive current corona discharge in dry air. Specifically, this work focuses on determining the 2-D distribution of the EHD wind velocity, force, and space charge density at each point in the wire-plate electrode space.

IV.2 Results and discussion

In this study, the investigated electrodes' arrangement includes two identical wires with a radius of r_0. These two wires are positioned above the grounded plate and connected to positive high voltage. The resulting electric wind generated by the corona discharge is confined between the lower ground plate (GP) and the upper insulating plate separated by a distance h. Each plate has a length of L. The wires are located at the center of the channel, equidistant from the two plates, and spaced apart by a distance of f. Figure IV.1 depicts a schematic representation of the corona reactor.

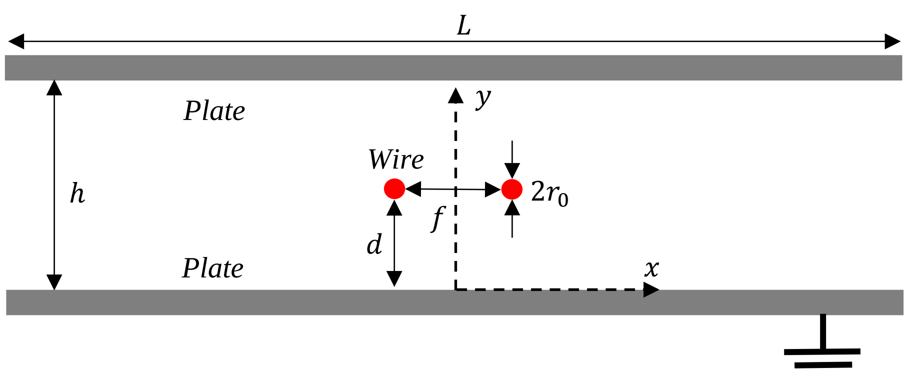

Figure IV.1. Schematic presentation of the corona reactor.

The results discussed in this section correspond to the following parameters for the corona discharge reactor: the radius of the electrode wire is $r_0 = 50$, 100, and 150 µm; the wire-plate electrode distance for each wire is $d = 0.5$, 1, and 1.5 cm; the length of the upper and lower plates is $L = 10$ cm; the distance separation between them is $h = 1.02$, 2.02, and 3.02 cm; and the separation distance between the two wires considered is $f = 0.2$, 1, and 2 cm.

IV.2.1 Electric Current

Figure IV.2 shows the characteristic current–voltage for three values of wire-to-wire separation (*f* = 2, 1, and 0.2 cm). For a given value of the applied voltage, this figure reveals a decrease in electric current as the separation distance *f* is reduced. For example, at 11 kV, the electric current decreases by about 15% when the distance *f* changes from 2 to 1 cm and 49% when the distance *f* changes from 1 to 0.2 cm. For any given value of the applied voltage, the current is higher in the one-wire configuration than the mean value for the two-wire configuration, which confirms the mutual effect between the two wires. As discussed earlier, the strength of the mutual interaction or shielding between the two wires is related to the wire-to-wire distance. Indeed, the space charge tends to diminish more and more on the surface of each wire, and the field lines become more compact over the wire surface when the distance f decreases further. Experimental measurements have confirmed this attenuation of the electric current, which is caused by the interaction of the electric field lines created by adjacent discharge wires, i.e., shielding [17, 18].

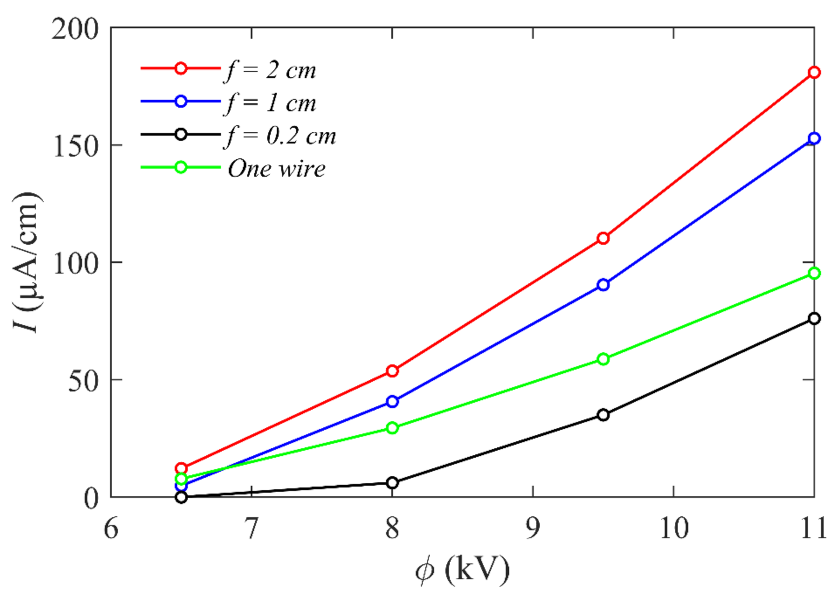

Figure IV.2. Effect of wire-to-wire separation on $I-\phi$ characteristics for three separation distances between the wires ($f\ = 0.2, 1,$ and 2 cm) and for wires' radius, $r_0\ = 100$ µm, and wire-plate electrode distance, $d\ = 0.5$ cm.

To validate our calculations, the current density distribution at the grounded plate is compared with the experimental measurements [8] shown in Figure IV.3 for one and two wires with a radius of 125 µm, a wire-plate electrode spacing of 8 cm, and an applied voltage of 14 kV. It is clear from this comparison that the results produced by the numerical model were accurate and in good agreement with the experimental measurements. Thus, the presented numerical model was used to investigate the effect of various corona discharge parameters on the degree of shielding and the induced EHD gas flow.

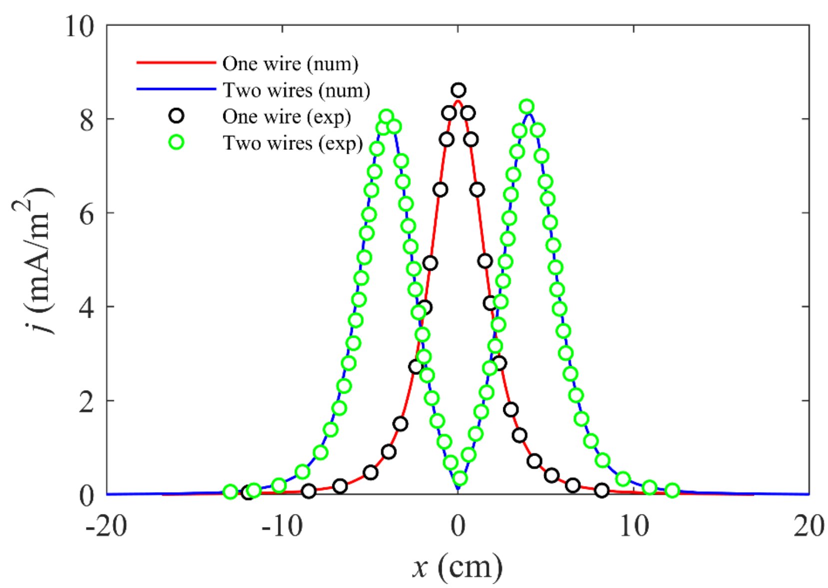

Figure IV.3. Electric current density distribution at the grounded plate for wires' radius, $r_0 = 125\ \mu m$; wire-plate electrode distance, $d = 3\ cm$; interwire distance, $f = 8\ cm$; and high voltage, $\phi = 14\ kV$

The mutual interaction between two wires when they are closer to each other results in a reduction in the geometric electric field, as illustrated in Figure IV.4, where the geometric electric field is plotted along an electric field line for three separation distances between the wires ($f = 0.2, 1,$ and 2 cm). In Figure IV.4, the distance l_a presents the arc length of the electric field line. The three graphs corresponding to the separation distances all start at the same point on the wire surface. Indeed, a decrease in the geometric electric field leads to a reduction in the space charge density generated by the corona discharge and, consequently, a reduction in the electric current.

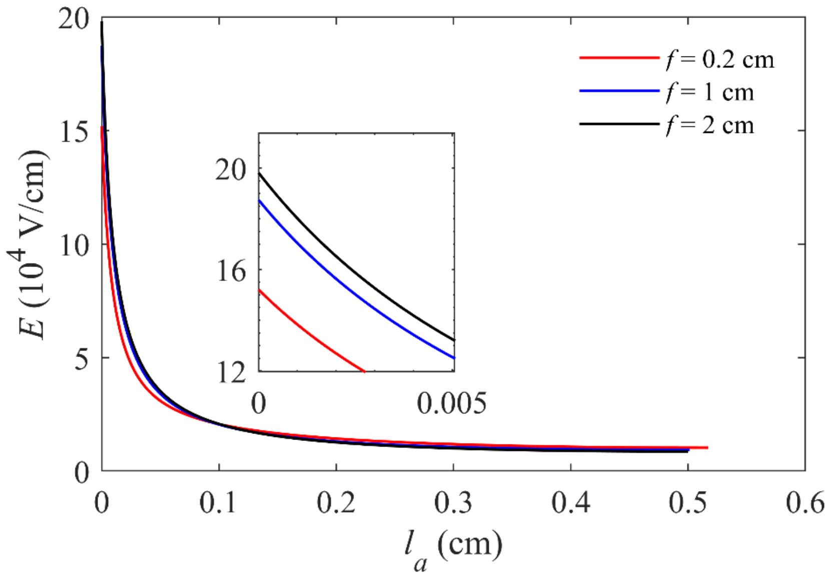

Figure IV.4. Geometric electric field strength along the electric field line defined by the starting point on the surface of the wire ($x = (f/2) + r_0, y = d$) for three separation distances between the wires ($f = 0.2, 1$, and 2 cm) and for wires' radius, $r_0 = 100$ μm; wire-plate electrode distance, $d = 0.5$ cm; and high voltage, $\phi = 9.5$ kV

In Figure IV.5, the charge density has two separate distributions, one for each wire. It is clear that due to the shielding effect, the space charge density declines when the separation distance f is reduced. For example, the maximum charge density on each wire surface is approximately $5.14 \times 10^{-3}, 10.1 \times 10^{-3}$, and 12.1×10^{-3} C/cm^3 when the separation distance f takes the values of $0.2, 1$, and 2 cm, respectively. Between the two wires, in a narrow region around the y-axis, the values of the space charge density are practically negligible. Marciulionis and Zebrauskas [9] have also reported this shielding effect when the number of wires increases. Indeed, the shielding effect alters the spatial distribution of the charge density. For example, in the case of wires separated by distances f = 1 and f = 2 cm [Figure IV.5 (b) and (c)], each charge density distribution is nearly symmetrical with respect to a straight line connecting the wire and the GP, while in the case of f = 0.2 cm this symmetry vanishes. Finally, it is important to note that when the distance between the wires increases, the interaction between them weakens, and the charge density distributions become more similar to that of a single wire [see Figure IV.5 (d)]. This is because the electric field created by each wire has a less impact on the electric field of the other wire as the distance between them increases. As a result, the shielding effect becomes less significant, and the charge density distributions become more symmetric with respect to the wire and GP axis.

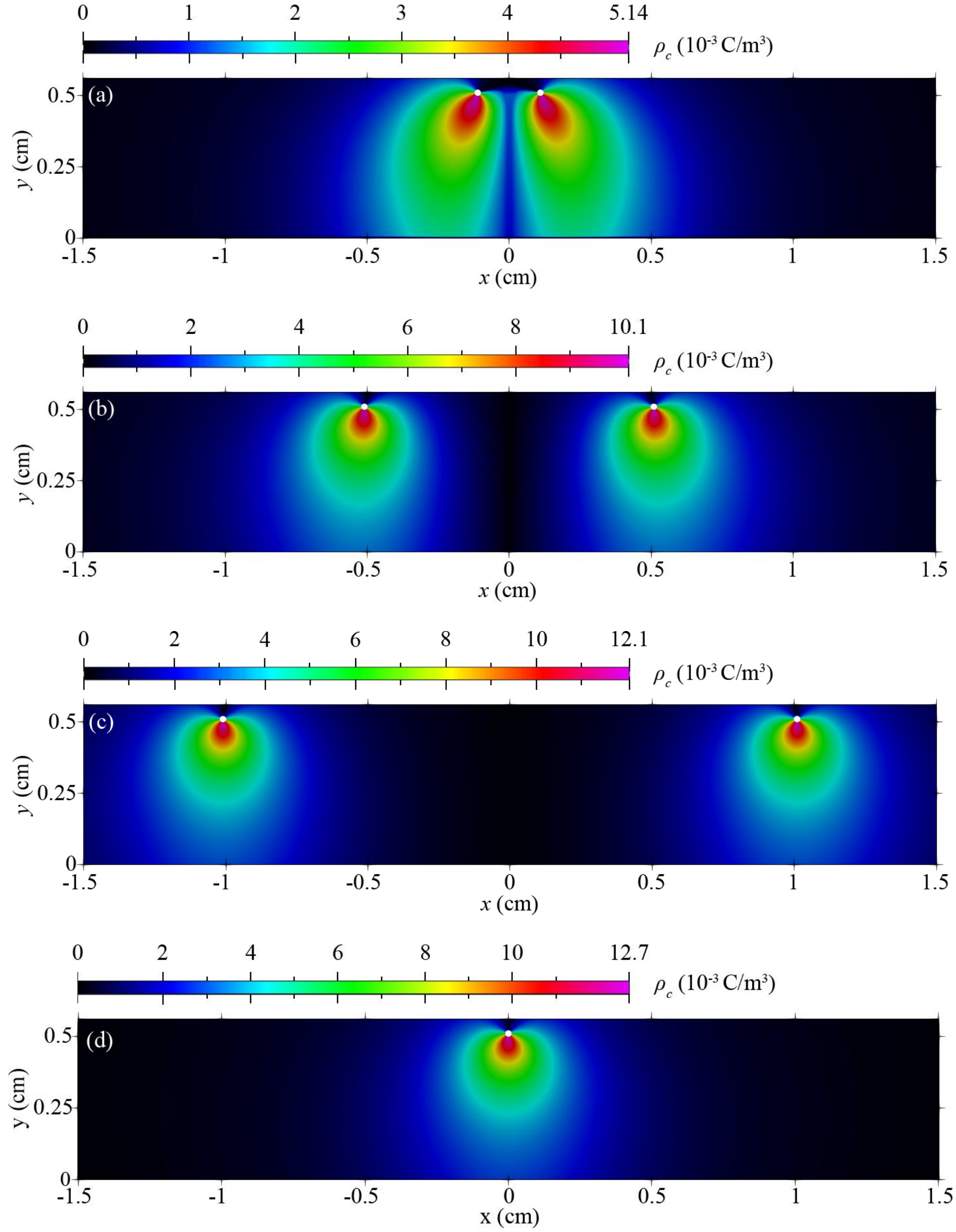

Figure IV.5. Two-dimensional spatial distribution of the space charge density for two wires and for: wires' radius, $r_0 = 100$ μm; wire-plate electrode distance, $d = 0.5$ cm; high voltage, $\phi = 11$ kV; and the distance f between the two wires is (a) 0.2, (b) 1, (c) 2 cm and (d) corresponds only to one wire.

IV.2.2 EHD Force

The EHD force generated by the corona discharge in each point of space is related to the distribution of space charge density and the strength and direction of the electric field, as indicated by relation (II.51). As can be seen, the direction of the EHD force is the same as the electric field at each point in the discharge space. However, the average direction of the EHD force is not collinear with the average direction of the electric field in all the cases. For example, in a simple electrode configuration, such as a wire-to-plate arrangement, the average direction of the EHD force is collinear with the average direction of the electric field. However, in the case of two closely spaced wires, the average direction of the EHD force for each wire is not collinear with the corresponding average direction of the electric field. As a result, the direction of the EHD flow, which is related to the average direction of the EHD force, will depend on the mutual interaction between the wires. Overall, the effect of shielding on the direction of the EHD force is twofold. First, it modifies the electric field lines, which alters the direction of the EHD force. Second, it modifies the space charge density, which impacts the global direction of the EHD force. To the best of our knowledge, this aspect regarding the effect of shielding on the direction of the EHD flow has not yet been highlighted.

In this context, Figure IV.6 shows the spatial distributions of the EHD force, including the force lines, corresponding to the separation distances f between the two wires: 0.2, 1, and 2 cm. For these three cases, the average EHD force direction for each wire is represented by an oblique line (the left line corresponds to the left wire, while the right line corresponds to the right wire). Specifically, the EHD force magnitude lines spread from each wire toward the ground plate (GP) and the upper plate along the oblique lines.

Starting at the wire surface and moving away from each side along the oblique line, the EHD force magnitude lines are getting further away. For all three distances f, the EHD force magnitude is maximal at two points on the surface of each wire, with values of approximately $6.1 \times 10^{-2}, 12.1 \times 10^{-2}$, and 14.4×10^{-2} $\mathrm{N/cm^3}$, when f takes the values $0.2, 1$, and 2 cm, respectively, as shown in Figure IV.6. Then, it starts decreasing along lines 1 and 2; at a distance of about $250\ \mu\mathrm{m}$ from each wire, the EHD force is about $1.91 \times 10^{-2}, 3.60 \times 10^{-2}$, and $4.25 \times 10^{-2}\ \mathrm{N/cm^3}$, respectively. Further down, at the surface of the GP, it becomes negligible. Regarding the case where two wires are separated by a distance of $f = 0.2$ cm (as shown in Figure IV.6 (a)), it is worth noting that the electrostatic interaction between the wires is significant. Consequently, this interaction has a noteworthy impact on the magnitude of the EHD force.

In terms of the effective global direction of the EHD force, for a wire-to-wire distance of $f = 1$ cm (Figure IV.6 (b)), the oblique lines (lines 1 and 2), which indicate the EHD force direction, are almost vertical, while for $f = 2$ cm, they became completely vertical because, at this distance, the shielding effect nearly disappears. It should be noted that as the distance between the two wires increases, the values of the EHD force also increase as a consequence of shielding disappearance.

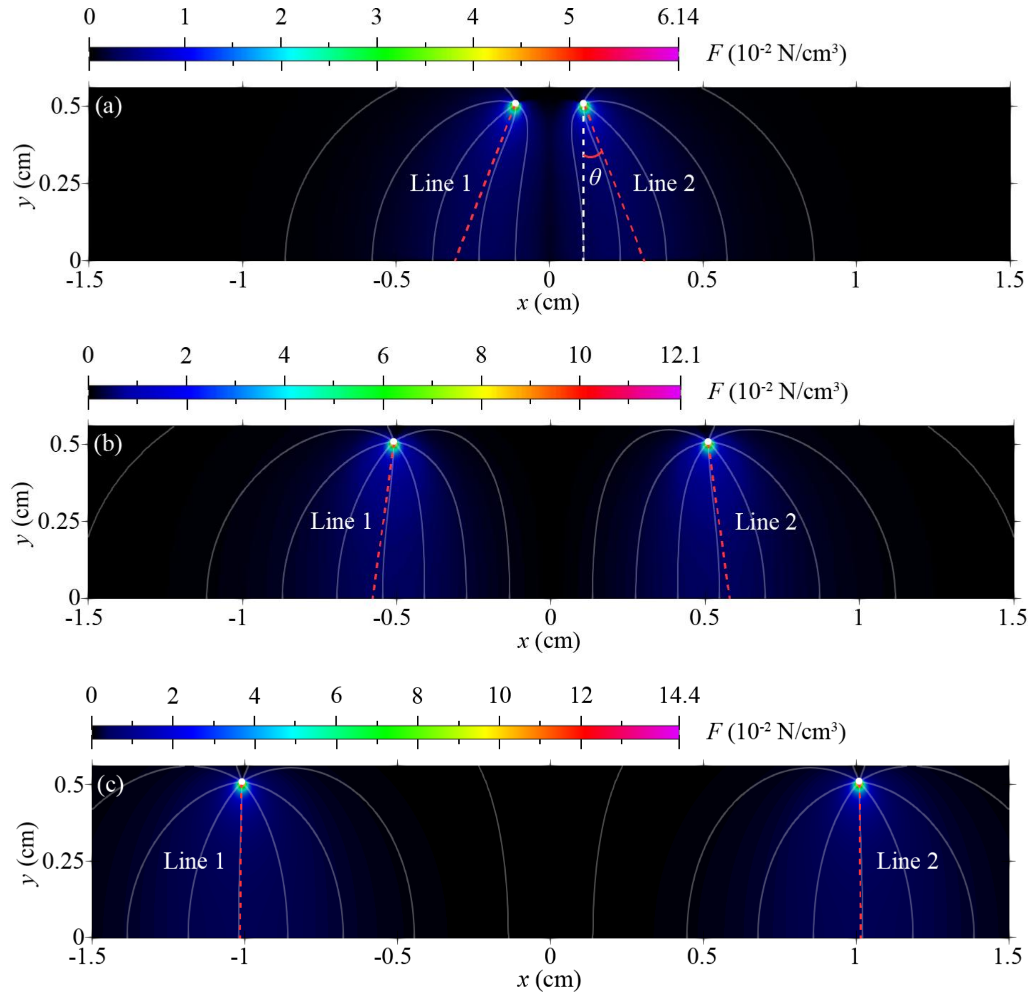

Figure IV.6. Two-dimensional spatial distribution of the EHD force magnitude for two wires for: wires' radius, $r_0 = 100$ µ*m; wire-plate electrode distance,* $d = 0.5$ *cm; high voltage,* $\phi = 11$ *kV; and the distance* f *between the two wires is (a)* 0.2*, (b)* 1*, and (c)* 2 *cm.*

The reduction in the EHD force with decreasing wire-to wire distance due to shielding is also illustrated in Figure IV.7, where the EHD force distribution is plotted below the wire along the line $y = 0.5$ cm. It is clear from this figure that the EHD force reaches its maximum value at the points directly below the discharge wires and gradually decreases as it moves toward the midpoint between the adjacent wires.

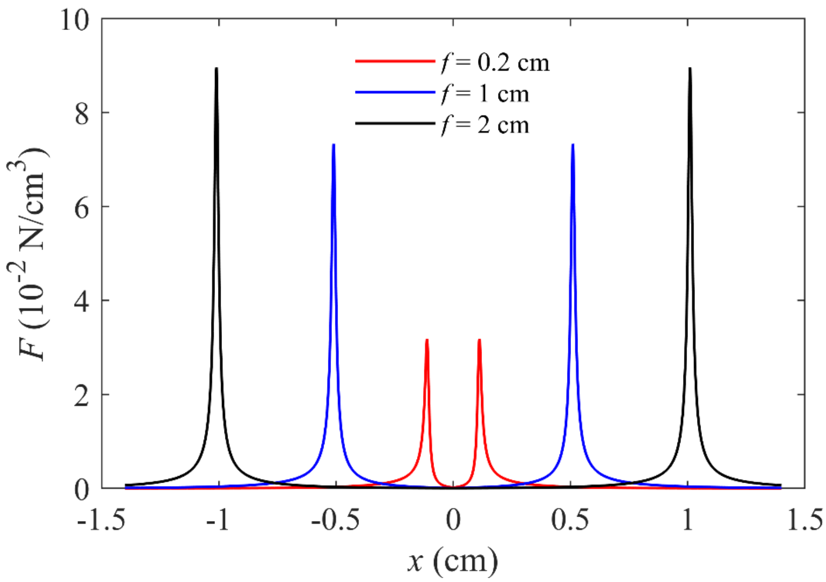

Figure IV.7. Force magnitude below the wire along the line $y = 0.5\ cm$ *for wires' radius,* $r_0 = 100\ \mu m$*; wire-plate electrode distance,* $d = 0.5\ cm$*; and high voltag* $\phi = 9.5\ Kv$.

IV.2.3 Electric Wind

Figure IV.8 (a) and (b) demonstrates the effect of the EHD force on airflow in the wire-to-plate electrode configuration, with reasonable agreement found between the results obtained from our numerical modeling and our previous model that relied on an analytical approach to calculate the EHD force [19, 20]. Indeed, the difference between the currently used model, as described in CHAPTER II, and the previous one [19] is as follows: The current model predicts the characteristic current-voltage, which facilitates the handling of complex electrode geometries, in contrast to the previous [19, 20] model, which dealt with simple electrode configurations and used the characteristic current–voltage as an input parameter. Both the figures confirm that the air moves from the wire to the GP due to the EHD force and undergoes a change in direction upon reaching the GP, resulting in the formation of two symmetrical vortices with respect to the axis $x = 0$. Since these vortices are formed due to the EHD force and the grounded plate, which plays a role as an obstacle, these vortices can be regarded as mixed vortices, which is a combination of free and forced vortices [21].

The observed agreement between our numerical model and that calculated by our previous analytical model, as demonstrated in Figure IV.8 (a) and (b), provides strong evidence for the validity of our calculations regarding the EHD force and its effect on airflow in the wire-to-plate electrode configuration. Based on these results, we can conclude that our numerical model yields highly satisfactory results and can effectively be used to investigate the shielding effect in the corona discharge.

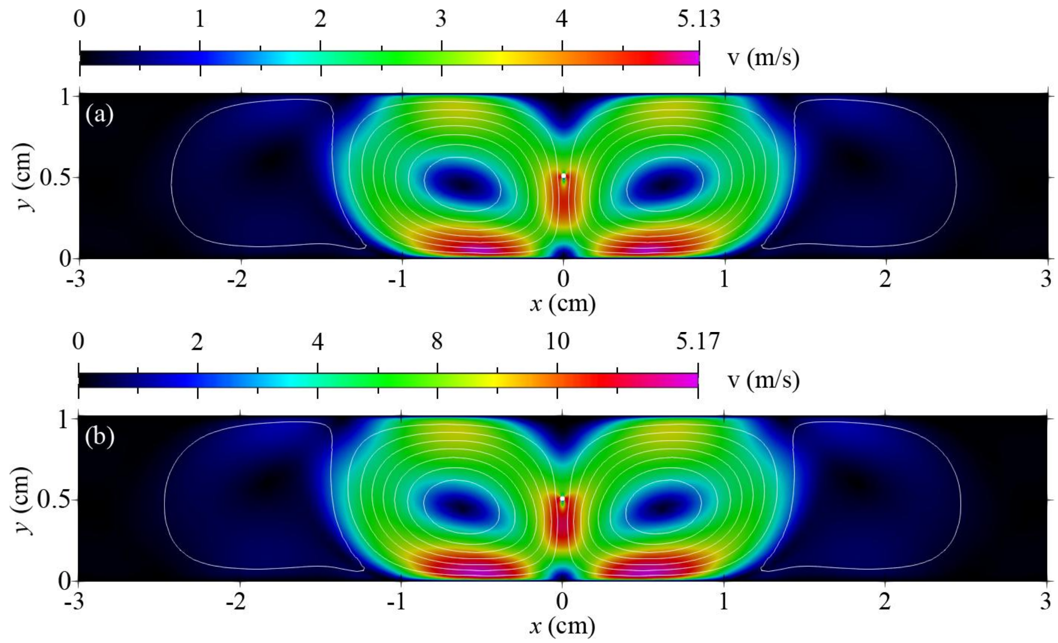

Figure IV.8. Two-dimensional spatial distribution of the magnitude of the gas velocity inside the reactor for a single wire of radius $r_0 = 100$ μm, wire-plate electrode distance $d = 0.5$ cm, and for an applied voltage $\phi = 9$ kV. (a) Calculated and (b) analytical mod models of the EHD force.

Figure IV.9 illustrates that when the value of f is set to 0.2 cm (Figure IV.9 (a)), the shielding effect is so significant that the variation in velocity magnitude primarily occurs along line 1 (on the left) at an angle of approximately 42∘ relative to the y-axis and along line 2 (on the right), which is slanted at the same angle. At a distance of approximately 0.25 cm from the wire on each of the two straight lines, the maximum velocity is approximately 1.58 m/s. Aside from the two large vortices that form, two smaller vortices develop between them, located below the two wires and near the GP. These small vortices have a maximum velocity of around 1.58 m/s.

The shielding effect is less pronounced when the distance f between the two wires is 1 cm (as shown in Figure IV.9 (b)). As a result, the angle at which the velocity flows along lines 1 and 2 becomes negative, around $-20°$. This observation is unexpected when compared with the results obtained in Figure IV.9 (a). In addition, the highest velocity, which is approximately 3.45 m/s, is located at the center of the interwire distance. This value is greater than the velocity observed in Figure IV.9 (a). Concerning the two neighboring vortices, they still occupy the interwire space; however, their deformation is less pronounced, and their size is larger when compared with Figure IV.9 (a) where $f = 0.2\ cm$. This observation may be attributed to a possible increase in the intensity of the EHD force acting between the two wires as they move apart. Finally, when the interwire distance is $f = 2$ cm (as shown in Figure IV.9 (c)), the interaction between the wires is even less pronounced than in Figure IV.9 (b). This is evident from the small angle of inclination, which is approximately 10° (for the left wire), and the maximum velocity flow of approximately 3 m/s below each wire. Based on the observations from the three cases, it can be concluded that an increase in the interwire distance f leads to a weaker interwire shielding effect. This results in a higher maximum velocity magnitude and a lower inclination of the ionic wind flow (lines 1 and 2). As mentioned earlier, the weakening of the interwire shielding effect leads to an increase in the magnitude of the EHD force, which explains the rise in gas velocity as it approaches the axis of symmetry.

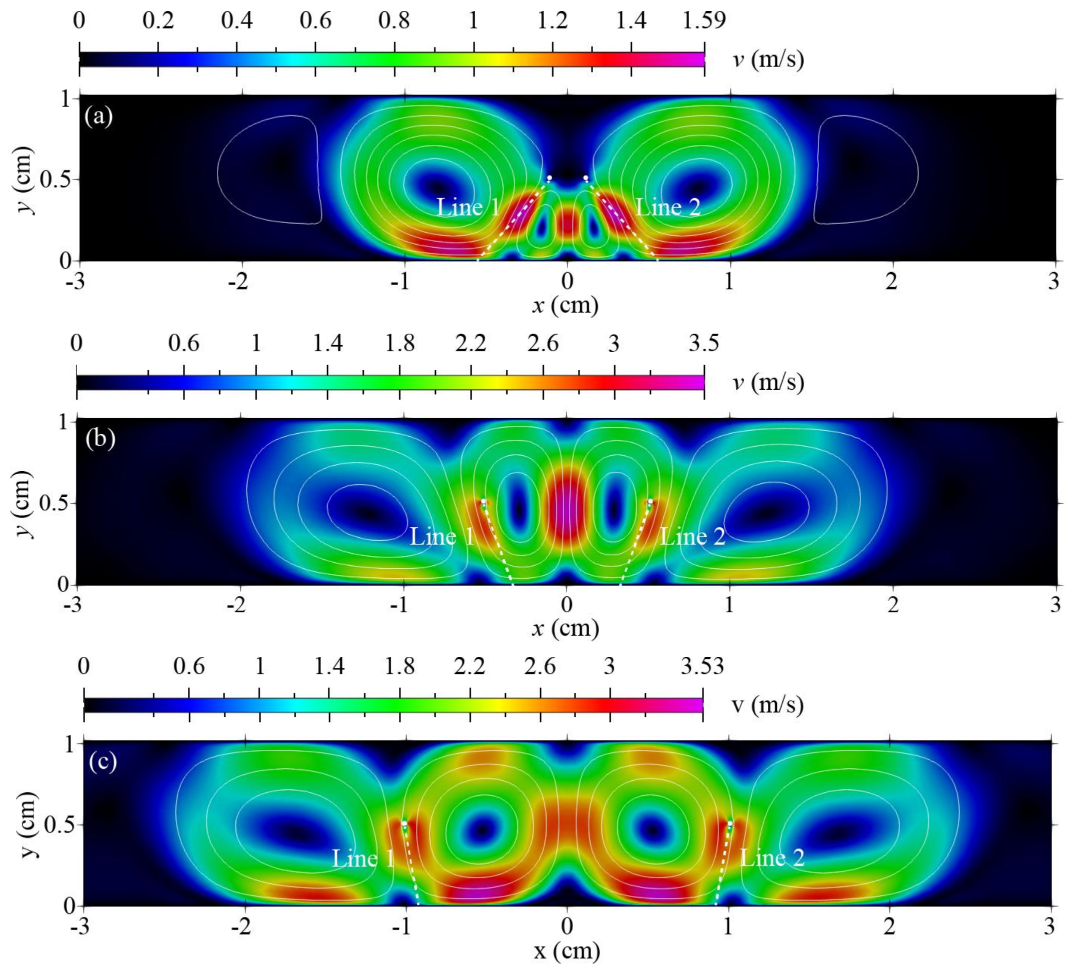

Figure IV.9. Two-dimensional spatial distribution of the magnitude of the gas velocity inside the reactor for two wires: the radius of each wire is $r_0 = 100$ μm; the wire-plate electrode distance is $d = 0.5\ cm$; the applied voltage is $\phi = 8\ kV$; and the distance between the two wires is (a) 0.2, (b) 1, and (c) 2 cm.

IV.2.4 Parametric Studies

IV.2.4.1 Effect of the Applied Voltage

In the glow regime of the corona, the magnitude of the EHD force is directly proportional to the intensity of the electric current, which, in turn, is proportional to the applied voltage. Therefore, a higher voltage would result in a larger discharge current, leading to a greater EHD force. To investigate the effect of the applied voltage on the EHD force and the induced electric wind flow, the voltage was varied while keeping the other parameters constant.

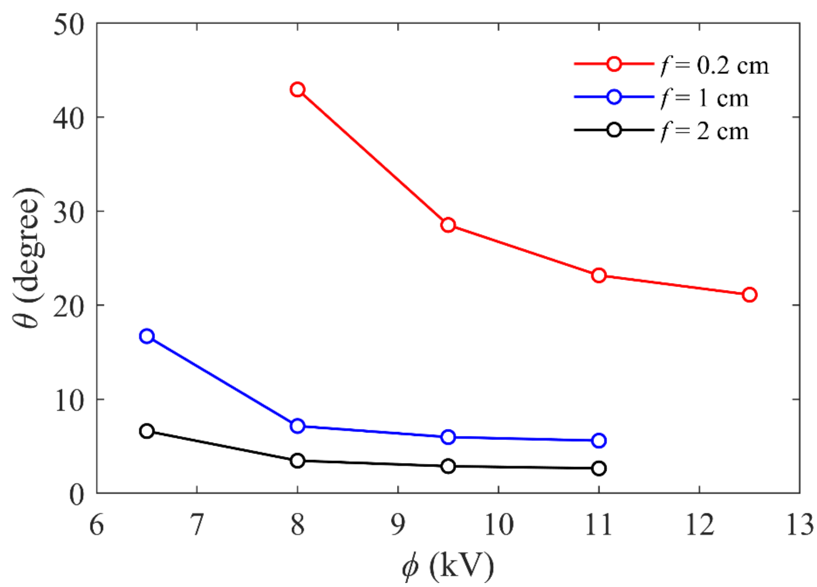

Figure IV.10. Variation in the angle θ (relative to the y-axis) that indicates the average direction of the EHD force as a function of the high voltage for interwire distance $f = 0.2, 1,$ and 2 cm; wires' radius $r_0 = 100$ µm; and wire-plate electrode distance, $d = 0.5$ cm.

Figure IV.10 illustrates how the applied voltage affects the global angle of the EHD force with respect to the y-axis. This figure demonstrates that as the interwire spacing f increases, there is a rapid variation in the angle (θ) at relatively low high-voltage levels and with relatively large angles. For example, for an applied voltage $\phi = 11$ kV, the angle θ takes the values $2.64°, 5.59°$, and $23.17°$ when f takes the values $2, 1$, and 0.2 cm, respectively. However, at higher values of the applied voltage, beyond a certain threshold, the global direction of the EHD force does not change significantly when $f > 1$ cm, although the magnitude of this EHD force increases as the voltage increases.

The effect of the applied voltage on the spatial distribution of EHD force is illustrated in Figure IV.11 which indicates that the magnitude of the EHD forces below the wires along the line $y = 0.5$ cm axis decreases as the applied voltage diminishes. As an example, the maximum EHD force is approximately $0.098\ \mathrm{N/cm^3}$ at an applied voltage of 12.5 kV, while it decreases to $0.06\ \mathrm{N/cm^3}$ at $\phi = 11.0$ kV and further drops to $0.025\ \mathrm{N/cm^3}$ at $\phi = 9.50$ kV.

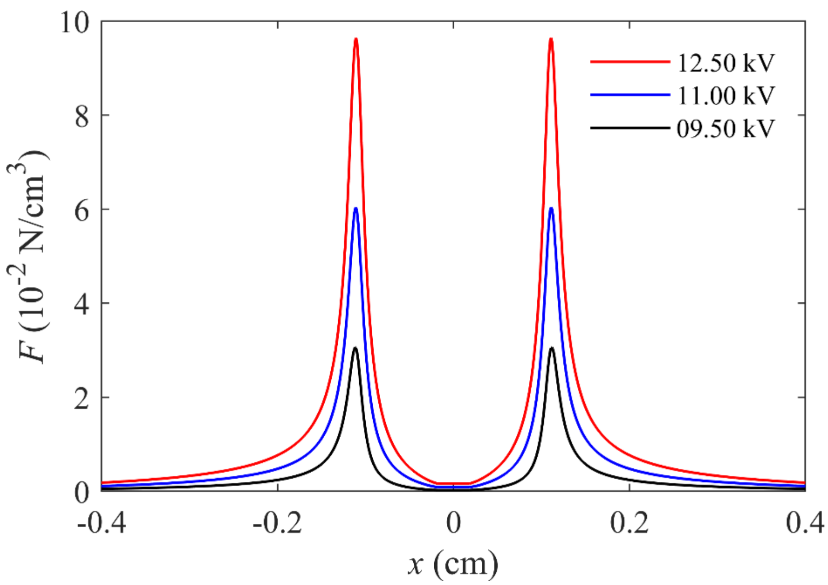

Figure IV.11. EHD force magnitude distribution below the wire along the line $y = 0.5$ cm for: inter-wire distance $f = 0.2$ cm; wires radius $r_0 = 100$ µm; inter-electrode distance, $d = 0.5$ cm; and high voltage $\phi = 9.5, 11$ and 12.50 kV .

To explain why the angle of the average direction of the EHD force is high at small values of the applied voltage and starts decreasing when the applied voltage increases, the density of space charge is plotted along two chosen electric field lines in Figure IV.12. For an applied voltage of 8 kV, the distribution of the space charge density is the same for the two lines; in fact, these two lines are considered to be symmetric with respect to the axis ($x = f/2 + r_0$): these two lines are defined by the two symmetrical starting points on the surface of the wire which are ($x = f/2, y = d + r_0$) and ($x = f/2 + 2r_0, y = d + r_0$), respectively. However, when the voltage is increased further, the charge density on the left (right) of the right wire (left wire) becomes more significant than that on the right (left) of the right wire (of the left wire). This means that the global direction of the EHD force deviates toward the left (right) for the right wire (left wire) since the EHD force is the product of the charge density and the electric field. It is important to note that the orientation of the electric field remains constant at each point in space (or locally constant) regardless of the applied voltage. Consequently, the direction of the EHD force also remains constant at each point, contrary to the global (or average) direction of the EHD force, which undergoes variation due to alterations in the distribution of charge density, as explained above.

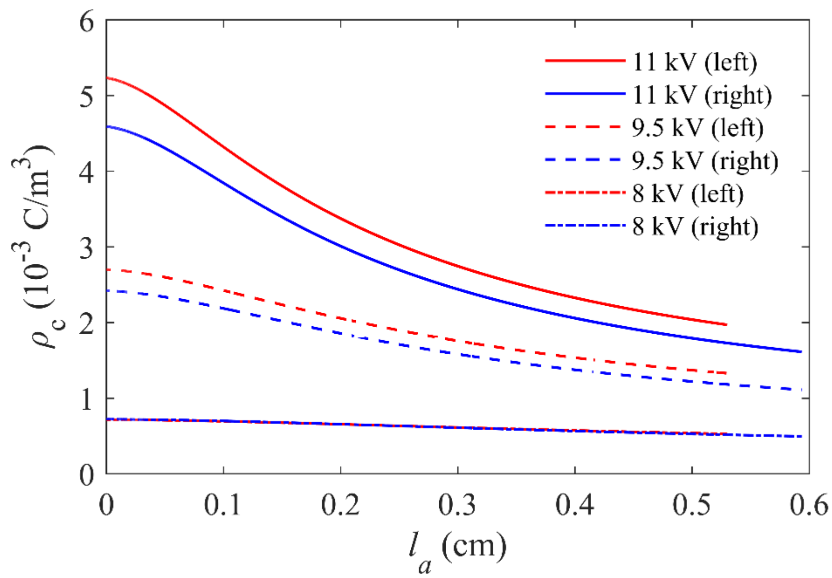

Figure IV.12. Density of space charge along two electric field lines defined by two symmetrical starting points on the surface of the wire which ($x = f/2, y = d + r_0$) *and* ($x = f/2 + 2r_0, y = d + r_0$), *respectively, for: interwire distance* $f = 0.2$ *cm; wires' radius* $r_0 = 100$ μm*; wire-plate electrode distance,* $d = 0.5$ *cm; and high voltage* $\phi = 8.0, 9.5,$ *and* 11.0 *kV*.

Figure IV.13 shows the 2-D spatial distribution of the wind velocity magnitude in the case of two wires distant with $f = 0.2$ cm and for three applied voltage values (Figure IV.13 (a), $\phi = 8$ kV; Figure IV.13 (b), $\phi = 8,5$ kV; and Figure IV.13 (c), $\phi = 11$ kV). A comparison of the three cases confirms that the shielding effect is more significant when the applied voltage is higher.

This effect is primarily manifested in two ways: an increased inclination of the electric wind direction and a shift in the position of the maximum velocity v_{max}, which undergoes a notable increase in magnitude from 1.58 m/s (at 8 kV) to 5.5 m/s (at 11 kV). In addition, the two vortices are expanded toward the left and right boundaries, with a length of approximately $x = 1.64$ cm. Finally, it is important to note that the structure of the wind velocity (the 2-D spatial distribution) undergoes a complete transformation at higher applied voltages ($\phi = 11$ kV). Specifically, at this voltage level, the two nearest vortices between the two wires almost disappear entirely. Instead, the other two vortices become adjacent, occupying a large portion of the interwire space and expanding slightly toward the channel ends (Figure IV.13 (c)).

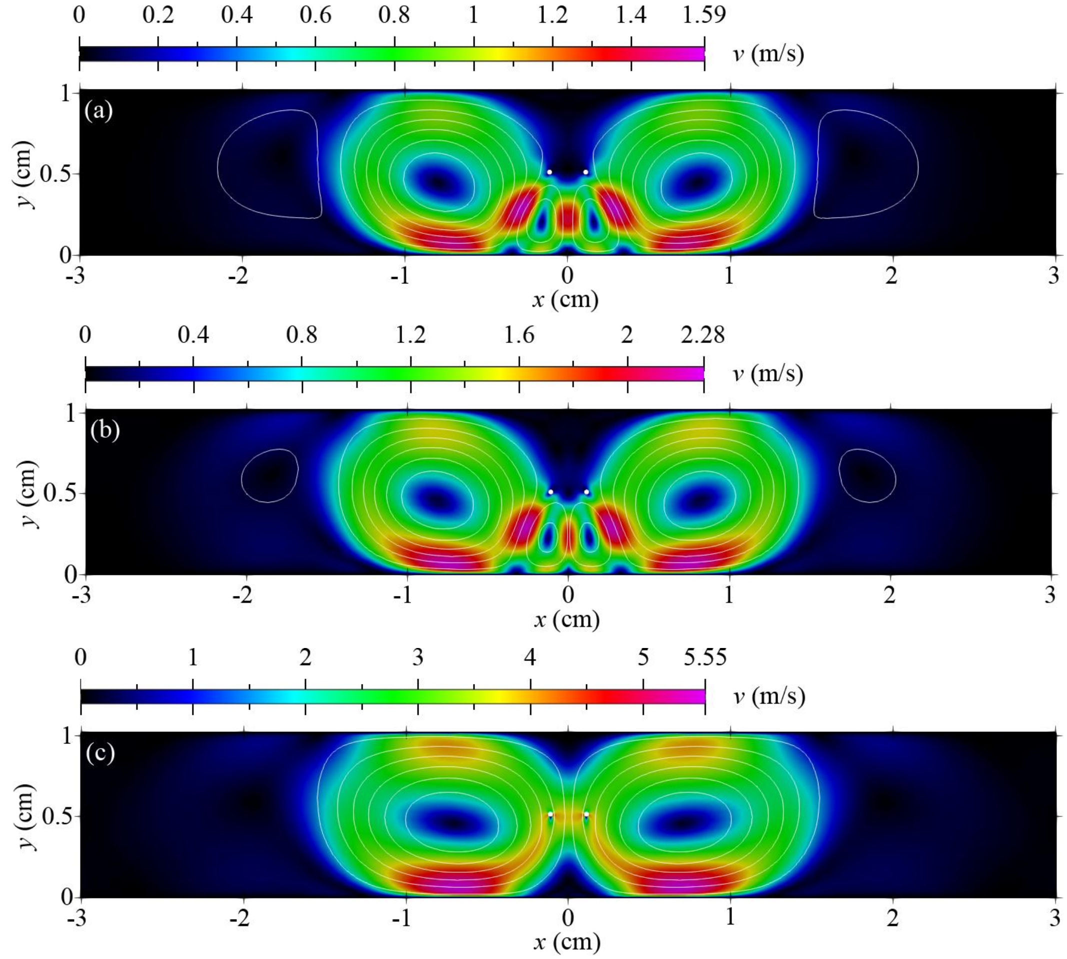

Figure IV.13. Two-dimensional spatial distribution of gas velocity magnitude corresponding to two stressed wires separated by distance $f = 0.2\ cm$, for a wire radius $r_0 = 100\ \mu m$, a wire-plate electrode distance $d = 0.5\ cm$, and a high voltage (a) $\phi = 8$, (b) $\phi = 8.5$, and (c) $\phi = 11\ kV$.

The disappearance of the two small vortices, which were reduced in volume due to the reduction in the distance f (as shown in Figure IV.13 (b)), can be attributed to a significant increase in the size and strength of the two vortices that are located outside the interwire space. As a result, the two small vortices are compressed against the plate, minimized, and ultimately eliminated when the applied voltage is sufficiently high. On the other hand, when considering a small interwire distance of $f = 0.2$ cm and an applied voltage higher than 9 kV, the direction of the electric wind underneath the wires does not exhibit a significant change. However, the maximum velocity v_{max} of the electric wind increases considerably closer to the grounded plate.

It can be concluded that when the applied voltage is sufficiently high, and the interwire distance is small, the behavior of the two wires is analogous to that of a single wire, as only two vortices are formed, similar to the case of a single wire. It should also be noted that for small interwire spacing, the overall wind velocity profile undergoes a complete change when transitioning from low to high applied voltage levels.

IV.2.4.2 Effect of the Wire-Plate Electrode Distance

The influence of the wire-plate electrode distance on the EHD force and on the wind velocity profile is shown in Figure IV.14 and Figure IV.15 for an interwire distance of f = 0.2 cm and three different wire-plate electrode distances of d = 0.5, 1.0, and 1.5 cm.

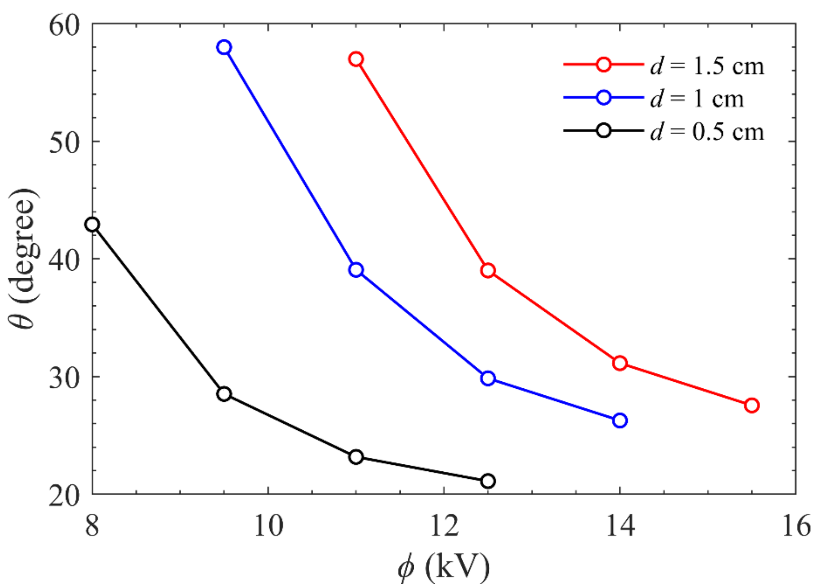

Figure IV.14. Variation in the angle θ that indicates the average direction of the EHD force as a function of the high voltage for interwire distance f = 0.2 cm; wires' radius r_0 = 100 μm*; and wire-plate electrode distance, d = 0.5, 1, and 1.5 cm.*

According to the results shown in Figure IV.14, for a fixed applied voltage level, the angle representing the average of the EHD force direction decreases as the wire-plate electrode distance d is reduced. For instance, at a high voltage of 11 kV, the angle θ assumes values of 56.98°, 39.06°, and 23.17° for wire-plate electrode distances of 1.5, 1.0, and 0.5 cm, respectively.

Nonetheless, the effect of reducing the angle θ as d decreases becomes less pronounced at higher applied voltages, eventually becoming negligible. This suggests that beyond a certain threshold of the applied voltage, the direction of the EHD force is only minimally inclined with respect to the $x = 0$ axis, even as the magnitude of the EHD force continues to increase with the applied voltage.

Figure IV.15 illustrates the spatial distribution of the magnitude of the EHD force below the wire along the line $y = d$. It is evident from the figure that increasing the inter-electrode distance from 0.5 to 1.0 cm and subsequently to 1.5 cm significantly reduces the magnitude of the EHD force. For an example, for an applied voltage of $11kV$ and inter-electrode distances of 0.5, 1, and $1.5cm$, the maximum magnitude of the EHD force (F_{max}) is 6.19×10^{-2}, 0.71×10^{-2}, and $0.15 \times 10^{-2}\ \mathrm{N/cm^3}$, respectively. Figure IV.15 also shows that the magnitude distribution of the EHD force is not symmetric versus each vertical axis passing by the center of each wire, due to the shielding effect. Specifically, the magnitude of the EHD force is lower in the space between the two wires than in the space outside the discharge wires. This effect becomes more apparent as the inter-electrode distance decreases.

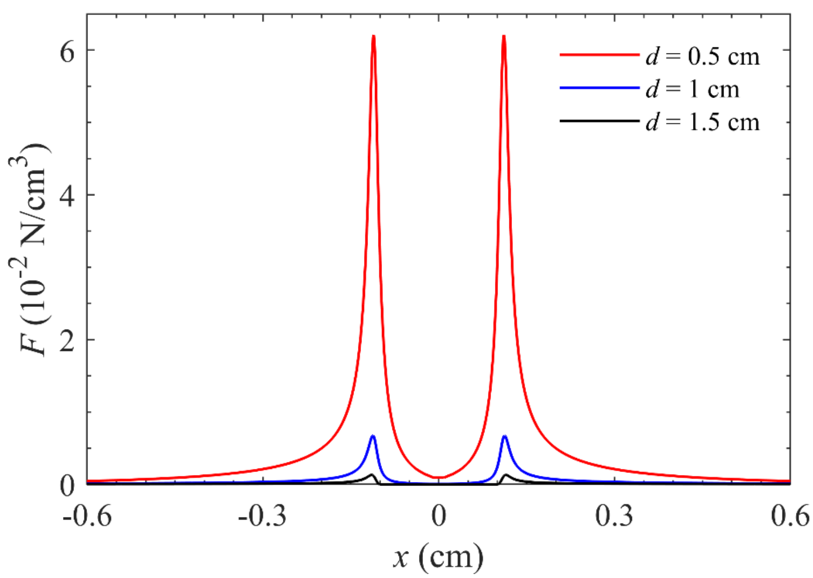

Figure IV.15. EHD force magnitude distribution below the wire along the line y = d for: inter-wire distance f = 0.2 cm; wires radius$r_0 = 100$ μm; interelectrode distance, d = 0.5, 1 and 1.5 cm; and high voltage ϕ = 11 kV.

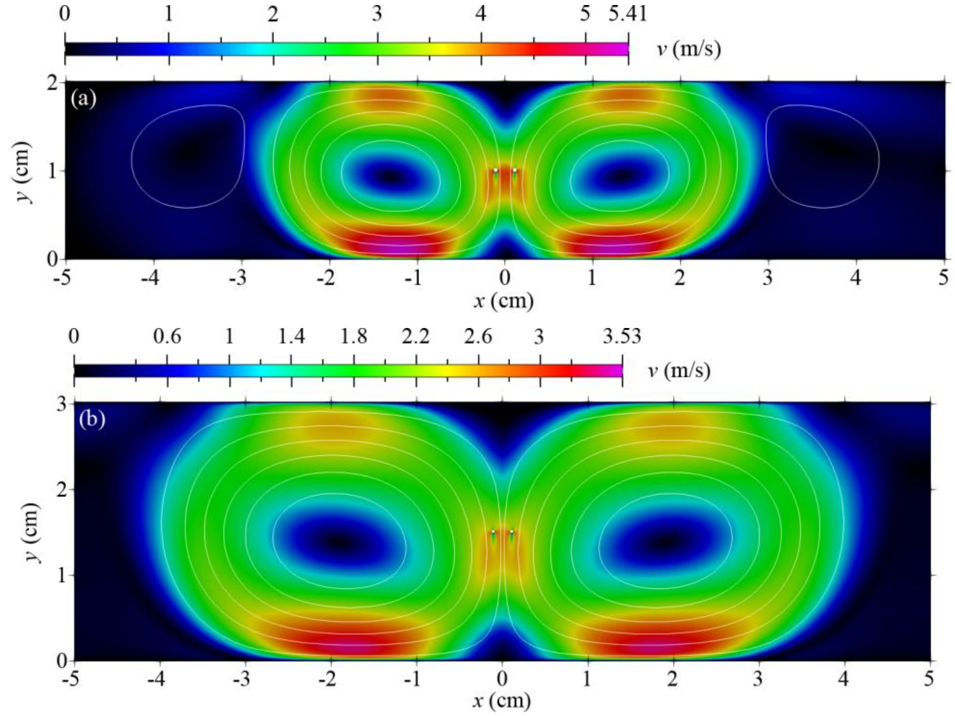

Figure IV.16. Two-dimensional spatial distribution of gas velocity magnitude corresponding to two stressed wires separated by distance f = 0.2 cm; for a wire radius $r_0 = 100$ μm; an interelectrode distance (a) d = 1.0 cm and (b) d = 1.5 cm; and a high voltage $\phi = 15.5\ kV$.

The 2-D spatial distribution of the wind velocity for two wires with an interwire distance of $f = 0.2$ cm, an applied voltage of $\phi = 15.5\ kV$, and a wire-plate electrode distance of $d = 1$ cm is presented in Figure IV.16 (a). Despite the applied voltage being significantly increased to 15.5 kV, the overall pattern of the electric wind velocity observed for a small distance of $f = 0.2$ cm remains unchanged from the previous case at 11 kV [as shown in Figure IV.13 (c)]. Similarly, Figure IV.16 (b) displays the 2-D spatial distribution of wind velocity for the same parameters as Figure IV.16 (a), but with an increased wire-plate electrode distance (d) of approximately 1.5 cm. The results show that the distance d has a more significant impact on the general pattern of the EHD force and therefore the EHD flow compared with the high voltage, as evidenced by the decrease in the maximum velocity v_{max} from 4.67 m/s (at d = 1 cm) to 2.8 m/s (at d = 1.5 cm) and the widening of the vortices, which extend up to approximately x = 4.7 cm. Therefore, the increase in distance d up to 1.5 cm further confirms the crucial role played by distance d in shaping the EHD flow.

For both the figures, the increase in vortex size as the wire-plate electrode distance d increases is primarily attributed to the larger volume of the reactor, which allows the EHD flow to occupy a greater space. This expansion in volume results in a weaker EHD force, which is responsible for the decrease in velocity.

IV.2.4.3 Effect of the Wire Radius

The angle variation formed by the average direction vector of the EHD force with respect to the axis perpendicular to the GP ($x = -f/2 - r_0$ or $x = f/2 + r_0$) for three different wire radius values is plotted in Figure IV.17. It can be seen that decreasing the radius r_0 causes a significant decrease in the angle, especially at low applied voltages. For instance, at an applied voltage of 11 kV, the angle θ has values of 33.57°, 23.17°, and 15.22° for wire radii of 150, 100, and 50 μm, respectively.

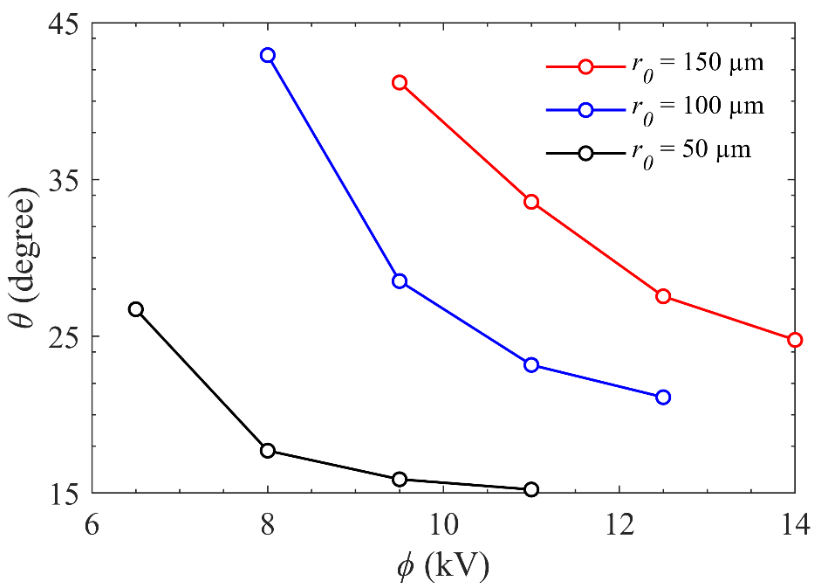

Figure IV.17. Variation in the angle θ that indicates the average direction of the EHD force as a function of the high voltage for interwire distance f = 0.2 cm; wires' radius $r_0 = 50, 100,$ and 150 µm; and interelectrode distance d = 0.5 cm.

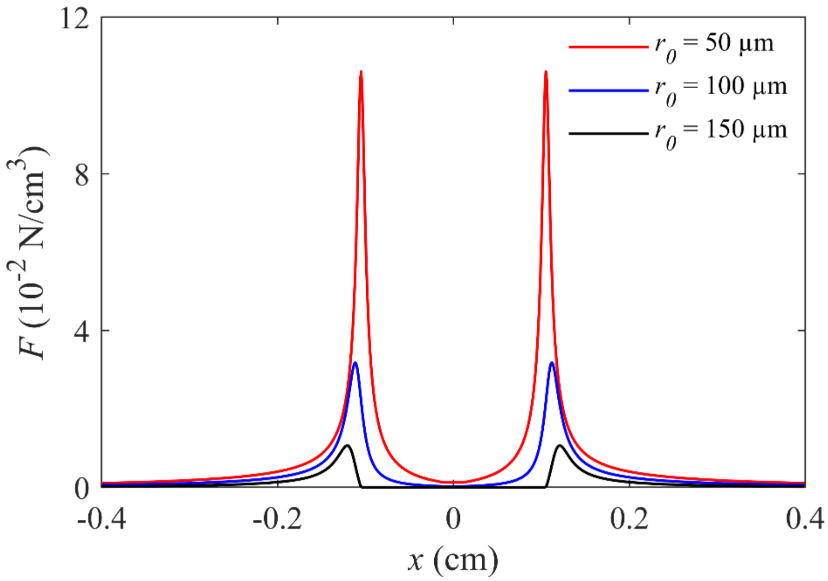

Figure IV.18. EHD force magnitude distribution below the wire along the line y = 0.5 cm for: inter-wire distance f = 0.2 cm; wires radius $r_0 = 50, 100\ 150$ μ*m; inter-electrode distance, d = 0.5 cm; and high voltage* ϕ *= 9.5 kV.*

Figure IV.18 illustrates that for any value of the wire radius r_0, the distribution of the magnitude of the EHD force just below the wire (y = 0.5 cm) is slightly asymmetrical with respect to a straight line passing through the center of each wire and parallel to the oy axis. Reducing the wire radius increases the EHD force. For instance, the maximum magnitude of the EHD force, F_{max}, becomes increasingly larger as the wire radius, r_0, decreases. such as, when r_0 takes the values 150, 100, and 50 μm, and a high voltage of 9.5 kV is applied, F_{max} takes approximately the values $1.2 \times 10^{-2}, 3.25 \times 10^{-2}$, and 10.5×10^{-2} N/cm^3, respectively.

According to the findings presented in Figure IV.19, reducing the wire radius can lead to a more intense EHD flow, as evidenced by the electric wind velocity just below each wire. For instance, for wire radii of 50, 100, and 150 μm, the electric wind velocity just beneath the wire (either the right or the left wire) in the direction of the gas flow is approximately 4.80, 3.86, and 3.8 m/s, respectively. The reduction in EHD flow velocity is greater when the radius is increased from 50 to 100 μm than when the radius is from 100 to 150 μm. What stands out in this figure is that the velocity profile completely changes at a wire radius of 150 μm: two extra small vortices are formed underneath the two wires. This is because the EHD force is smaller at a higher wire radius, which means that the external vortices cannot eliminate or suppress the smaller ones just below the two wires. This behavior was also observed at a low applied voltage (Figure IV.13).

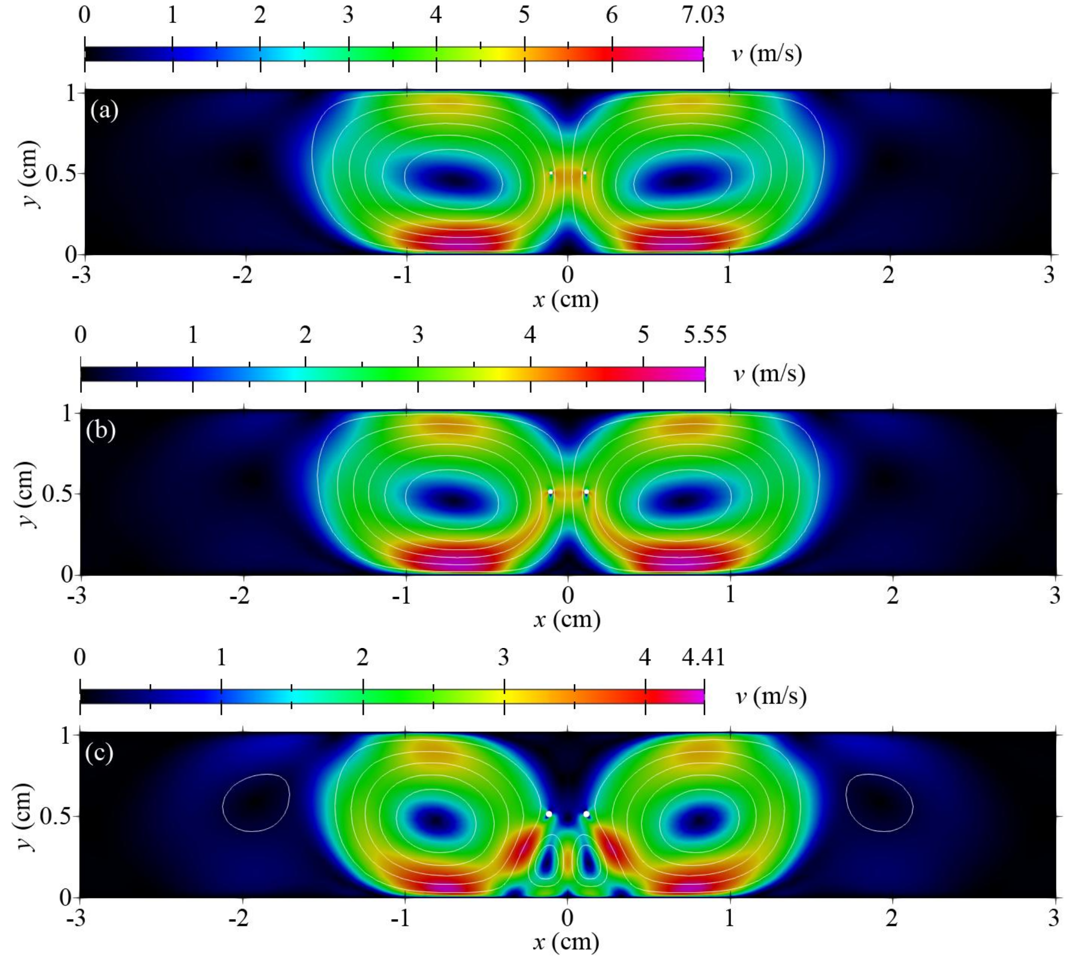

Figure IV.19. Two-dimensional spatial distribution of the magnitude of the gas velocity inside the reactor for two wires: the distance between the two wires is f = 0.2 cm; the interelectrode distance is d = 0.5 cm; the applied voltage is $\phi = +11\ kV$; and the radius of each wire is (a) $r_0 = 50$, (b) $r_0 = 100$, and (c) $r_0 = 150$ µm.

IV.3 Conclusion

Our new numerical model is exploited to study the shielding effect that can arise between adjacent corona discharge electrodes in two-wire-to-plate electrostatic precipitators. As it is known in many applications of electric wind, such as cooling systems, propulsion, and aerodynamic flow, the structure of the EHD flow is a critical parameter that can help control and optimize devices used in such applications. Thus, the present investigation highlights the effect of mutual electrostatic interaction or shielding between two high-voltage wire electrodes on changing the direction and magnitude of the EHD force and the overall structure of the EHD flow. In essence, the present modeling focuses on the effect of shielding on the EHD flow structure, an aspect that has not received much attention in the literature. The main results of this study are given below.

➢ The attenuation of the electric current, the space charge, and the magnitude of the EHD force is more dominant as the distance between the wires gets smaller. This is due to the shielding effect between the wires, which reduces the electric field strength and limits the flow of ions and electrons.

➢ The asymmetrical distribution of the space charge and the EHD force is due to the interaction between adjacent wires, which results in a deflection of the flow. As the distance between the wires decreases, this deflection becomes more pronounced, leading to a larger asymmetry in the distribution of the space charge and the EHD force.

➢ The wire-plate electrode distance and the applied voltage are important factors that affect the structure of the EHD flow. In addition, the wire radius also plays a significant role in determining the magnitude and direction of the EHD force. The effects of these factors are as follows.

- When the distance between the wires is decreased, it can cause a change in the direction of the EHD flow and a decrease in the gas velocity magnitude. This is because the interaction between the wires becomes stronger as the distance between them decreases, leading to more complex flow structures.
- At a small distance ($f < 1$ cm) and a sufficiently high voltage level, the increase in velocity overcomes its decrease due to the short distance f, causing the two wires to behave as a single wire and directing the EHD flow almost along the wire-plate electrode axis ($x = 0$).
- Increasing the distance d between the wires and the plate has the opposite effect compared with increasing the applied high voltage. Notably, as the distance d increases, the EHD flow’s velocity decreases, and the size of the vortices becomes larger. Furthermore, when the distance f is sufficiently small, the effect of the distance d on the EHD flow is more significant than that of the high voltage.
- As the wire radius increases, the strength of the EHD force decreases, but at the same time, the angle between the overall direction of the EHD force and the $x = 0$ axis increases.

Overall, the results of this study provide insight into the effect of the shielding between two high-voltage wires on the EHD flow structure and highlight the importance of considering this effect in the design and optimization of electrostatic precipitators and other devices that rely on the EHD flow.

Reference

[1] R. K. Singh, L. Philip, and S. Ramanujam, “Continuous flow pulse corona discharge reactor for the tertiary treatment of drinking water: Insights on disinfection and emerging contaminants removal,” *Chemical Engineering Journal*, vol. 355, pp. 269–278, Jan. 2019, doi: 10.1016/j.cej.2018.08.109.

[2] C.-S. Ren, T.-C. Ma, D.-Z. Wang, J.-L. Zhang, and Y.-N. Wang, “A study of cross-gas-flow to stabilize an atmospheric pressure glow plasma in a multi-pin-to-multi-cupped-plane negative corona discharge,” *Journal of Electrostatics*, vol. 64, no. 1, pp. 23–28, Jan. 2006, doi: 10.1016/j.elstat.2005.05.001.

[3] F. C. Lai and R. K. Sharma, “EHD-enhanced drying with multiple needle electrode,” *Journal of Electrostatics*, vol. 63, no. 3, pp. 223–237, Mar. 2005, doi: 10.1016/j.elstat.2004.10.004.

[4] I. Suarasan, L. Ghizdavu, I. Ghizdavu, S. Budu, and L. Dascalescu, “Experimental characterization of multi-point corona discharge devices for direct ozonization of liquids,” *Journal of Electrostatics*, vol. 54, no. 2, pp. 207–214, Feb. 2002, doi: 10.1016/S0304-3886(01)00178-4.

[5] M. Bouadi, K. Yanallah, M. R. Bouazza, and F. Pontiga, “Effect of the Variation of the Electrode Geometrical Configuration on the Electric Wind Velocity Produced by an Electric Corona Discharge,” in *ICREEC 2019*, A. Belasri and S. A. Beldjilali, Eds., Singapore: Springer, 2020, pp. 465–474. doi: 10.1007/978-981-15-5444-5_58.

[6] M. R. Bouazza, K. Yanallah, M. Bouadi, and F. Pontiga, “Distributions of Chemical Species Produced by Positive Corona Discharge Using Multi-wire Emitting Electrodes,” in *ICREEC 2019*, A. Belasri and S. A. Beldjilali, Eds., Singapore: Springer, 2020, pp. 531–538. doi: 10.1007/978-981-15-5444-5_66.

[7] S. Arif, D. J. Branken, R. C. Everson, H. W. J. P. Neomagus, and A. Arif, “The influence of design parameters on the occurrence of shielding in multi-electrode ESPs and its effect on performance,” *Journal of Electrostatics*, vol. 93, pp. 17–30, Jun. 2018, doi: 10.1016/j.elstat.2018.03.001.

[8] O. Chibane, A. Rahmani, K. Smili, B. Bendahmane, L. Dascalescu, and A. Kasdi, “Experimental characterization of multi-wire corona electrode configurations,” *Journal of Electrostatics*, vol. 111, p. 103575, May 2021, doi: 10.1016/j.elstat.2021.103575.

[9] P. Marciulionis and S. Zebrauskas, “Comparison of Electric Field of Corona Discharge in Single-Wire- and Multi-Wire-to-Plate Electrode Systems,” *Elektronika ir Elektrotechnika*, vol. 121, no. 5, Art. no. 5, May 2012, doi: 10.5755/j01.eee.121.5.1644.

[10] H. Ziedan, J. Tlustý, A. Mizuno, A. Sayed, and A. Ahmed, “Corona Current-Voltage Characteristics in Wire-Duct Electrostatic Precipitators ‘Theory versus Experiment,’” 2010.

[11] H. Ziedan, J. Tlustý, A. Mizuno, A. Sayed, A. Ahmed, and R. Procházka, “Finite Element Solution of Corona I-V Characteristics in ESP’s with Multi Discharge Wires,” 2011.

[12] A. Z. El Dein and K. Usama, “Experimental and Simulation Study of V–I Characteristics of Wire–Plate Electrostatic Precipitators Under Clean Air Conditions,” *Arab J Sci Eng*, vol. 39, no. 5, pp. 4037–4045, May 2014, doi: 10.1007/s13369-014-1046-2.

[13] A. Kasdi, “Computation and measurement of corona current density and V–I characteristics in wires-to-plates electrostatic precipitator,” *Journal of Electrostatics*, vol. 81, pp. 1–8, Jun. 2016, doi: 10.1016/j.elstat.2016.02.005.

[14] Z. He and E. T. M. Dass, “Correlation of design parameters with performance for electrostatic Precipitator. Part I. 3D model development and validation,” *Applied Mathematical Modelling*, vol. 57, pp. 633–655, May 2018, doi: 10.1016/j.apm.2017.05.042.

[15] X. Wang, “Effects of corona wire distribution on characteristics of electrostatic precipitator,” *Powder Technology*, vol. 366, pp. 36–42, Apr. 2020, doi: 10.1016/j.powtec.2020.02.044.

[16] A. Chelih, M. Bouadi, M. R. Bouazza, A. Safa, K. Yanallah, and F. Pontiga, “Illustration of the dependence of the electrohydrodynamic force on the electrode configuration in a positive corona discharge,” in *2022 2nd International Conference on Advanced Electrical Engineering (ICAEE)*, Oct. 2022, pp. 1–6. doi: 10.1109/ICAEE53772.2022.9962131.

[17] Z. Al-Hamouz, A. El-Hamouz, and N. Abuzaid, “Simulation and experimental studies of corona power loss in a dust loaded wire-duct electrostatic precipitator,” *Advanced Powder Technology*, vol. 22, no. 6, pp. 706–714, Nov. 2011, doi: 10.1016/j.apt.2010.10.005.

[18] M. Abdel-Salam and A. Eid, “Finite element simulation of corona in wire-duct precipitators,” in *Conference Record of the 2002 IEEE Industry Applications Conference. 37th IAS Annual Meeting (Cat. No.02CH37344)*, Oct. 2002, pp. 1383–1389 vol.2. doi: 10.1109/IAS.2002.1042737.

[19] K. Yanallah, F. Pontiga, and J. H. Chen, “A semi-analytical study of positive corona discharge in wire–plane electrode configuration,” *J. Phys. D: Appl. Phys.*, vol. 46, no. 34, p. 345202, Aug. 2013, doi: 10.1088/0022-3727/46/34/345202.

[20] M. R. Bouazza, K. Yanallah, F. Pontiga, and J. H. Chen, “A simplified formulation of wire-plate corona discharge in air: Application to the ion wind simulation,” *Journal of Electrostatics*, vol. 92, pp. 54–65, Apr. 2018, doi: 10.1016/j.elstat.2018.02.001.

[21] A. Pereira and H. M. Ramos, “CFD for hydrodynamic efficiency and design optimization of key elements of SHP,” *International Journal of Energy and Environment*, vol. 1, no. 6, 2010.

CHAPTER V : Numerical study of a New Corona Ionic Wind Blower used for Solar Panel cleaning

The potential of solar energy as a sustainable power source remains hindered by various efficiency limitations. One of the major challenges is the accumulation of dust on photovoltaic (PV) panels, leading to the decrease of the efficiency and the need for regular cleaning. To address this issue, this work aims to explore the use of ionic wind, generated by corona discharge, as an innovative method for dust removal from PV panels. In line with this objective, this chapter presents a numerical analysis of electro-hydrodynamic (EHD) air blowers with wire-to-rectangle configurations to harness the potential of ionic wind for cleaning PV panels. The study utilizes 2D models that have undergone experimental validation. The results highlight a parametric analysis, shedding light on how different geometrical parameters influence the performance of the ionic wind air blower and its energetic efficiency. The geometrical parameters considered in the simulation are the distance between electrodes, the width of the grounded plate, the wire radius and the inclusion of the grounded plates.

V.1 Introduction

The current study expands upon our earlier research [1], delving into a numerical exploration of electro-hydrodynamic (EHD) air blowers employing wire-to-rectangle electrode configurations, specifically designed for cleaning of photovoltaic (PV) panels. Despite the great potential of solar energy, it currently makes up only a small fraction of the world's energy supply due to many problems that limits their efficiency [2]. For example, as shown in the literature, accumulated dust on photovoltaic (PV) panels can significantly decrease their efficiency [3], making it necessary to clean them regularly. There are three main cleaning methods for PV panels: mechanical, coating, and electrostatic techniques [4, 5]. Among mechanical techniques, air-blowing [6], robotic [7, 8], water-blowing [9], and ultrasonic vibration methods [10] are investigated, but they consume substantial power due to their moving parts. Water-based cleaning is efficient but has the drawback of using significant amounts of water, especially problematic in arid regions [11, 12]. The coating method involves nanotechnology to create super hydrophilic and hydrophobic thin films on the solar panel surface [13]. While effective, it can be further combined with other techniques for better results [14].

Apart from these, there are two electrostatic methods: one relies on induction electrostatic charge to repel dust particles using parallel electrodes with high voltage [15, 16]. The drawback is the need for two power supplies with opposite polarities for charging and lifting particles. The other method, known as EDS (Electrodynamic Screen) cleaning, expels dust using electric curtain boards with parallel wire electrodes on a dielectric layer deposited on the panel glass [17, 18]. However, its effectiveness depends on the electrical characteristics of the sand particles [19, 20].

The ionic wind, which is an airflow generated by corona discharge, is being explored for the first time by our team with collaboration with APLEC laboratory of Sidi bel Abbes University [21, 22] as an alternative method for cleaning dust from the surfaces of photovoltaic (PV) panels. The ionic wind has several advantages over traditional cleaning methods, such as the ability to avoid using water in areas where it is either unavailable or too expensive [21]. Additionally, it does not require solid parts movement, that can damage the surface of photovoltaic (PV) panels, and increase maintenance costs.

In addition to its utilization in enhancing the efficiency of solar panels, the ionic wind has others various interesting applications across different fields. Some of the notable applications include fluid pumping [23], cooling system [24], evaporation and drying [25, 26], electrohydrodynamic thrusters [27, 28], and aerodynamic flow control [29].

In this context, to comprehend the mechanisms governing the cleaning of solar panels from dust particles through the utilization of electric wind, this chapter presents a comprehensive numerical study focusing on electro-hydrodynamic (EHD) air blowers equipped with wire-to-rectangle configurations. In reference [21], we have shown through experiments that ionic wind can be successfully used for dust cleaning from solar panels surface. A corona system based on needles-rectangular plate configuration has been presented. However, a geometrical optimization of the device is necessary in order to improve its efficiency. In this work, a numerical study of such ionic wind air blower device is presented. The analysis is based on 2D numerical simulation of the electric field, space charge, and the generated EHD phenomena. The simulation is validated experimentally using electric current and air velocity measurements. The results include a parametric analysis that demonstrates how the geometrical parameters affect the performance of the air blowers. The present study constitutes an extension of our previous work, specifically the simulation [1], by considering the efficiency of the conversion of electric energy to mechanical energy.

The current simulation employs an innovative approach capable of managing complex electrode configurations [30]. It relies exclusively on numerically integrating the Laplacian electric field to ascertain the electric field lines. Subsequently, employing previously developed semi-analytical formulations [31, 32], the method yields satisfactory approximations of the electric field and space-charge density, facilitating the determination of the EHD force density. This approach stands out for its ease of implementation and computational efficiency. Unlike finite element method (FEM) or finite volume method (FVM) approaches [33, 34], it does not necessitate iterative processes on an unstructured mesh to solve electrical equations. Moreover, it sidesteps convergence issues typically associated with solving the Gauss equation coupled with continuity equations of charged species.

V.2 Results and discussion

The electro-hydrodynamic air blower device is composed of a wire electrode that is connected to a high DC voltage and a grounded rectangular shape frame electrode. A 2D graphic of the blower device is shown in Figure V.1. The EHD force, generated by the corona discharge, causes the electric wind to flow from the wire electrode, toward the frame electrode, and then exit through two openings located below the frame. To simulate the EHD flow, we assume that the corona discharge is in the stationary regime. To evaluate the EHD force acting on air, it is necessary to calculate the electric field and the charge density.

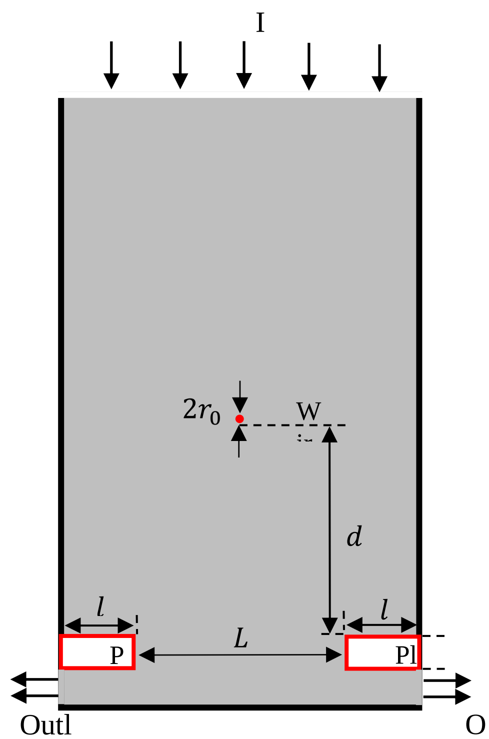

Figure V.1. Schematic illustration of the corona ionic wind blower (rectangular plate). d = 3 cm, l = 1 cm, r_0 = 100 µ*m, L = 3 cm.*

The numerical results are shown in Figure V.2 - Figure V.6, which illustrate the distributions of the electric field, space charge density, EHD force, and EHD velocity flow, respectively. Validation results are presented in Figure V.9, comparing the outlet velocity obtained from the simulation against experimental data. The numerical analysis explores the impact of design parameters on the EHD air flow, including the inter-electrode distance (d), ground plate width (l), wire radius (r_0) and inclusion of the grounded plates.

The numerical results presented in this section were obtained using a corona wire of radius $r_0 = 100$ µm and an inter-electrode separation $d = 3$ cm. The negative voltage applied to the corona wire have been chosen to be $\phi = -25\ kV$, which corresponds to a current intensity per unit of wire length of 805 µA/m.

Before delving into the behavior of the EHD force, it is essential to provide an overview of the electric field and space charge density profiles, as the EHD force is intricately linked to these physical quantities through equation (II.49). The two-dimensional distribution of the electric field is depicted in Figure V.2, with additional clarity achieved by plotting the electric field lines starting from the wire and extending to the two plates. Notably, the electric field intensity exhibits significant value near the wire, reaching approximately 1.19×10^7 V/m. However, it rapidly decreases as we move in the direction of the plates. For instance, at the end of the line, the electric field intensity diminishes to around 10^6 V/m. This variation in electric field intensity has significant implications on the acceleration of air gas particles within the drift region. A close examination of Figure V.2 shows that the electric field's minimal value is reached a few millimeters before the plate and then rises toward the plates. This is due to the accumulation of space charges, which intensifies the electric field on the ground electrode. The electric field on the wire surface can be determined by Peek's law [35]. However, in the drift region, the mobility of the ions impacts the intensity of the electric field.

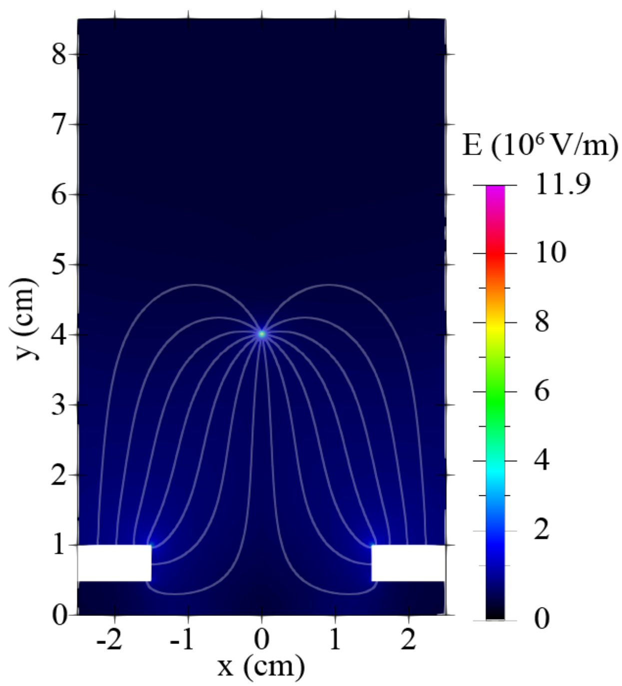

Figure V.2. 2D-spatial distribution of the electric field for $d = 3$ cm, $l = 1$ cm, $r_0 = 100$ μm, $L = 3$ cm and $\phi = -25$ kV.

In the negative corona, electrons are expelled from the wire. As these electrons travel, they undergo inelastic collisions with neutral molecules, resulting in ionization and the creation of secondary electrons. During this process, the positive ions produced are drift towards the wire.

Simultaneously, electrons combine with neutral particles, forming negative ions that drift towards the plates. As a result of these processes, the space charge in the drift region is predominantly dominated by the presence of negative ions (Figure V.3).

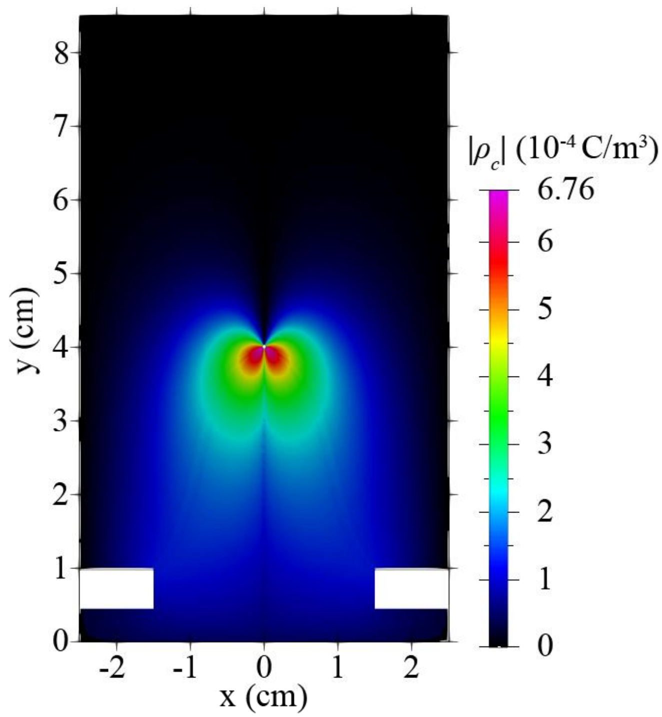

Figure V.3. 2D-spatial distribution of the space charge density for $d = 3\ cm$, $l = 1\ cm$, $r_0 = 100\ \mu m$, $L = 3\ cm$ *and* $\phi = -25\ kV$.

Figure V.3 presents the 2D special distribution of the space charge density. According to M. R. Bouazza et al. [32], electrons have a small contribution to the total EHD force since their number density is at least two orders of magnitude lower than the densities of positive and negative ions. As a result, in the ionization region, the EHD force is predominantly owing to positive ions, with the cathode having the maximum force density ($\sim 1.08 \times 104\ \mathrm{N/m^3}$). Negative ions, on the other hand, are the largest contributors to the EHD force in the drift region. Indeed, it is important to highlight that the electric field intensity in the drift region is approximately one order of magnitude lower than that in the ionization region. As a result, the EHD force exerted in the drift region is correspondingly weaker, even though its influence extends over a larger area. Certainly, the difference in electric field strength between the ionization region and the drift region plays a crucial role in shaping the magnitude and impact of the Electro-Hydrodynamic (EHD) force within the cleaning blower device.

It seems form Figure V.3 that there is no space charge at the central section of the cell (at x = 0 cm). However, Figure V.4 provides a detailed cross-sectional view of the space charge distribution of Figure V.3 along the axes at y = 0.25 cm, y = 1.1 cm, and y = 3.0 cm. The analysis reveals that while the space charge slightly decreases towards the center of the cell (at x = 0 cm), it remains clearly non-zero. This indicates that a measurable space charge is present at the center, even though it is reduced in comparison to other regions of the cell.

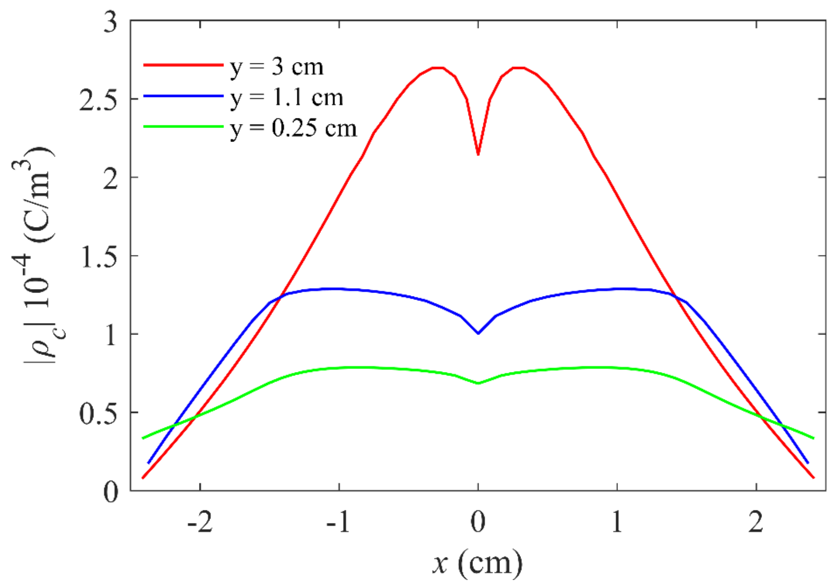

Figure V.4. The spatial distribution of the space charge density along the axes at $y = 0.25\ cm, y = 1.1\ cm$, and $y = 3\ cm$, for $d = 3\ cm$, $l = 1\ cm$, $r_0 = 100\ \mu m$, $L = 3\ cm$ and $\phi = -25\ kV$.

Figure V.5 depicts the 2D spatial distributions of EHD force density, as well as a zoom around the wire. As previously stated, the EHD force undergoes a sign reversal towards the boundary where electron attachment takes over ionization. The air gas is pushed towards the plates in the negatively charged drift region.

Figure V.6 illustrates the gas velocity distribution in the inter-electrode space generated by the negative corona discharge, together with the streamlines, with a $-25\ kV$ applied voltage. Because the corona plasma region is limited to a small layer around the wire, the flow distribution shown in Figure V.6 is primarily determined by the EHD force acting in the drift zone. The EHD force acts as a propulsive mechanism, accelerating the air gas from the corona wire towards the two plates. As the air gas approaches the plates, it undergoes deflection along each plate's surface. Consequently, in the downstream region of the wire, the flow structure is

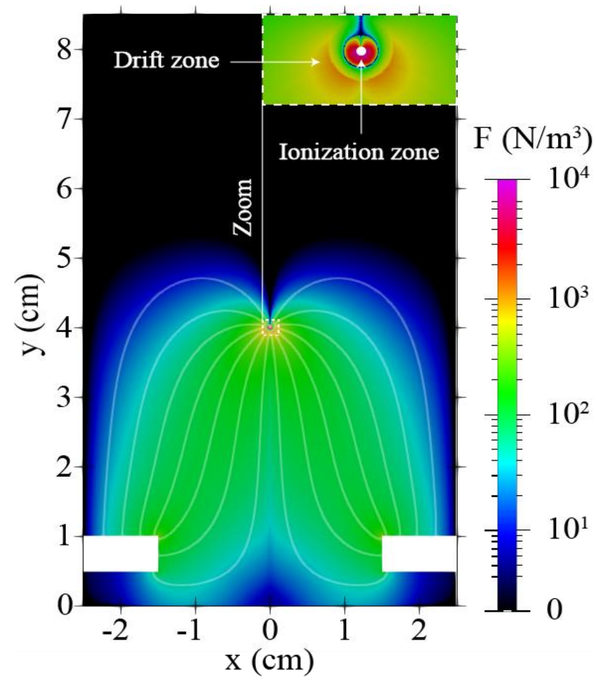

Figure V.5. 2D-spatial distribution of the of EHD force density for $d = 3\ cm$, $l = 1\ cm$, $r_0 = 100\ \mu m$, $L = 3\ cm$ and $\phi = -25\ kV$.

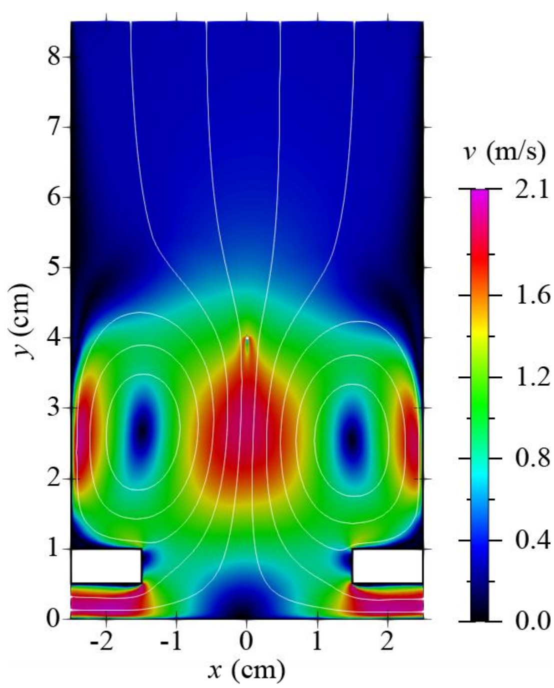

Figure V.6. 2D spatial distribution of the ionic wind velocity inside the blower device for $d = 3\ cm$, $l = 1\ cm$, $r_0 = 100\ \mu m$, $L = 3\ cm$ and $\phi = -25\ kV$.

characterized by the presence of two recirculating and stable vortices situated above each plate, originating from hydrodynamic effects. A detailed examination of Figure V.6 highlights a tiny asymmetry in the gas flow, which stems from the use of an unstructured triangular mesh. While this asymmetry has minimal influence on the overall flow dynamics, it can be addressed by increasing the mesh density. However, this approach may be computationally expensive, particularly during parametric studies. Thus, finding an optimal balance between mesh resolution and computational efficiency is crucial. The maximum air velocity, reaching approximately 2.1 m/s, is observed beneath the wire and within the deflected flow that circulates parallel to the walls on both sides of the blower. Furthermore, the gas velocity remains high at the outlet boundaries due to the small outlet surface, which enhances the flow's kinetic energy in those regions. The combination of these flow characteristics and vortices contributes to the overall efficiency and performance of the EHD air blower. Understanding these flow patterns is vital for optimizing the design and functionality of such EHD device.

V.3 Comparison with experiments

In this subsection, modeling results are compared with our experimental measurements. The studied cleaning device (or the blower device) is an electrostatic actuator that generates an 'ionic wind' through corona discharge, facilitated by a system of electrodes consisting of a wire and a rectangular aluminum frame [22] (See Figure V.7). The grounded electrode, made of a 1 cm wide aluminum strip (or plate), has an inner length of 23 cm. The high voltage electrode, a wire positioned 3 cm above the grounded electrode, is powered by a high-voltage DC source (XP Glassman, 40 kV, 10 mA). The ionic wind flows through the metal frame and exits through a 5 mm opening at the bottom of the actuator's front wall. This opening is an empty space between the actuator's lower part and the surface of the solar panel. The actuator shaped as a parallelepiped and constructed from polyvinyl chloride (PVC). Wind velocity is measured with a hot-wire anemometer (Testo 405i), with the sensor positioned in the front of the actuator at the opening of the front wall through which the electric wind exits. It is to note that Figure V.1 presents a cross-section of the actuator, which is indicated by the plane shown in Figure V.7.

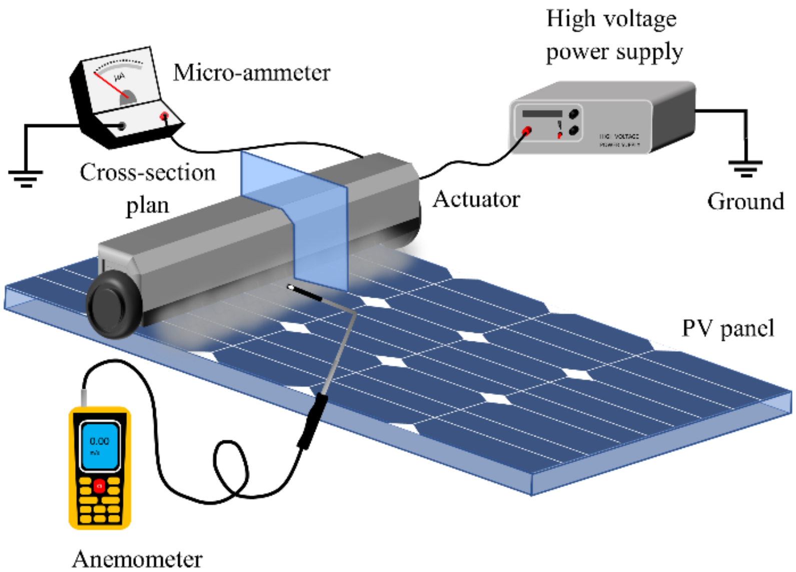

Figure V.7. Schematic presentation of the experimental setup for the solar panel dust cleaning system.

The validation process is twofold: Firstly, comparing the calculated electric current with the measured current-voltage characteristic of corona discharge to estimate the EHD force and flow profile. Secondly, comparing the model-predicted average flow velocity at the blower outlet with experimental measurements. More information about the experimental setup can be obtained from reference [22]. This comparison ensures the accuracy and reliability of the numerical model in simulating the EHD flow behavior.

Figure V.8 and Figure V.9 show the numerical simulation of the current-voltage characteristic and the average outlet velocity versus applied voltage, respectively. The comparison, were conducted for corona wire of radius 100 µm, with the applied voltage being varied. Satisfactory agreement was observed for both parameters: the electric current and the outlet velocity. As confirmed by the results presented in Figure V.9, the raise of the applied voltage and, therefore, of the corona current intensity, implies an augmentation of the EHD force. Consequently, there is an increase in the ionic wind velocity at the outlet. These findings align with different published data suggest an almost linear dependence of the averaged wind velocity with the square root of the discharge current for others electrode configurations [36].

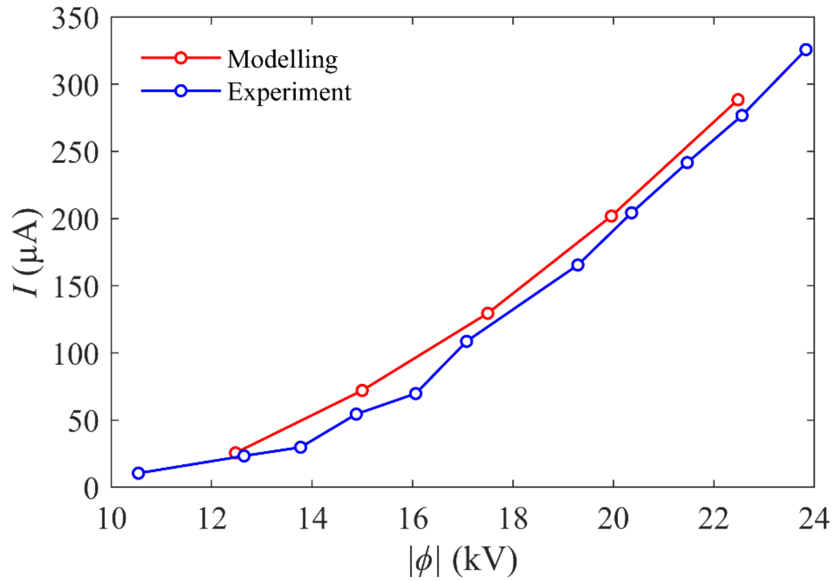

Figure V.8. Current–voltage characteristic of a negative corona for d = 3 cm, l = 1 cm $r_0 = 100\ \mu m$, *L = 3cm.*

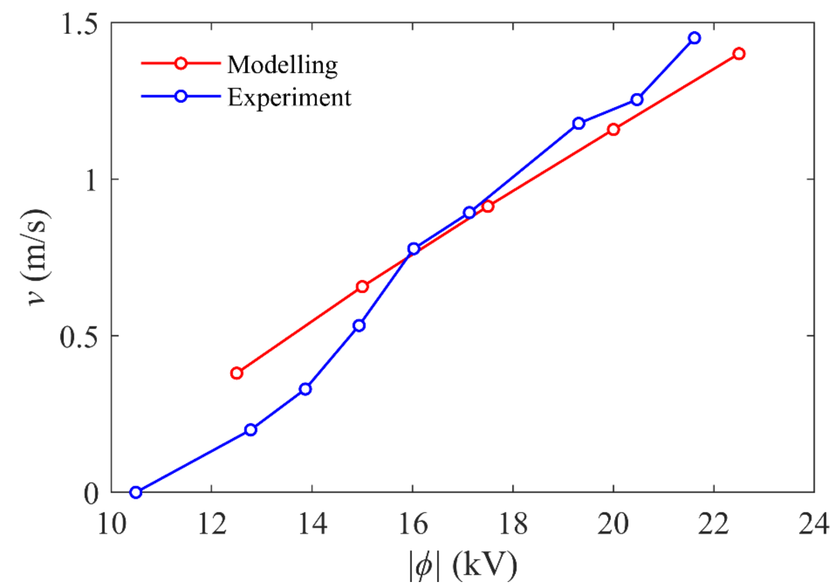

Figure V.9. Wind velocity produced by a negative corona for d = 3 cm, l = 1 cm, $r_0 = 100\ \mu m$, *L = 3cm.*

V.4 Calculation of mechanical efficiency

To optimize energy usage and process effectiveness of the blower device, it is necessary to compute the efficiency of the conversion of electric energy to mechanical energy. In addition, understanding the energy efficiency of generation of the electric wind, such as in corona discharge devices, is crucial for advancing sustainable and resource-efficient manufacturing processes of solar energy. Note that the results presented in this section are based on numerical simulations.

The efficiency of generating the electric wind, which expresses the conversion of the electric energy into mechanical energy, can be calculated using the relation [37]:

$$\eta_{eff} = \frac{P_{mec}}{P_{ele}} \tag{V.1}$$

With P_{mec} is the mechanical energy (power) given by

$$P_{mec} = \frac{1}{2}\rho A_g v_g^3 \tag{V.2}$$

Where, A_g the gas flow cross-section and v_g the airflow velocity crossing the surface A_g.

P_{ele} is the electrical energy (power) given by

$$P_{ele} = \phi . I \tag{V.3}$$

where ϕ is the applied voltage and *I* is the electric current.

Replacing (V.2) and (V.3) in (V.1) gives

$$\eta_{eff} = \frac{\frac{1}{2}\rho A_g v_g^3}{\phi . I} \tag{V.4}$$

The measured characteristic current-voltage taken from reference [22] can be well fitted using the famous formulas [38, 39]:

$$I = c_1 \cdot \phi \cdot (\phi - \phi_{onset}) \tag{V.5}$$

where c_1 is geometric constant and ϕ_{onset} is the onset voltage.

In our case, as shown by Sigmond's law [37], the airflow velocity v_g is proportional to square root of the electric current as follow:

$$v_g = \sqrt{\frac{I.d}{\rho \mu_n A_g}} \tag{V.6}$$

Equation (V.6) can be written;

$$v_g \approx c_2 \sqrt{I} \tag{V.7}$$

where c_2 is a constant that depends on geometrical and mechanical parameters.

Replacing (V.7) and then (V.5) in (V.4) gives

$$\eta_{eff} = \frac{\frac{1}{2}\rho A_g \left(c_2 \sqrt{I}\right)^3}{\phi \cdot I} = \frac{\frac{1}{2}\rho A_g (c_2)^3 \sqrt{c_1 \cdot \phi \cdot (\phi - \phi_{onset})}}{\phi} \approx \sqrt{\left(1 - \frac{\phi_{onset}}{\phi}\right)} \tag{V.8}$$

This relation illustrates that increasing the applied voltage (or the electric power) leads to a direct enhancement in the mechanical efficiency. The underlying physical explanation lies in the reduction of the plasma's equivalent resistance because of the produced charge density as the electric current (or electric power) intensifies, as shown by relation (II.49). This reduction implies that we generate more ions with less energy when increasing the input power. Consequently, the electric wind, generated through the collisions between ions and neutral particles, experiences an increase in the flow rate with a lower energy input. Thus, the overall efficiency is heightened due to the increased electric wind velocity achieved with less energy consumption.

V.5 Parametric study

V.5.1 Effect of the inter-electrode distance

Figure V.10 and Figure V.11 illustrate the impact of the distance (*d*) between the wire and the ground frame on the average outlet velocity of the ionic wind and the mechanical efficiency. Four values of the inter-electrode distance are considered: *d* = 1, 2, 3 and 4 cm, whereas the cleaner aperture *L* was fixed to 3 cm and *l* to 1cm.

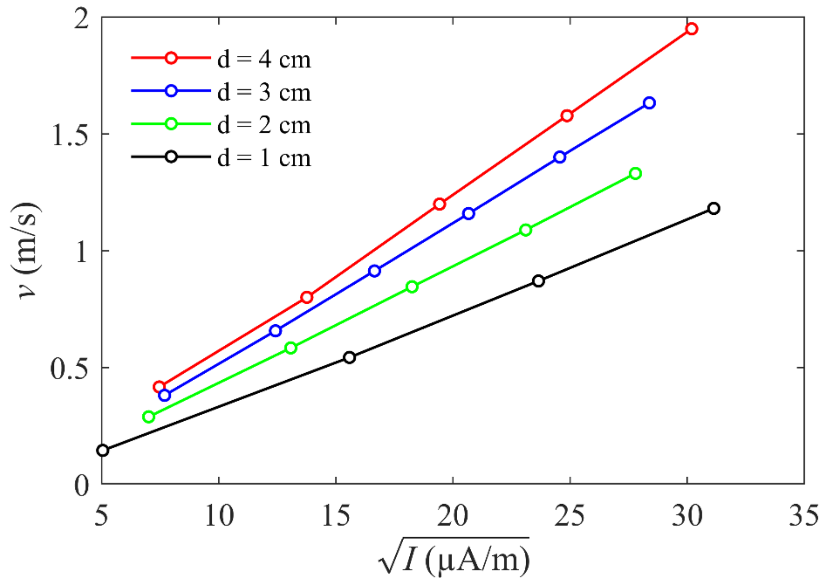

Figure V.10. Ionic wind velocity versus the square root of the electric current for four different values of the inter-electrode distance: d = 1, 2, 3 and 4cm.

In both experiment and modelling, the critical voltage for the onset of corona discharge is found to be influenced by the separation between the wire and the plate (electrode separation). When the distance between the wire and the plates is increased, the corona onset voltage also rises, resulting in less electric current flowing for the same applied voltage. This reduction in electric current intensity leads to a lower Electro-Hydrodynamic (EHD) force and a decrease in the gas flow intensity within the drift region. For instance, reducing the inter-electrode gap from 4 cm to 1 cm leads to a nearly 40% decrease in the outlet velocity. Additionally, as mentioned earlier, the outlet flow velocity follows the square root of the current intensity for all four values of the inter-electrode distance. This behavior of the gas velocity aligns with the expression (V.6) given by Sigmond's law [38].

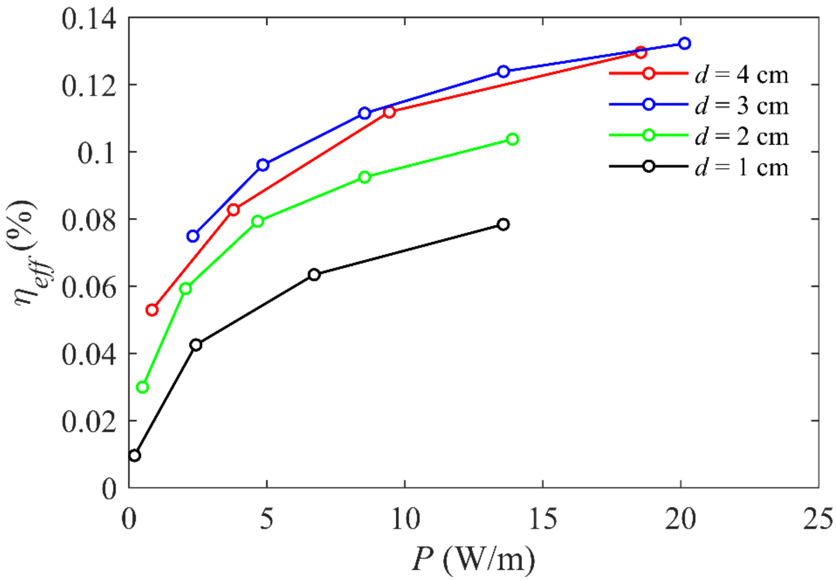

Figure V.11. The efficiency as function of the electric consumed power for four different values of the inter-electrode distance.

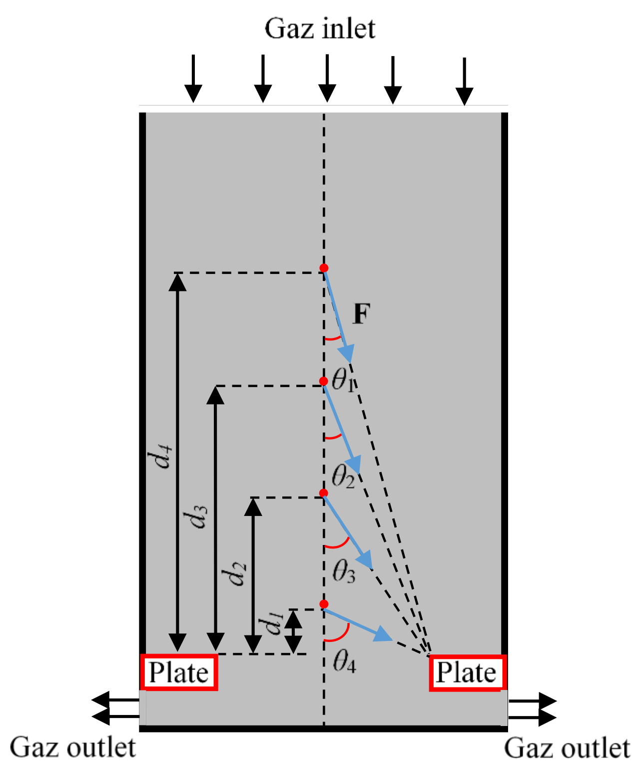

Figure V.12. Diagram showing the change in the direction of the force with the inter-electrode distance.

As illustrated in Figure V.11, the efficiency increases with the inter-electrode distance (d), peaking at d = 3 cm, but slightly drops at d = 4 cm. This trend is explained by the enhanced distribution of electric field lines at larger d, improving kinetic energy transfer through the vertical components of the Electro-hydrodynamic (EHD) force. However, a further increase in d, under constant electric power, reduces the impact of the EHD force due to decreased electric field strength. A delicate balance exists between the strength and direction of the Electro-hydrodynamic force. For instance, at d = 3 cm, despite a lower EHD force strength than at d = 1 and 2 cm, the electric EHD force is highly effective, characterized by an optimal angle (See Figure V.12). This results in a larger region between collecting electrodes, leading to a comparatively superior generation of ionic wind.

V.5.2 Effect of the width of the grounded plates

Figure V.13 depicts the relationship between the electric wind velocity and the size of the ground electrode or discharge cross-section where the aperture L was fixed to 3 cm. For instance, at an electric current of 150 µA, the wind velocity increases from 0.8 m/s to 1.25 m/s when the width of the grounded electrode is reduced from 1.5 cm to 0.1 cm. For a given value of the total electric current, the reduction in the width of the grounded plates leads to two contrasting effects. On one hand, a smaller discharge cross-section results in higher current density distribution, leading to a stronger Electro-Hydrodynamic (EHD) force. On the other hand, the overall volume action of the EHD force decreases. Based on the results in Figure V.13, the increase in current density has a dominant influence over the decrease in volume action of the EHD force due to the reduced cross-section. This results in an overall increase in electric wind velocity. Another parameter that appears to play an important role in increasing wind velocity is the reduction in the width of the grounded plate, which could lead to a pressure drop and subsequently reduce flow resistance. However, simulations conducted confirm that the pressure drop is not the dominant factor for the current geometrical parameters of the actuator. To demonstrate this, we calculated the outlet velocity with a ground plate width of $l = 1.5$ cm and $L = 2$ cm. We then applied the same force corresponding to these dimensions to a smaller plate with $l = 0.1$ cm and $L = 4.8$ cm. For example, with an electric current value of 345µA, we observed a slight increase in wind velocity from 0.99 m/s to 1.05 m/s (See Figure V.14 (a) and Figure V.14 (c) below). However, this is still lower than the value of 1.146 m/s shown in Figure V.14 (b), which corresponds to the actual simulation for the plate with l = 0.1 cm and L = 4.8 cm. This led us to conclude that the pressure drop is not the dominant effect in the parametric study.

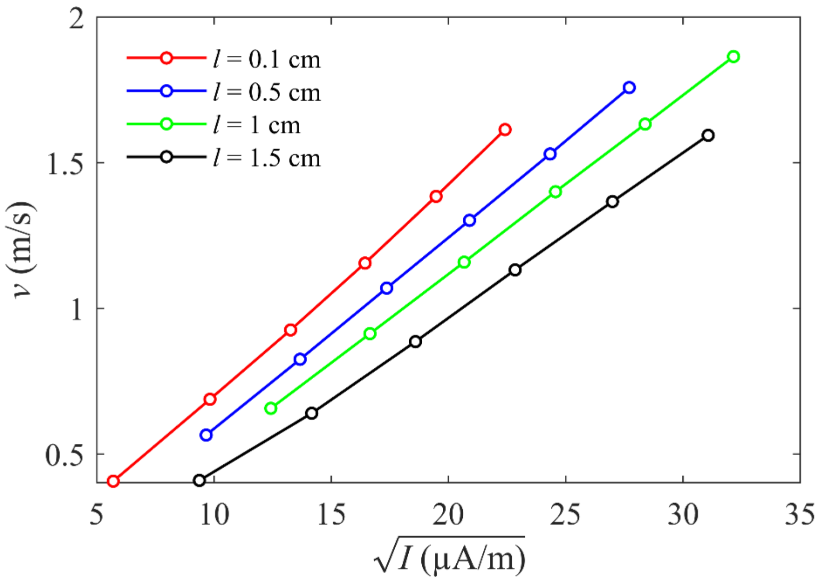

Figure V.13. Ionic wind velocity versus the square root of the electric current for four different values of the width of the grounded plates: l = 0.1, 0.5, 1 and 1.5 cm

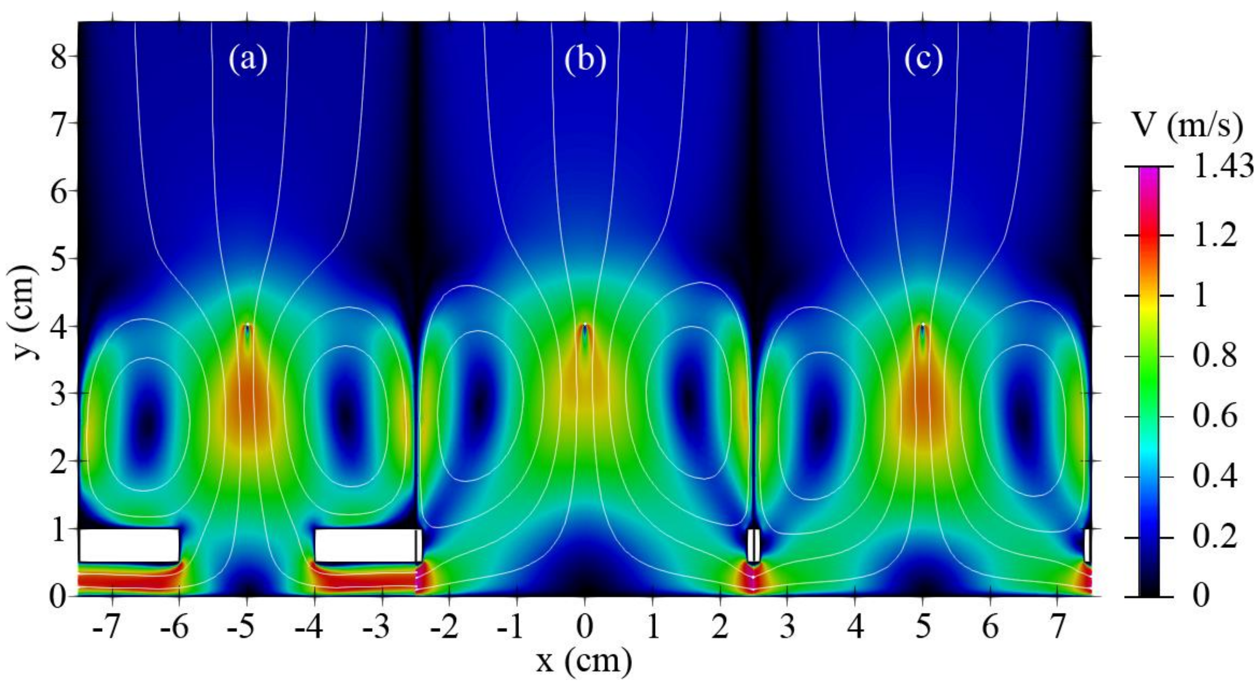

Figure V.14. Streamlines and 2D spatial distribution of the ionic wind velocity inside the blower device for d = 3 cm, r_0 = 100 µm, (a)-l = 1.5 cm and L = 2 cm, (b)-l = 0.1 cm, L = 4.8 cm and I = 345µA.

The correlation between the electric wind velocity and the configuration of ground electrode significantly impacts the mechanical efficiency. This relationship stems when the gas flow generated by the corona discharge traversing the aperture between the two grounded plates. Indeed, larger grounded electrodes slow down the gas flow by creating two tightened vortices. In contrast, thicker grounded electrodes which create a higher EHD force density make the two vortices less stiff, resulting in a smoother flow with higher velocity, as depicted in Figure V.14. This leads to reduced energy loss, enhancing the efficiency of converting electric energy to mechanical energy, as illustrated in Figure V.15. For instance, at an electric power of 14 Watts/m, the efficiency values are 0.09, 0.13, 0.15, and 0.19 for width's plate of 1.5, 1, 0.5, and 0.1 cm, respectively.

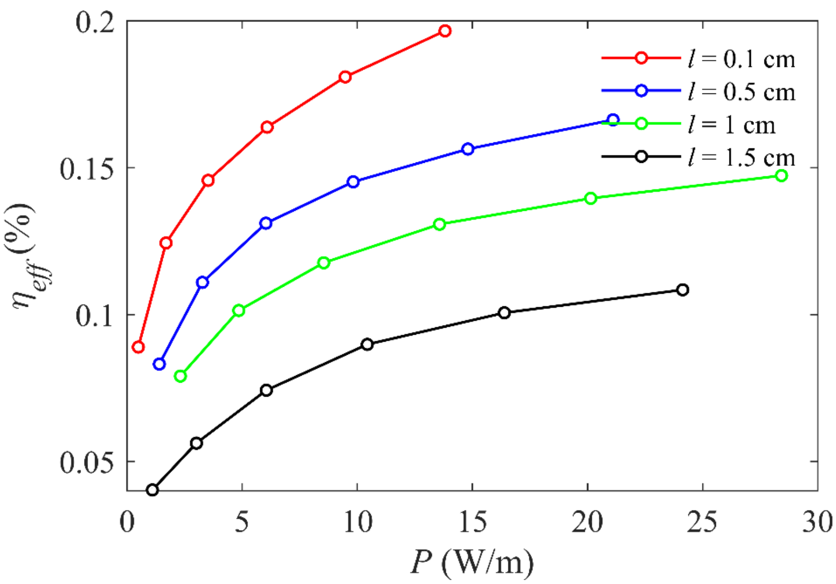

Figure V.15. The efficiency as function of the electric consumed power for four different values of the width of the grounded plates.

V.5.3 Effect of the wire radius

The effect of varying the wire radius on the space charge density is shown in Figure V.16 and Figure V.17. The funding demonstrates that the space charge distributions across the discharge space are qualitatively similar for all three wire radii ($r_0 =$ 50 μm, 100 μm, and 150 μm) (See Figure V.17). However, on a quantitative level, the space charge density increases as the wire radius decreases (See Figure V.17). It to note, that the distribution of the space charge has great influence on the EHD force distribution and therefore the EHD flow.

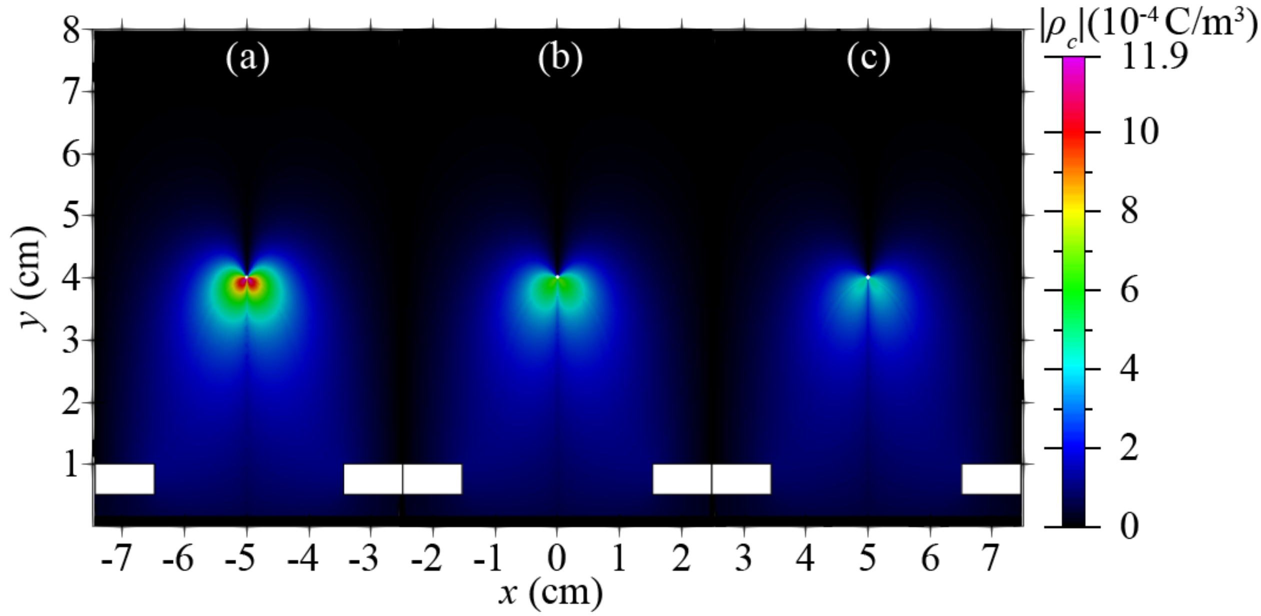

Figure V.16. 2D-spatial distribution of the space charge density for d = 3 cm, l = 1 cm, L = 3 cm, $\phi = -25\ kV$ and $r_0 = 50$ µm (a), $r_0 = 100$ µm (b), $r_0 = 150$ µm (c).

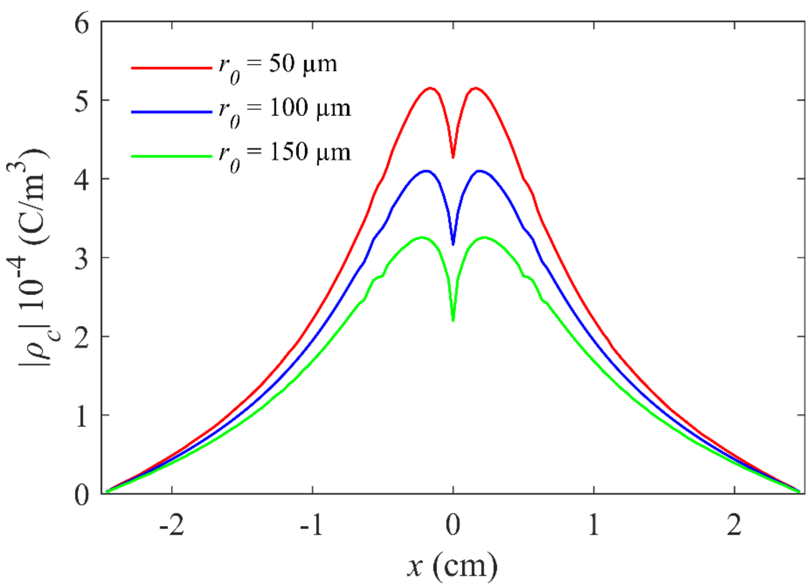

Figure V.17. The spatial distribution of the space charge density along the axes at y = 3. 5 cm for d = 3 cm, l = 1 cm, L = 3 cm, ϕ = -25 kV and $r_0 = 50$ µm (a), $r_0 = 100$ µm (b), $r_0 = 150$ µm (c).

The effect of varying the wire radius on the EHD velocity is illustrated in Figure V.18 for an inter-electrode separation of 3 cm. Figure V.18 shows that the wire radius does not impact the wind velocity for any fixed value of the electric current, in line with relation (V.6). However, when the applied voltage remains constant, the wind velocity increases as the wire radius decreases. According to Peek's law [35], the radius of the corona wire affects both the electric field on the cathode (Equation (II.23)), and the critical voltage for the onset of corona discharge.

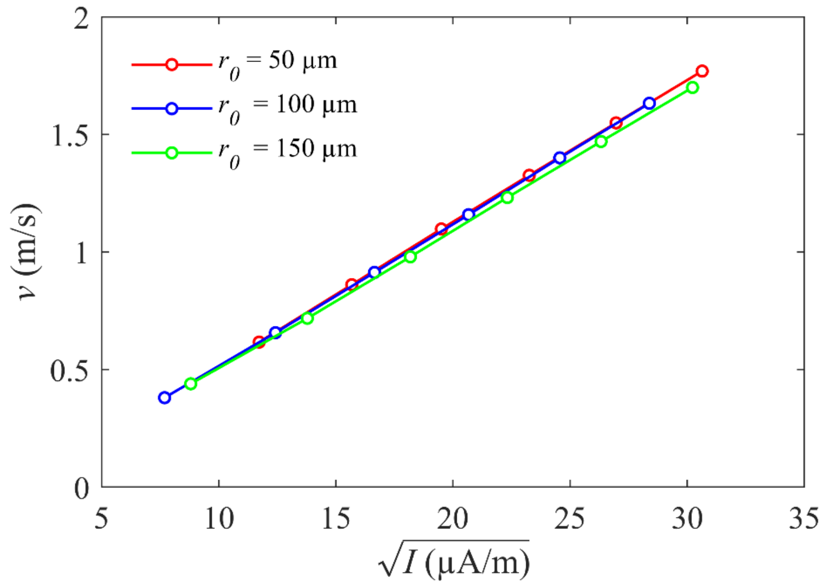

Figure V.18. Ionic wind velocity versus the square root of the electric current for three different values of the wire radius: $r_0 = 50, 100,$ *and* $150\ \mu m$.

Decreasing the radius of the corona wire results in a lower corona onset voltage and higher electric currents for the same applied voltage. For instance, at an applied voltage of 20 kV, the electric currents corresponding to the mentioned radiuses are 540.9, 427.1, and 330.5 µA, respectively. This is explained by the fact that the electric current is related to space charge which increases quantitatively with smaller wire radii although the space charge distributions remain qualitatively similar across the discharge space. Consequently, as the wire radius decreases, the current intensity increases, leading to a stronger Electro-Hydrodynamic (EHD) force and faster gas velocity. This correlation is clearly evident in the results depicted in Figure V.19. Indeed, using a lower wire radius offers the advantage of operating the cleaning devices with lower voltage. The effect of the wire radius on the trend of the mechanical efficiency differs from its influence on the trend of the wind velocity, as illustrated in Figure V.20. Notably, reducing the wire radius corresponds to an increase in efficiency. For instance, at a power of 15 W/m, efficiency rises from 0.11% to 0.138% when the wire radius decreases from 150 µm to 50 µm. This behavior is attributed to the fact that a decrease in wire radius results in an increase in electric current which implies an increase in the gas velocity (see relation (V.6) or (V.7)) and, consequently, an improvement in efficiency, as previously explained.

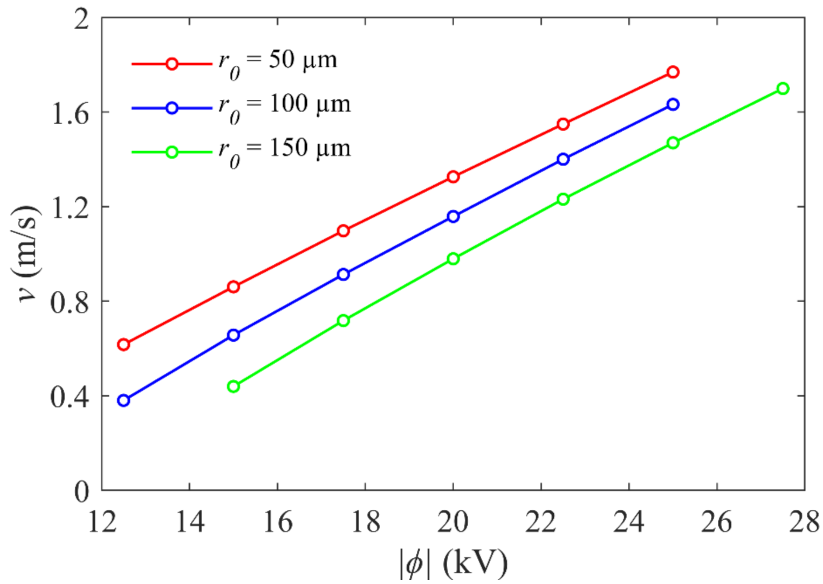

Figure V.19. Ionic wind velocity versus the applied voltage for three different values of the wire radius: $r_0 = 50, 100,$ *and* 150 μm.

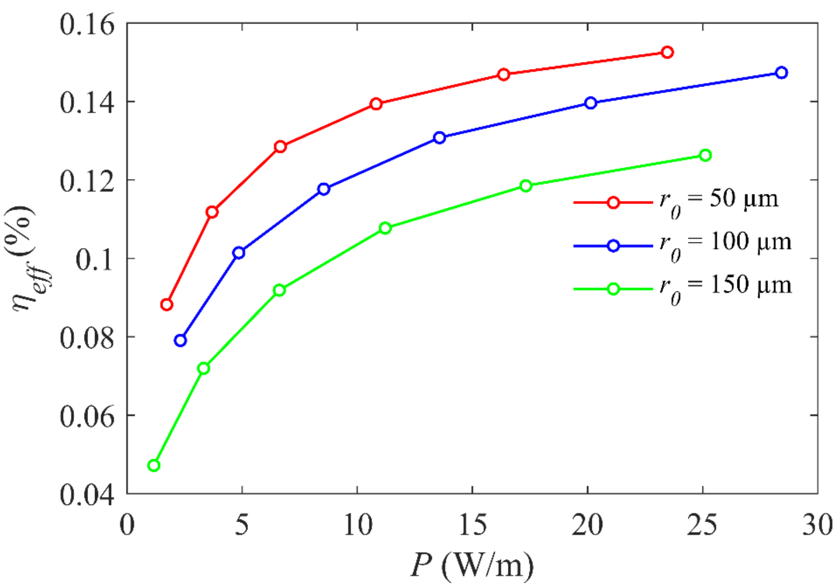

Figure V.20. The efficiency as function of the consumed electric power for three different values of the wire radius.

V.5.4 Effect of the inclusion of the grounded plates

In the modified electro-hydrodynamic (EHD) air blower device, as depicted in Figure V.21, the angle of deviation (θ_p) of the grounded rectangular plate electrode has been considered. This adjustment alters the configuration of the blower, specifically by decreasing the total wide of the air blower's inlet while maintaining a constant outlet length. The modified geometry impacts the electric wind flow pattern, as the EHD force generated by the corona discharge will now have a different direction and magnitude due to the altered angle of the grounded plates.

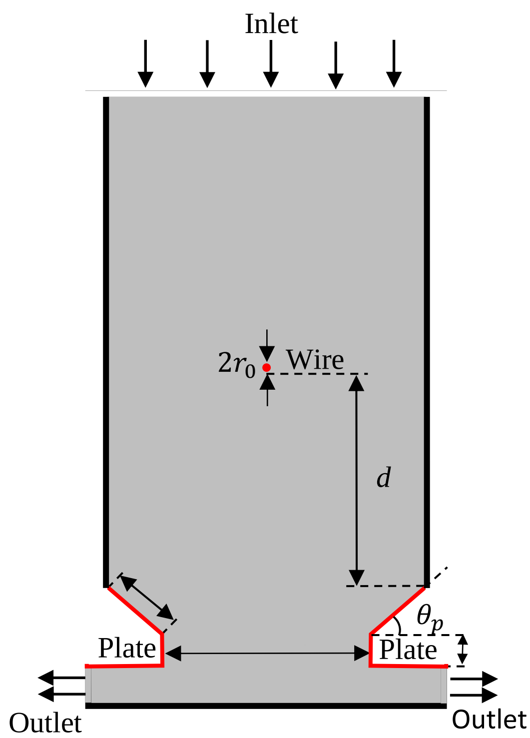

Figure V.21. Schematic illustration of the corona ionic wind blower (inclined plate). d = 3 cm, l = 1 cm, r = 100 µm, L = 3 cm.

Figure V.22 presents the current-voltage characteristics for five different incline angles ($\theta_p = 0°, 30°, 45°, 60°,$ and $90°$). The data indicate that, for a fixed applied voltage, the electric current decreases as the incline angle f increases. For instance, at -25 kV, the current drops by 25% when the angle changes from $0°$ to $30°$, by approximately $12\ \%$ for the transitions from $30°$ to $45°$ and $45°$ to $60°$, and by 27% when the angle increases from $60°$ to $90°$. At any applied voltage, the current is highest at $\theta_p = 0°$, as the horizontal ground surface (anode) aligns the electric field lines perpendicularly, enhancing the space charge density. Conversely, as the incline angle increases, the ground surface moves further from the critical pole (cathode), reducing the electric charge and thus the current.

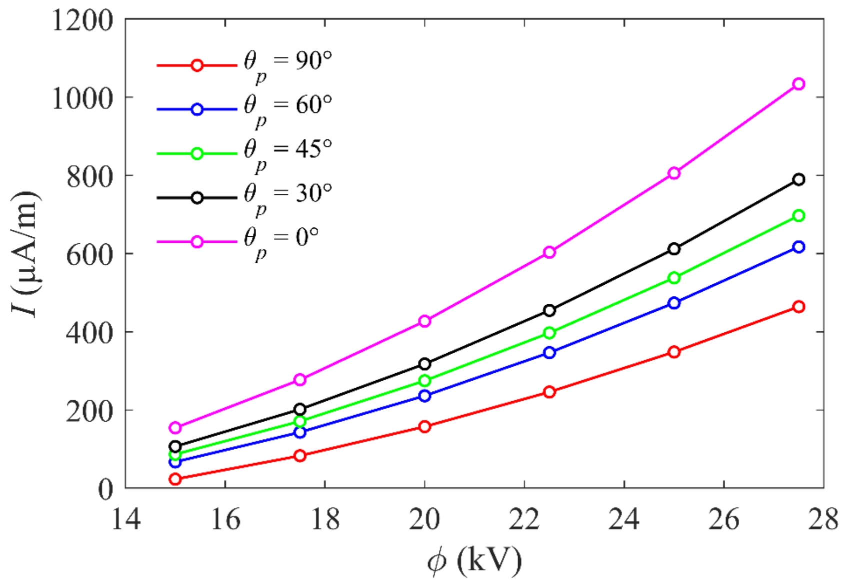

Figure V.22. Current-voltage characteristic for five different angles of inclined plate, $d = 3\ cm$, $l = 1\ cm$, $r_0 = 100\ \mu m$, $L = 3\ cm$.

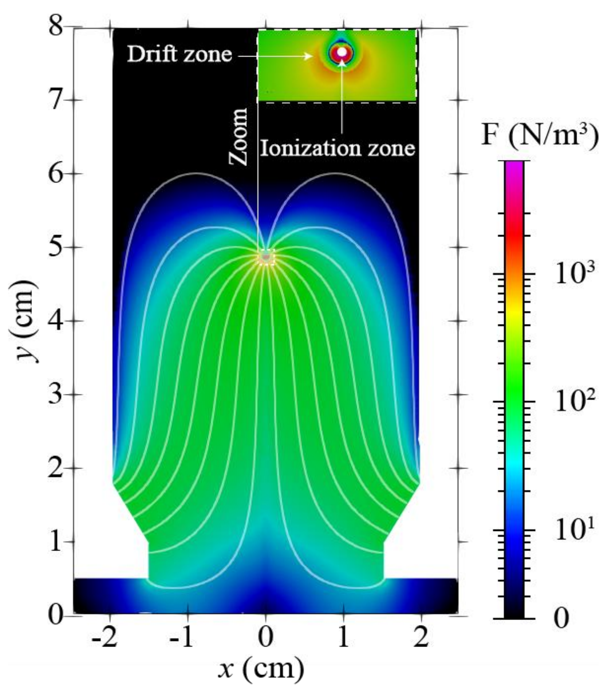

Figure V.23. 2D-spatial distribution of the of EHD force density for $d = 3\ cm$, $l = 1\ cm$, $r_0 = 100\ \mu m$, $L = 3\ cm$, $I = 248\ \mu A$ and $\theta_p = 60°$

Figure V.23 displays the 2D spatial distributions of EHD force intensity, along with force lines and a zoom view around the wire. The EHD force magnitude lines extend from the wire toward the two lower plates, emanating from the wire's surface and diverging towards the plates on each side. As previously noted, in the case of negative corona discharge, the sign of the electric force reverses around the boundary where the attachment coefficient equals the ionization coefficient.

Figure V.24 offers valuable insights into the influence of electrode geometry on air velocity in the electrohydrodynamic (EHD) blower. It highlights that altering the ground electrode angle affects the velocity at which air moves through the system. Specifically, the higher inclined electrode configuration lead to greater air velocity compared to lower inclined angles, underscoring the importance of electrode geometry in improving blower performance. A key indication is that at an electrical current of 150 µA, the wind velocity rises from 1.01 m/s to 1.38 m/s when the grounded electrode surface tilt angle increases from 0° to 90°.

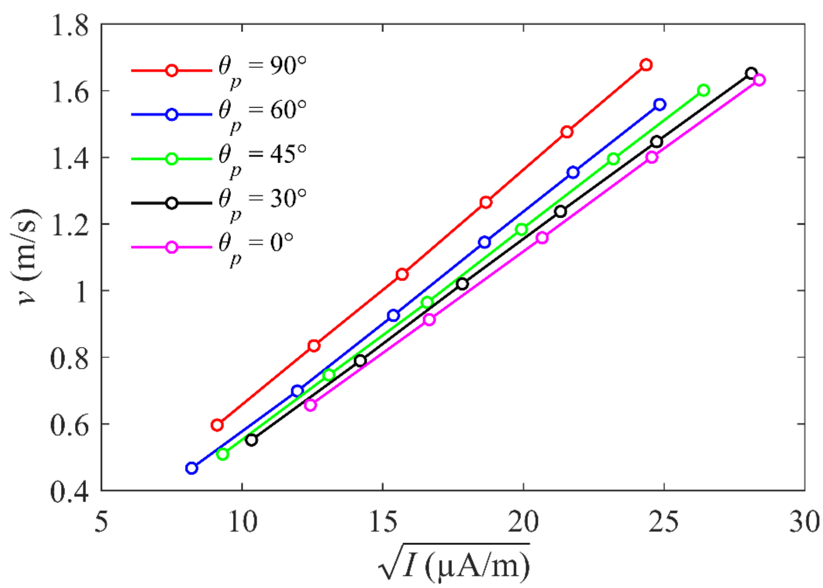

Figure V.24. Comparison of ionic wind velocity versus the square root of the electric current for five different angles of inclined plate, $d = 3$ cm, $l = 1$ cm, $L = 3$ cm and $r_0 = 100$ µm.

The results depicted in Figure V.25 highlighting the mechanisms driving the observed differences in air velocity. The two-dimensional velocity profiles indicate that the rectangular ground electrodes in the configuration shown in Figure V.1 lead to the creation of two compact vortices, which obstruct the flow of gas and consequently lower the overall air velocity. On the other hand, the configuration presented in Figure V.21, which features inclined electrodes, produces a higher electrohydrodynamic (EHD) force density. This enhanced force density reduces the rigidity of the vortices, facilitating a smoother and more efficient airflow at increased velocities.

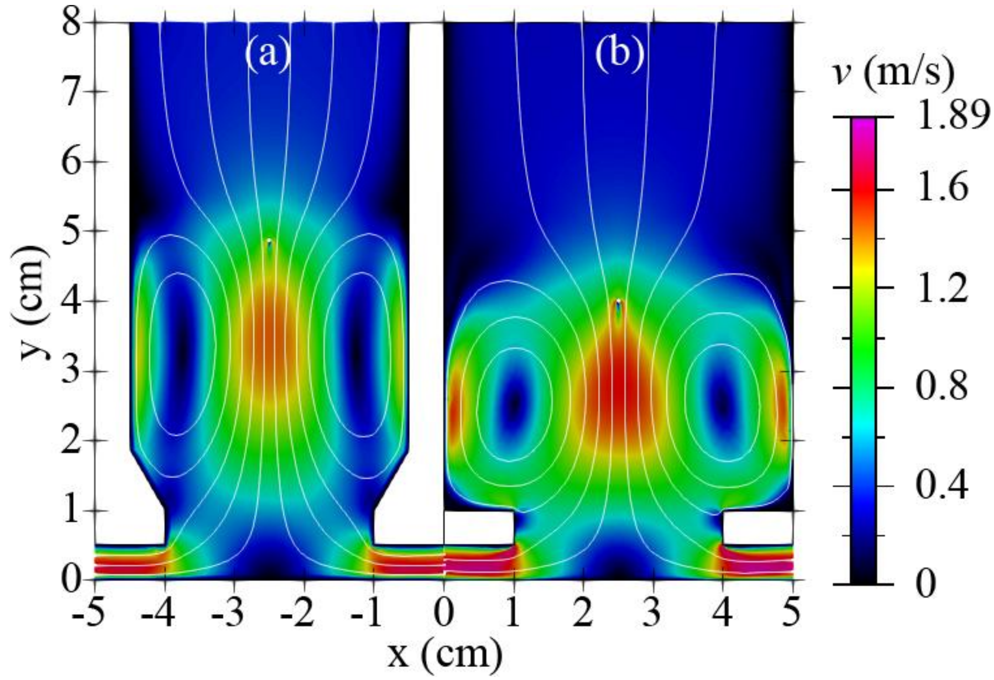

Figure V.25. Streamlines and 2D spatial distribution of the ionic wind velocity inside the blower device for $d = 3\ cm$, $r_0 = 100\ \mu m$, (a)- $\theta_p = 60°$, (b)- $\theta_p = 0°$ and I = 248 µA.

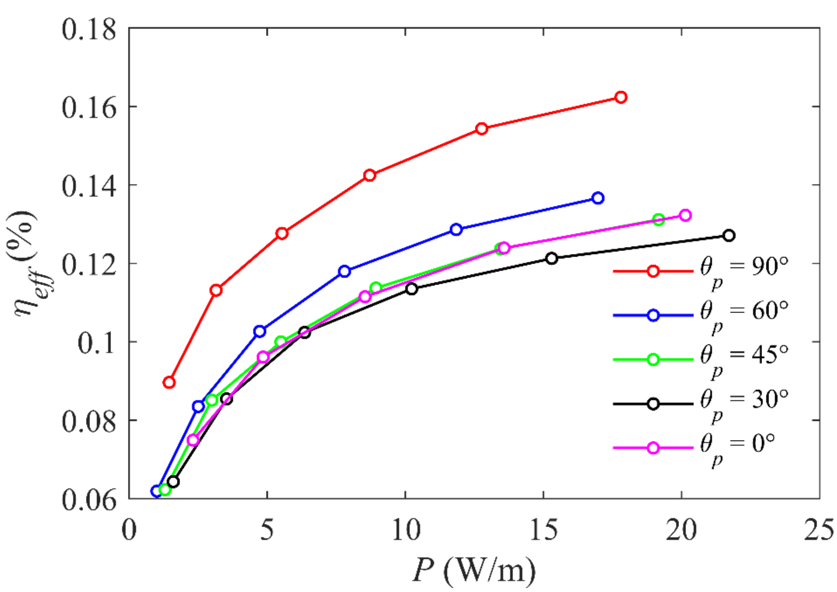

Figure V.26. The efficiency as function of the consumed electric power for five different electrode angles.

Figure V.26 presents a detailed analysis of the efficiency of the electrohydrodynamic (EHD) blower as a function of power for five different electrode angles (0°, 30°, 45°, 60°, and 90°). The data indicate a clear trend, showing that as the electrode angle increases, the efficiency of the device improves. For instance, at a power level of 15 W, the efficiencies for the 30°, 45°, 60°, and 90° angle configurations reach 0.12%, 0.125%, 0.135%, and 0.16%, respectively. For any given power value, the efficiency of the 0° (rectangular) device is comparable to that of the 45° configuration. The observed increase in efficiency with greater electrode angles can be attributed to the enhanced flow dynamics associated with larger angles, as discussed in Figure V.24 and Figure V.25. The 90° configuration likely promotes a more efficient distribution of the EHD force, leading to smoother and more consistent airflow. This arrangement minimizes energy loss due to vortex formation, which was more prevalent in lower-angle geometries.

I.1 Conclusion

In this study, we explored the use of ionic wind generated by corona discharge as an innovative method for cleaning photovoltaic (PV) panels, addressing the issue of efficiency loss due to dust accumulation. We conducted a numerical analysis of electro-hydrodynamic (EHD) air blowers with wire-to-rectangle configurations to investigate the potential of corona discharge for generating airflow. The 2D models used were validated experimentally. Our results demonstrate how various design parameters affect EHD airflow, including the distance between electrodes, the width of the grounded plate, the wire radius and the inclusion of the grounded plates. Specifically, increasing the inter-electrode distance or the width of the grounded plate leads to the increase of the electric wind velocity, assuming a fixed electric current. On the other hand, reducing the wire radius increased the EHD force, leading to a higher electric wind velocity when the applied voltage remained constant. This positive correlation allows the cleaning devices to operate at lower voltages, which can improve energy efficiency and reduce operational costs. The conversion efficiency of electrical energy to mechanical energy is significantly influenced by geometrical parameters, as follows:

- Optimal efficiency is achieved at an inter-electrode distance of 3 cm, where the electric field distribution is most effective, maximizing the kinetic energy transfer through electrohydrodynamic (EHD) forces.
- Using thicker grounded electrodes reduces vortex stiffness, resulting in a smoother and faster gas flow. This decrease in energy loss improves the efficiency of converting electrical energy into mechanical energy.
- Reducing the wire radius increases the electric current and gas velocity, which enhances mechanical efficiency.

➢ Inclined electrode configuration results in higher air velocity than lower angles, highlighting the crucial role of electrode geometry in enhancing blower performance.

The findings allow us to design a geometrically optimized system to investigate the efficiency of the ionic wind for solar panels cleaning in our future works.

Reference

[1] K. Yanallah et al., "Numerical Analysis of a New Corona Ionic Wind Blower Used for Solar Panel Cleaning," in 2023 IEEE Industry Applications Society Annual Meeting (IAS), Oct. 2023, pp. 1–12. doi: 10.1109/IAS54024.2023.10406798.

[2] H. A. Kazem, M. T. Chaichan, A. H. A. Al-Waeli, and K. Sopian, "A review of dust accumulation and cleaning methods for solar photovoltaic systems," Journal of Cleaner Production, vol. 276, p. 123187, Dec. 2020, doi: 10.1016/j.jclepro.2020.123187.

[3] M. T. Chaichan and H. A. Kazem, Generating Electricity Using Photovoltaic Solar Plants in Iraq. Cham: Springer International Publishing, 2018. doi: 10.1007/978-3-319-75031-6.

[4] S. S. and S. Darvekar, "Solar Photovoltaic Panels Cleaning Methods A Review," International Journal of Pure and Applied Mathematics, vol. 118, pp. 1–17, May 2018.

[5] A. Badhoutiya, "Evaluation of Different Methods used to Clean Solar Panel Surface," in 2023 Second International Conference on Electronics and Renewable Systems (ICEARS), Mar. 2023, pp. 46–48. doi: 10.1109/ICEARS56392.2023.10085478.

[6] J. A. P. Rodrigues, A. Sonia. A. C. Diniz, and L. L. Kazmerski, "Evaluation of the Impacts of Various Cleaning Techniques on Photovoltaic Module Glass," in 2021 IEEE 48th Photovoltaic Specialists Conference (PVSC), Jun. 2021, pp. 0958–0960. doi: 10.1109/PVSC43889.2021.9518864.

[7] N. S. Najeeb, P. K. Soori, and T. R. Kumar, "A Low-Cost and Energy-Efficient Smart Dust Cleaning Technique for Solar Panel System," in 2018 International Conference on Smart Grid and Clean Energy Technologies (ICSGCE), May 2018, pp. 125–129. doi: 10.1109/ICSGCE.2018.8556806.

[8] N. Anjum, K. A.s, M. P, and S. T. R, "Automatic Cleaning of Solar Panel," International Journal of Engineering Research & Technology, vol. 6, no. 13, Apr. 2018, doi: 10.17577/IJERTCONV6IS13062.

[9] P. A. Patil, J. S. Bagi, and M. M. Wagh, "A review on cleaning mechanism of solar photovoltaic panel," in 2017 International Conference on Energy, Communication, Data Analytics and Soft Computing (ICECDS), Aug. 2017, pp. 250–256. doi: 10.1109/ICECDS.2017.8389895.

[10] I. Walaman-i, S. Isaacs, and H. Beem, "Design of a Dust Cleaning Machine to Reduce Dust Soiling on Solar PV Panels in Ghana," in 2022 IEEE Global Humanitarian Technology Conference (GHTC), Sep. 2022, pp. 481–484. doi: 10.1109/GHTC55712.2022.9911012.

[11] S. Fan, W. Liang, G. Wang, Y. Zhang, and S. Cao, "A novel water-free cleaning robot for dust removal from distributed photovoltaic (PV) in water-scarce areas," Solar Energy, vol. 241, pp. 553–563, Jul. 2022, doi: 10.1016/j.solener.2022.06.024.

[12] D. Sun and K. F. Böhringer, "An active self-cleaning surface system for photovoltaic modules using anisotropic ratchet conveyors and mechanical vibration," Microsyst Nanoeng, vol. 6, no. 1, pp. 1–12, Sep. 2020, doi: 10.1038/s41378-020-00197-z.

[13] S. N. N. A. Hamidon, A. Nawabjan, A. S. Abdullah, and S. M. Hussin, "Hydrophobic Sol-Gel Based Self-cleaning Coating for Photovoltaic Panels," vol. 632, pp. 753–765, 2020, doi: 10.1007/978-981-15-2317-5_63.

[14] S. P. Dalawai et al., "Recent Advances in durability of superhydrophobic self-cleaning technology: A critical review," Progress in Organic Coatings, vol. 138, p. 105381, Jan. 2020, doi: 10.1016/j.porgcoat.2019.105381.

[15] M. Altıntaş and S. Arslan, “The Study of Dust Removal Using Electrostatic Cleaning System for Solar Panels,” Sustainability, vol. 13, no. 16, Art. no. 16, Jan. 2021, doi: 10.3390/su13169454.

[16] S. Panat and K. K. Varanasi, “Electrostatic dust removal using adsorbed moisture–assisted charge induction for sustainable operation of solar panels,” Science Advances, vol. 8, no. 10, p. eabm0078, Mar. 2022, doi: 10.1126/sciadv.abm0078.

[17] A. Sayyah, M. N. Horenstein, and M. K. Mazumder, “A comprehensive analysis of the electric field distribution in an electrodynamic screen,” Journal of Electrostatics, vol. 76, pp. 115–126, Aug. 2015, doi: 10.1016/j.elstat.2015.04.002.

[18] A. Sayyah, M. N. Horenstein, M. K. Mazumder, and G. Ahmadi, “Electrostatic force distribution on an electrodynamic screen,” Journal of Electrostatics, vol. 81, pp. 24–36, Jun. 2016, doi: 10.1016/j.elstat.2016.02.004.

[19] A. Zouaghi, N. Zouzou, and P. Braud, “Study of dielectric particles motion in traveling and standing electrostatic waves using particle tracking velocimetry,” J. Phys. D: Appl. Phys., vol. 53, no. 38, p. 385502, Jul. 2020, doi: 10.1088/1361-6463/ab93f6.

[20] A. Zouaghi and N. Zouzou, “Numerical modeling of particle motion in traveling wave solar panels cleaning device,” Journal of Electrostatics, vol. 110, p. 103552, Mar. 2021, doi: 10.1016/j.elstat.2021.103552.

[21] A. Tilmatine, N. Kadous, K. Yanallah, Y. Bellebna, Z. Bendaoudi, and A. Zouaghi, “Experimental investigation of a new solar panels cleaning system using ionic wind produced by corona discharge,” Journal of Electrostatics, vol. 124, p. 103827, Jul. 2023, doi: 10.1016/j.elstat.2023.103827.

[22] N. Kadous, K. Yanallah, Y. Bellebna, Z. Bendaoudi, and A. Tilmatine, “Exploring the effectiveness of a novel cleaning method for solar panels using corona ionic wind,” Particulate Science and Technology, vol. 42, no. 2, pp. 324–330, Feb. 2024, doi: 10.1080/02726351.2023.2243857.

[23] M. Ghazanchaei, K. Adamiak, and G. S. P. Castle, “Predicted flow characteristics of a wire-nonparallel plate type electrohydrodynamic gas pump using the Finite Element Method,” Journal of Electrostatics, vol. 73, pp. 103–111, Feb. 2015, doi: 10.1016/j.elstat.2014.11.003.

[24] S. Venkatesh, A. Kumar, A. Bhattacharya, and S. Pramanik, “Ionic wind review-2020: advancement and application in thermal management,” Sādhanā, vol. 46, no. 3, p. 165, Aug. 2021, doi: 10.1007/s12046-021-01687-0.

[25] N. N. Misra and A. Martynenko, “Multipin dielectric barrier discharge for drying of foods and biomaterials,” Innovative Food Science & Emerging Technologies, vol. 70, p. 102672, Jun. 2021, doi: 10.1016/j.ifset.2021.102672.

[26] K. Iranshahi, D. I. Onwude, A. Martynenko, and T. Defraeye, “Dehydration mechanisms in electrohydrodynamic drying of plant-based foods,” Food and Bioproducts Processing, vol. 131, pp. 202–216, Jan. 2022, doi: 10.1016/j.fbp.2021.11.009.

[27] E. Moreau, N. Benard, J.-D. Lan-Sun-Luk, and J.-P. Chabriat, “Electrohydrodynamic force produced by a wire-to-cylinder dc corona discharge in air at atmospheric pressure,” J. Phys. D: Appl. Phys., vol. 46, no. 47, p. 475204, Oct. 2013, doi: 10.1088/0022-3727/46/47/475204.

[28] M. Mazumder et al., “Characterization of Electrodynamic Screen Performance for Dust Removal from Solar Panels and Solar Hydrogen Generators,” IEEE Transactions on Industry Applications, vol. 49, no. 4, pp. 1793–1800, Jul. 2013, doi: 10.1109/TIA.2013.2258391.

[29] E. Moreau, C. Louste, G. Artana, M. Forte, and G. Touchard, “Contribution of Plasma Control Technology for Aerodynamic Applications,” Plasma Processes and Polymers, vol. 3, no. 9, pp. 697–707, 2006, doi: 10.1002/ppap.200600059.

[30] K. Yanallah et al., “A new numerical approach for efficient modeling of positive corona discharge and its associated electric wind,” J. Phys. D: Appl. Phys., vol. 56, no. 41, p. 415201, Jul. 2023, doi: 10.1088/1361-6463/ace456.

[31] K. Yanallah, F. Pontiga, and J. H. Chen, "A semi-analytical study of positive corona discharge in wire–plane electrode configuration," J. Phys. D: Appl. Phys., vol. 46, no. 34, p. 345202, Aug. 2013, doi: 10.1088/0022-3727/46/34/345202.

[32] M. R. Bouazza, K. Yanallah, F. Pontiga, and J. H. Chen, "A simplified formulation of wire-plate corona discharge in air: Application to the ion wind simulation," Journal of Electrostatics, vol. 92, pp. 54–65, Apr. 2018, doi: 10.1016/j.elstat.2018.02.001.

[33] L. Zhao and K. Adamiak, "Effects of EHD and External Airflows on Electric Corona Discharge in Point-Plane/Mesh Configurations," IEEE Transactions on Industry Applications, vol. 45, no. 1, pp. 16–21, Jan. 2009, doi: 10.1109/TIA.2008.2009389.

[34] L. Zhao and K. Adamiak, "Numerical simulation of the effect of EHD flow on corona discharge in compressed air," in 2011 IEEE Industry Applications Society Annual Meeting, Oct. 2011, pp. 1–7. doi: 10.1109/IAS.2011.6074283.

[35] M. Goldman and A. Goldman, "Chapter 4 - Corona Discharges," in Gaseous Electronics, M. N. Hirsh and H. J. Oskam, Eds., Academic Press, 1978, pp. 219–290. doi: 10.1016/B978-0-12-349701-7.50009-2.

[36] B. A. Kozlov and V. I. Solovyov, "Electric wind in electrode systems with corona points," Tech. Phys., vol. 52, no. 7, pp. 892–897, Jul. 2007, doi: 10.1134/S1063784207070109.

[37] E. Moreau and G. Touchard, "Enhancing the mechanical efficiency of electric wind in corona discharges," Journal of Electrostatics, vol. 66, no. 1, pp. 39–44, Jan. 2008, doi: 10.1016/j.elstat.2007.08.006.

[38] R. S. Sigmond, "The unipolar corona space charge flow problem," Journal of Electrostatics, vol. 18, no. 3, pp. 249–272, Oct. 1986, doi: 10.1016/0304-3886(86)90021-5.

[39] R. S. Sigmond and I. H. Lågstad, "Mass and species transport in corona discharges," High Temp. Chem. Processes, vol. 2, no. 4, p. 5, 1993.

Conclusions

Conclusions

This work explored and modeled the complex phenomena associated with corona discharge and its applications in electrohydrodynamic (EHD) systems, integrating concepts from plasma physics, fluid mechanics, and electrical engineering to enhance understanding and practical implementation.

The work began with the development of a robust modeling approach for steady-state corona discharge using Laplacian electric field lines as a starting point. Approximated analytical expressions for the electric field intensity along these lines, coupled with a simple root-finding algorithm, enabled the determination of the space charge distribution and EHD force density. This approach avoids the numerical convergence issues typically associated with coupling Gauss's law with the charge continuity equation. Additionally, the model demonstrated versatility by accommodating various electrode configurations, such as wire-to-cylinder and wire-to-plate setups, for both positive and negative DC corona discharges. The results highlighted the model's robustness and broad applicability, making it a valuable tool for practical design and analysis.

The second part of this study expanded on this work by rigorously validating the numerical model through comparisons with experimental data. The model accurately reproduced critical electrical characteristics, such as current-voltage relationships and the spatial distribution of current density at the cathode, confirming its reliability in simulating corona discharges. Moreover, the model effectively predicted EHD characteristics, including ionic wind velocities and gas flow distributions, which were consistent with experimental observations. An improved electrode configuration for EHD air movers was proposed, featuring corona wires embedded within dielectric walls. This design simplified construction, enhanced velocity distribution, eliminated recirculating vortices, and achieved better energy efficiency than conventional configurations, addressing critical challenges in cooling systems, particularly for miniaturized electronic components.

In the third part of this study, the investigation shifted to the shielding effect between adjacent corona discharge electrodes in two-wire-to-plate. The study focused on the impact of mutual electrostatic interactions on the structure of EHD flow, an aspect underexplored in the literature. Key findings included:

- The attenuation of electric current, space charge density, and EHD force as the inter-wire spacing decreases, primarily due to shielding effects.
- Increasing asymmetry in flow patterns and force distributions as wire spacing reduces, causing flow deflection and diminished efficiency.
- The impact of parameters such as wire radius, electrode distance, and applied voltage on EHD flow direction, magnitude, and vortex structures, offering crucial insights for optimizing device performance.

Finally, we conducted a parametric study on a novel application of ionic wind generated by corona discharge for cleaning photovoltaic (PV) panels, addressing efficiency losses caused by dust accumulation. A wire-to-rectangle electrode configuration was numerically modeled and experimentally validated. The study examined how design parameters, such as inter-electrode distance, wire radius, and grounded plate geometry, influence EHD airflow. Results showed that increasing the inter-electrode distance or the plate width improved airflow velocity, while reducing the wire radius enhanced the EHD force, enabling lower operational voltages for cleaning devices. Specific geometric optimizations, such as inclined electrodes, were shown to enhance airflow, improving cleaning efficiency and reducing energy consumption. Notably:

- Reducing wire radius or increasing inter-electrode spacing (3cm) enhanced ionic wind velocity, optimizing energy conversion from electrical to mechanical energy.
- Thicker grounded electrodes reduced turbulence, leading to smoother airflow and improved energy efficiency.
- Inclined electrode configurations further enhanced airflow velocity, showcasing the importance of geometric design in optimizing performance.

Through a detailed investigation of corona discharge and its EHD effects, this work has demonstrated the versatility and applicability of numerical modeling in addressing key challenges across various engineering fields. It established a robust modeling framework, validated its accuracy, and explored its applications in diverse scenarios, including cooling systems, electrostatic precipitators, and PV panel cleaning. By addressing critical design parameters and offering innovative solutions, this research provides valuable insights for optimizing EHD-based technologies. The findings pave the way for future advancements in microfluidics, HVAC systems, and renewable energy solutions, offering practical pathways to enhance performance, energy

Publications and communications

Publications

- K. Yanallah, **A. Chelih**, M. R. Bouazza, F. Pontiga, M. Bouadi, P. Vázquez, and B. zeid, "A new numerical approach for efficient modeling of positive corona discharge and its associated electric wind," J. Phys. D: Appl. Phys., vol. 56, no. 41, p. 415201, Jul. 2023, doi: 10.1088/1361-6463/ace456.
- **A. Chelih**, M. Bouadi, M. R. Bouazza, K. Yanallah, and A. Safa, "Investigating the Impact of Electrode Wire Interaction on EHD Flow in Two-Wire-to-Plate Corona Devices: A Computational Analysis," IEEE Transactions on Plasma Science, vol. 52, no. 2, pp. 212–221, Feb. 2024, doi: 10.1109/TPS.2024.3361498.
- K. Yanallah, **A. Chelih**, Y. Bellebna, N. Kadous, B. zeid, A Zouaghi, A. Tilmatine, and L. Canale, "Numerical Analysis of a New Corona Ionic Wind Blower Used for Solar Panel Cleaning," *IEEE Transactions on Industry Applications*, pp. 1–10, 2025, doi: 10.1109/TIA.2025.3531827.

Communications international

- M. R. Bouazza, M. Bouadi, **A. Chelih**, K. Yanallah, F. Pontiga, and P. Vázquez, "Effect of the EHD Force on the Spatial Distribution of Neutral Species Generated by a Positive and Negative Corona Discharge," in 2022 IEEE 21st International Conference on Dielectric Liquids (ICDL), May 2022, pp. 1–4. doi: 10.1109/ICDL49583.2022.9830955.
- **A. Chelih**, M. Bouadi, M. R. Bouazza, A. Safa, K. Yanallah, and F. Pontiga, "Illustration of the dependence of the electrohydrodynamic force on the electrode configuration in a positive corona discharge," in 2022 2nd International Conference on Advanced Electrical Engineering (ICAEE), Oct. 2022, pp. 1–6. doi: 10.1109/ICAEE53772.2022.9962131.
- K. Yanallah, **A. Chelih**, Y. Bellebna, N, Kadous, Z Boudaoud, A Zouaghi, and A. Tilmatine, "Numerical Analysis of a New Corona Ionic Wind Blower Used for Solar Panel Cleaning," in 2023 IEEE Industry Applications Society Annual Meeting (IAS), Oct. 2023, pp. 1–12. doi: 10.1109/IAS54024.2023.10406798.
- **A. Chelih**, M. R. Bouazza, N. Kadous, Y. Bellebna, K. Yanallah, and A. Tilmatine, "Shielding Impact on Efficiency of Electric Wind Blower for Solar Panel Cleaning," in

2024 3rd International Conference on Advanced Electrical Engineering (ICAEE), Nov 5th - 7th 2024, Sidi-Bel-Abbes, Algeria.

- M. F. Bekkara, Ali. Bouargoub, **A. Chelih**, D. Azzeddine, H. Azzeddine, and Y. Benmimoun, “Analyzing particles trajectories in a free-fall electrostatic separator,” in 2023 1st International Conference on Advances in Electronics, Control and Computer Technologies “ICAECCT’23”, Oct 25th – 26th 2023, Mascara, Algeria.
- **A. Chelih**, M. R. Bouazza, N. Kadous, Y. Bellebna, K. Yanallah, and A. Tilmatine, “Shielding Impact on Efficiency of Electric Wind Blower for Solar Panel Cleaning,” in *2024 3rd International Conference on Advanced Electrical Engineering (ICAEE)*, Nov. 2024, pp. 1–6. doi: 10.1109/ICAEE61760.2024.10783170.
- **Communications national**
- M. R. Bouazza, M. Bouadi, K. Yanallah, and **A. Chelih**, “La production de l’ozone par une décharge électrique couronne positive de configuration fil-grille,” La Journée d’Etude de la Physique et de ses Applications (JEPA), Dec 21th 2022, Tiaret, Algérie.
- **A. Chelih**, M. R. Bouazza, M. Bouadi, A. Safa, K. Yanallah, F. Pontiga, and Y. Messlem, “The influence of shielding on the gas-dynamic in two wires plate positive corona discharge.” in 2023 12th National Conference on High Voltage Engineering (CNHT), Oct 04th – 06th 2022. Sidi-Bel-Abbes, Algeria.
- M. R. Bouazza, K. Yanallah, **A. Chelih**, “ Modélisation de l'écoulement électro-hydrodynamique (EHD) produit par une décharge électrique couronne de type fil-deux plaques.,” La Journée d’Etude de la Physique et de ses Applications (JEPA), Dec 17th – 18th 2024, Tiaret, Algérie.

Abstract

An electrical discharge is generated between two electrodes, one subjected to high voltage and the other grounded, within a gaseous environment. In such a setup, the plasma behavior is primarily influenced by physical parameters (e.g., high applied voltage, injected power) and geometric configurations (e.g., electrode spacing, electrode symmetry). This discharge results in the conversion of electrical energy into mechanical energy, producing what is known as electrohydrodynamic (EHD) flow or "ionic wind," characterized by a specific velocity. Ionic ventilation technologies have gained significant importance over the years in applications such as cooling microelectronic devices, preserving food products, and reducing training loads for astronauts. These systems are compact, easy to understand, silent, non-polluting, and economically efficient. To better understand, control, and exploit ionic ventilation generated by electrical discharge, this study integrates comprehensive research on modeling, validation, and applications of corona discharge in EHD systems. It combines numerical simulation, experimental validation, and innovative design optimization to address both fundamental and practical aspects. Key contributions include a detailed overview of plasma and electrical discharges, with a focus on corona discharge and ionic wind phenomena, the development of a flexible methodology to determine space charge distribution and EHD force density—crucial for understanding ionic wind dynamics—and addressing challenges related to numerical convergence. The study also validates numerical models against experimental data, optimizes electrode designs for EHD air pumps to enhance cooling systems, particularly for microelectronics, investigates shielding effects between corona discharge electrodes in electrostatic precipitators, and explores EHD cleaning systems for photovoltaic panels, highlighting their effectiveness in mitigating dust accumulation and improving performance. This research provides a unified framework for advancing EHD applications, paving the way for cost-effective, energy-efficient solutions across multiple engineering fields.

Keywords: *ionic wind, corona discharge, numerical modeling, electrohydrodynamic force, shielding effect.*

Résumé

Une décharge électrique est générée entre deux électrodes, l'une soumise à une haute tension et l'autre mise à la terre, dans un environnement gazeux. Dans ce contexte, le comportement du plasma est principalement influencé par des paramètres physiques (par exemple, la tension élevée appliquée, la puissance injectée) et des configurations géométriques (par exemple, l'espacement entre les électrodes, la symétrie des électrodes). Cette décharge entraîne la conversion de l'énergie électrique en énergie mécanique, produisant ce que l'on appelle un flux électro-hydrodynamique (EHD) ou "vent ionique," caractérisé par une vitesse spécifique. Les technologies de ventilation ionique ont gagné une importance significative au fil des années, dans des applications telles que le refroidissement des dispositifs microélectroniques, la conservation des produits alimentaires, et la réduction des charges d'entraînement pour les astronautes. Ces systèmes sont compacts, faciles à comprendre, silencieux, non polluants et économiquement efficaces. Afin de mieux comprendre, maîtriser et exploiter la ventilation ionique générée par la décharge électrique, cette étude intègre des recherches approfondies sur la modélisation, la validation et les applications de la décharge couronne dans les systèmes EHD. Elle combine la simulation numérique, la validation expérimentale et l'optimisation de conception innovante pour aborder à la fois les aspects fondamentaux et pratiques. Les contributions clés incluent une vue d'ensemble détaillée sur le plasma et les décharges électriques, avec un focus particulier sur les phénomènes de décharge couronne et de vent ionique, le développement d'une méthodologie flexible pour déterminer la distribution des charges spatiales et la densité de force EHD — élément crucial pour comprendre la dynamique du vent ionique — ainsi que le traitement des défis liés à la convergence numérique. L'étude valide également les modèles numériques par rapport aux données expérimentales, optimise les conceptions d'électrodes pour les pompes à air EHD afin d'améliorer les systèmes de refroidissement, notamment pour la microélectronique, explore les effets d'écran entre les électrodes de décharge couronne dans les précipitateurs électrostatiques, et étudie les systèmes de nettoyage EHD pour les panneaux photovoltaïques, mettant en évidence leur efficacité dans la réduction de l'accumulation de poussière et l'amélioration des performances. Cette recherche offre un cadre unifié pour faire avancer les applications EHD, ouvrant la voie à des solutions rentables et écoénergétiques dans de nombreux domaines de l'ingénierie.

Mots clés : *vent électrique, décharge électrique couronne, modèle analytique, force électro-hydrodynamique, effet blindage.*

ملخص

يتم توليد تفريغ كهربائي بين قطبين كهربائيين، أحدهما يخضع لجهد كهربائي عالٍ والآخر مؤرض، داخل بيئة غازية. في هذا السياق، يعتمد سلوك البلازما بشكل رئيسي على المعايير الفيزيائية (مثل الجهد العالي المطبق، الطاقة المحقونة) والإعدادات الهندسية (مثل المسافة بين الأقطاب الكهربائية، تماثل الأقطاب الكهربائية). يؤدي هذا التفريغ إلى

تحويل الطاقة الكهربائية إلى طاقة ميكانيكية، مما ينتج عنه تدفق يُعرف باسم التدفق الكهروهيدروديناميكي (EHD) أو "الرياح الأيونية"، التي تتميز بسرعة محددة. اكتسبت تقنيات التهوية الأيونية أهمية كبيرة على مدار السنوات في تطبيقات مثل تبريد الأجهزة الإلكترونية الدقيقة، والحفاظ على المنتجات الغذائية، وتقليل الأحمال التدريبية لرواد الفضاء. هذه الأنظمة مدمجة، سهلة الفهم، هادئة، غير ملوثة، وفعالة اقتصاديًا. لفهم أفضل والسيطرة على التهوية الأيونية الناتجة عن التفريغ الكهربائي واستغلالها، تجمع هذه الدراسة بين بحوث شاملة لفهم نمذجة وتحقق وتطبيق تفريغ الهالة في أنظمة .EHD تدمج الدراسة بين المحاكاة الرقمية والتحقق التجريبي وتحسين التصميم المبتكر لمعالجة الجوانب الأساسية والتطبيقية. تشمل المساهمات الرئيسية نظرة شاملة على البلازما والتفريغات الكهربائية مع التركيز بشكل خاص على ظواهر تفريغ الهالة والرياح الأيونية، وتطوير منهجية مرنة لتحديد توزيع الشحنات الفضائية وكثافة القوة الكهروهيدروديناميكية—عنصر أساسي لفهم ديناميكيات الرياح الأيونية—بالإضافة إلى معالجة التحديات المتعلقة بالتقارب العددي. تؤكد الدراسة أيضًا على صحة النماذج العددية بمقارنتها مع البيانات التجريبية، وتحسن تصميم الأقطاب الكهربائية لمضخات الهواء EHD لتحسين أنظمة التبريد، خاصة للإلكترونيات المصغرة. كما تحقق في تأثيرات الحماية بين أقطاب تفريغ الهالة وتأثيرها على تدفق EHD في المرسبات الكهروستاتيكية، وتستكشف أنظمة التنظيف الكهروهيدروديناميكية للألواح الكهروضوئية، مسلطة الضوء على فعاليتها في معالجة تراكم الغبار وتحسين الأداء. تقدم هذه الدراسة إطارًا موحدًا لتطوير تطبيقاتEHD ، مما يمهد الطريق لحلول فعالة من حيث التكلفة وكفاءة الطاقة في مجالات هندسية متعددة.

الكلمات المفتاحية :الرياح الكهربائية، التفريغ الكهربائي التاجي، النموذج الرياضي، القوة الكهروهيدروديناميكية، تأثير التدريع.